THE UNIVERSITY OF CHICAGO

SOLVATION FORCES AND RIGIDITY IN DENSE SUSPENSION FLOWS

A DISSERTATION SUBMITTED TO

THE FACULTY OF THE DIVISION OF THE PHYSICAL SCIENCES

IN CANDIDACY FOR THE DEGREE OF

DOCTOR OF PHILOSOPHY

DEPARTMENT OF PHYSICS

BY

MICHAEL REEVES VAN DER NAALD

CHICAGO, ILLINOIS

DECEMBER 2023

To all my friends and family.

“Oh, she says, well, you’re not a poor man. You know, why don’t you go online and buy a hundred envelopes and put them in the closet? And so I pretend not to hear her. And go out to get an envelope because I’m going to have a hell of a good time in the process of buying one envelope. I meet a lot of people. And see some great looking babies. And a fire engine goes by. And I give them the thumbs up. And I’ll ask a woman what kind of dog that is. And, and I don’t know. The moral of the story is - we’re here on Earth to fart around. And, of course, the computers will do us out of that. And what the computer people don’t realize, or they don’t care, is we’re dancing animals. You know, we love to move around. And it’s like we’re not supposed to dance at all anymore." — Kurt Vonnegut

TABLE OF CONTENTS

LIST OF FIGURES

ACKNOWLEDGMENTS

First and foremost is my advisor, Heinrich Jaeger, for the support, mentorship, and guidance throughout the last six years. Learning how to do science and perhaps more importantly, communicate science, from you has been a privledge. Thank you for letting me in. Next my committee Sidney Nagel, Vincenzo Vitelli, and David Schmitz for attending meetings, giving advice, and above all being kind.

I was incredibly lucky to have exquisite lab mates in the Jaeger lab who throughout my PhD were always willing to talk science or just chat with me. I'm particularly indebted to all the folks I did dense suspension research with in no particular order are Nicole James, Endao Han, Grayson Jackson, Abhi Singh, Hojin Kim, Sam Livermore, Malcolm Slutzky, Elise Chen, Neil Dolinkski, Finn Braaten, Margot Young. Particularly Nicole James, Grayson Jackson, Juan de Pablo, and Abhi Singh are responsible for much of the day to day mentoring that I received and I'm forever grateful they taught me how they do science. In addition to the folks I did direct research with in the Jaeger lab I also benefitted from the warmth and intelligence of many others such as: Ted Esposito, Kieran Murphy, Leah Roth, Bryan Vansaders, Melody Lim, Baudouin Saintyves, Severine Atis, Brady Wu, Qinghao Mao, Tali Khain.

Outside of the lab I had the undying support of my partner, Sophia Weaver. It is hard to articulate just how much she helped me through everything that culminated to this document and my life as it is today. I am forever grateful for her support. My mother and father supported me throughout this experience with annual visits, weekly phone calls, and encouragement through their confidence in my abilities. My brother and his partner Carla are model people that have set the pace in my life for at least the last decade of what kind of person I want to be both intellectually and in how I treat people. These five folks formed the backbone for my graduate school experience and while not directly in the lab with me they shaped so much of this experience by informing who I am.

My friends in Chicago were constant distraction and support throughout and I am sure this list will fall short but some of them are: Robert Shreiner, Gray Putnam, Jonah Kudler-Flam, Alanna Kaiser, Emily Cole, Gray Putnam, Dan Southall, Chloe Lindeman, Savannah Gowen, Robert Morton, Takumi Matsuzawa, and Ephraim Bililign. Beyond Chicago my friends in Oregon always supported me throughout all of my studies, while there are many I am most indebted to: Louis Wolf, Marcus Hess, Angeline Sanders, and Nathan Jansen.

Finally, I acknowledge support from the Center for Hierarchical Materials Design (CHiMaD) under award number 70NANB19H005 (US Dept. Commerce) and from the Army Research Office under grants W911NF-19-1-0245, W911NF-20-2-0044 and W911NF-21-2-0146.

ABSTRACT

Suspensions are mixtures of solid particles in a liquid medium. As the volume fraction of the suspending particles approaches the maximal jamming packing fraction, ϕ_J, the material properties of these seemingly simple systems can exhibit discontinuous shear thickening (DST) where the viscosity increases discontinuously with shear rate, and even transition to a solid in a process known as shear jamming (SJ). Despite being simple and ubiquitous systems, many open questions in suspension science remain. Among them are the following questions: how do nanoscale and chemical features of the suspended particles and suspending media impact the bulk flow and solidification behavior, how do rigid frictional force networks inside suspension flow impact dissipation, and how do suspended particles with similar chemical characteristic but different morphological characteristics differ in their non-Newtonian flow behavior. This work touches on all three of those questions and finds new solvent chemical knobs to tune shear thickening and shear jamming, new phases of suspension flow where solid structures are embedded in flowing systems, and similarities and differences between different starch suspensions. This dissertation provides fundamental insights into how to control dense suspension systems using the chemistry of the suspending solvent, understand new dissipation mechanisms beyond interparticle forces, and insights into how different starch systems can show dramatically different rheological responses.

CHAPTER 1

INTRODUCTION

Dense suspensions are simple mixtures of solid particles suspended in a liquid and this simplicity makes them ubiquitous in natural processes that span a massive range of length scales from debris flow to blood flow in addition to being indispensable in industrial processes and products, such as slurry processing or paints. Their material properties can be either liquid-like or solid-like with the operative variables to tune between the two states being the volume fraction of suspended particles and the applied stress (5; 6; 7). In the liquid phase they can show non-Newtonian properties such as shear thickening, where the viscosity of the material increases with applied stress. At sufficiently high volume fractions and stresses the flow arrests and the material transitions into a solid phase that, depending on the morphology, chemistry, and size of suspended particles, can have a range of material properties (2; 8; 9; 10; 11). Despite this ubiquity, it is only in the last decade that physicists have begun bringing these materials into the fold of condensed matter physics by rigorously characterizing their properties and various phases.

These advances were enabled by establishing a model system of monodisperse or bidisperse hard-sphere suspensions that allowed experimentalists and theorists to develop a baseline for the underlying physics(12; 13; 14; 1; 15; 16; 17). In turn, this has only enabled more lines of inquiry that connect suspension physics to chemistry, statistical physics, material science, among other fields. In this thesis, we will will investigate the connections between suspension flow and nano-scale tribology, rigidity theory, and how suspension flows connect to everday materials. Before delving into those connections we first have to establish the phenomenology of suspension physics as well as a chapter about how experiments are conducted. My hope is that this document will serve not only as a culmination of my findings on suspension flow, but also as a useful document for future researchers who wish to learn how to do dense suspension experiments.

1.1 Shear Thickening and Shear Jamming Suspensions

As mentioned in the introduction, suspensions are solid particles suspended in a liquid medium. For this work we consider a liquid medium that is a Newtonian liquid, meaning its viscosity is not a function of shear rate. By suspending solid particles in a Newtonian liquid one often gets another fluid that is non-Newtonian with a wide range of responses to shear rate such as shear thickening, shear jamming, shear thinning, thixotropy, anti-thixotropy, etc (18; 19; 9). We will only consider suspensions that show shear thickening (ST) where the viscosity of the fluid increases with shear rate and shear jamming (SJ) where the suspension solidifies under applied stress. Examples of a shear thickening response measured using a rheometer are shown in Fig. 1.1, while an example of shear jamming response is shown in two different cornstarch suspensions that have solidified under extensional stresses Fig 1.2a and under impact in Fig 1.2b. Both ST and SJ can be found in granular suspensions where the diameter roughly exceeds 1um, rendering Brownian motion negligible, and colloidal dispersions where the diameter is less than 1um and Brownian motion is important(12).

1.1.1 Packing fraction ϕ

For an example of shear thickening we plot the viscosity vs shear stress for fumed silica suspensions of various volume fractions in Fig. 1.1a and we plot the same data as a function of shear rate in Fig. 1.1b. Higher packing fraction ϕ give a stronger shear thickening response as measured by the slope (β) of the curves when undergoing shear thickening when the viscotiy η is plotted as a function of shear stress τ. Here the packing fraction, ϕ, is defined as the ratio of volume of solid particles to the total volume:

$$\phi = \frac{V_P}{V_P + V_S} \tag{1.1}$$

where V_P is the volume of the particles and V_S is the volume of the suspending medium. Preparing suspensions with precise packing fractions and best practices for measuring data like that in Fig. 1.1 is the subject of Chapter 2. There are two types of shear thickening shown in Fig. 1.1. The first is continuous shear thickening (CST) which is echibited by the lowest packing fraction, $\phi = 27.1$, where in Fig. 1.1b the viscosity of this suspension increases continuously with shear rate. The highest packing fraction $\phi = 33.2$ shows discontinuous shear thickening (DST) in Fig. 1.1b, where the viscosity increases discontinuously as a function of shear rate. These same suspensions can also show shear jamming (SJ) at higher stresses which are accessible by doing impact testing which is discussed in Chapter 3. Shear thickening suspensions often show shear jamming if prepared at higher packing fractions or stresses. Where these transitions occur in ϕ-τ phase space is the subject of the last two sections of this chapter.

1.1.2 Frictional Contacts and Shear Thickening and Shear Jamming

Strong shear thickening, like the DST shown in Fig. 1.1, and shear jamming, have their origins in networks of suspended particles interacting frictionally (15; 12; 10; 20; 21). These networks of frictional contacts can be visualized in simulations as in Fig. 1.3, by red lines that connect particles where the width of the line indicates the strength of this frictional interaction. In the case of shear thickening the viscosity increase is primarily due to the continual formation and destruction of these force chains, where in shear jammed materials these force chains arrest into an anisotropic load bearing configuration.

Only in the last decade has the insight that frictional force chains are chiefly responsible for DST and SJ emerged with new insights that have grown up around it. I will highlight three here but this is far from an exhaustive list. Researchers have modulated the bulk ST and SJ responses by tuning the frictional interactions engineered at the nanoscale properties of the suspended particles to have a greater propensity to interact chemically or sterically(1; 22).

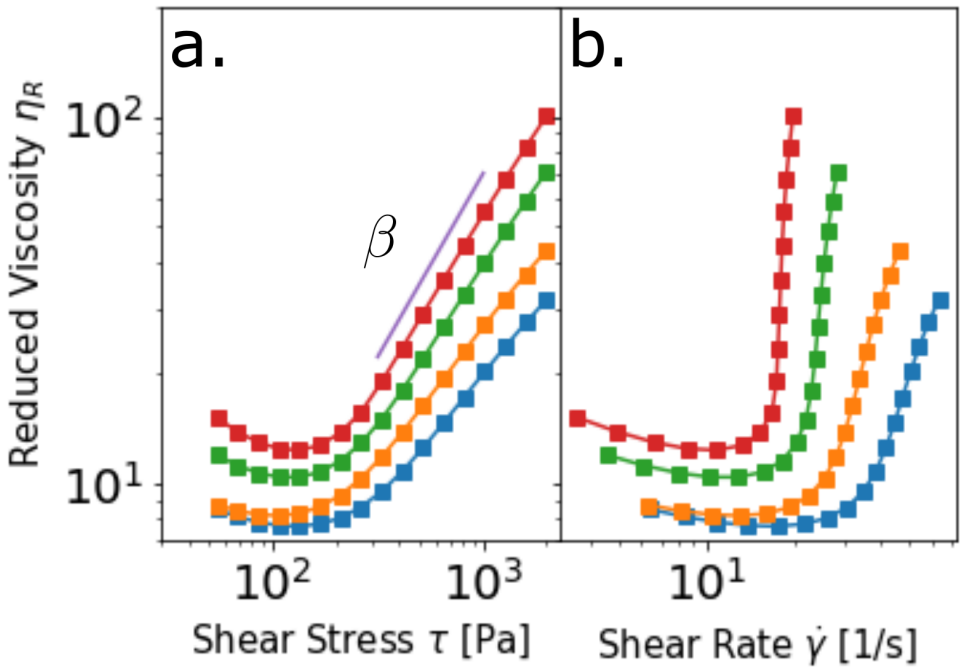

Figure 1.1: Steady state rheometry data from suspensions of Aerosil OX-50 particles in polyethylene glycol 200 (PEG200). Reduced viscosity is plotted as a function of shear stress τ in (a) and as a function of shear rate $\dot{\gamma}$ (b). The black line in (a) has a slope of 1 indicating that the flow curve corresponding to a packing fraction $\phi_v = .332$ is undergoing discontinuous shear thickening (DST), as confirmed by the same curve plotted as a function of shear rate in (b).

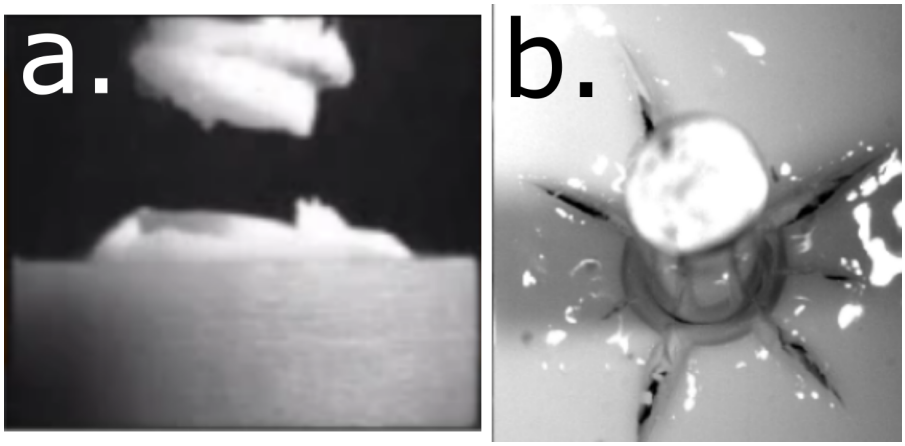

Figure 1.2: Two examples of shear jammed solids showing material failure under applied load. (a) Is an example of a cornstarch suspension undergoing extensional stresses and fracturing into two separate pieces. Picture taken from (1). (b) Example of cornstarch suspension being impaled by a falling rod which drives shear jamming and eventually showing brittle fracture with radial crack patterns. Picture taken from (2) .

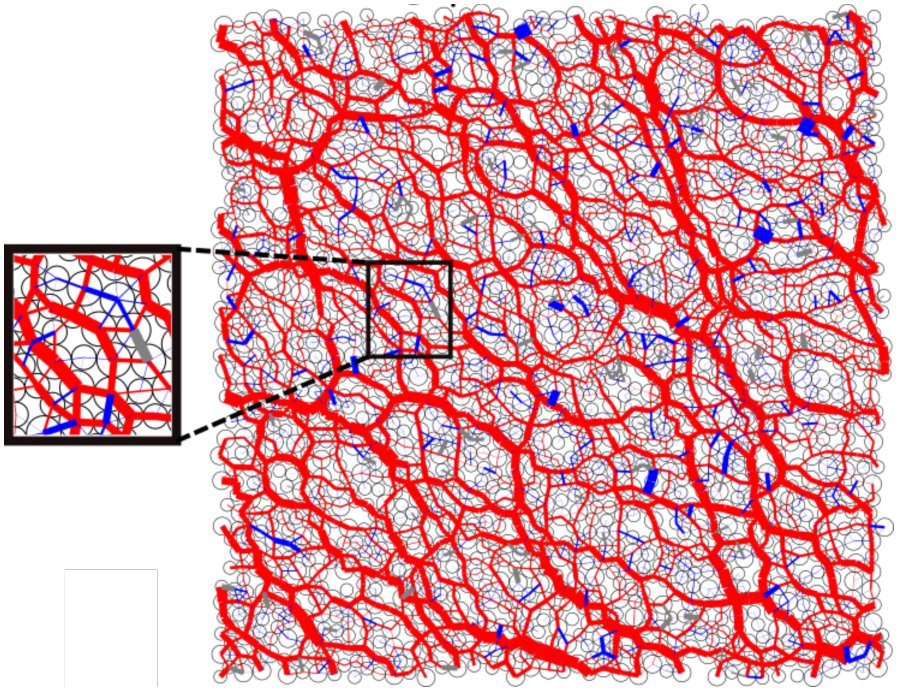

Figure 1.3: Representative snapshot of a simulated 2D dense suspension flow with bidisperse particles in periodic boundary at an area fraction of $\phi = 0.78$ and a normalized imposed stress of $\frac{\tau}{\tau^*} = 100$. Red lines are frictional forces, blue lines are hydrodynamic lubrication forces, grey lines are purely repulsive forces with the width of each line indicating the strength of the interaction. For more information about this simulation see chapter 4.

High stress regions have have been discovered in suspensions undergoing shear thickening using boundary stress measurements that suggest localized transient jamming events (23). Lastly, shear jammed suspensions have been shown to not only solidify under stress but also show different types of solid-like material failure, indicating the yielding of the underlying frictional network (2; 1).

1.2 Phase Behavior of Suspensions

One combination of particles and suspending medium can show CST, DST, and SJ all by tuning either the packing fraction, the stress applied, or both. Producing a steady state phase diagram of this behavior has been done experimentally, computationally, and theoretically and this section will briefly go over each. It should be emphasized that these phase diagrams are for the steady-state behavior of suspensions and this ignores transient phenomena such as start up flows or relaxation dynamics.

1.2.1 Phase Boundaries Measured Experimentally or Computationally

Measuring the phase boundaries between CST, DST, and SJ can be done by preparing a range of volume fractions ϕ for a single suspension system and then measuring every suspension for a range of stresses τ. This sounds simple enough but measurements between the DST and SJ states are difficult as the suspension is transitioning from an incredibly viscous liquid to a solid. Rheometers, the instruments typically used to measure the viscosity of materials, are ill-equipped to study this transition. This is because as the suspension transitions into a solid-state it often does it heterogeneously and will eject from the instrument before the full sample has solidified. One study exists that exhaustively measures this boundary between CST, DST, and SJ. It used a couette cell to overcome the difficulties with ejection and the phase diagram measured from that work is recreated in Fig 1.5a. These phase boundaries are often measured in computational systems where it is straightforward to measure CST,

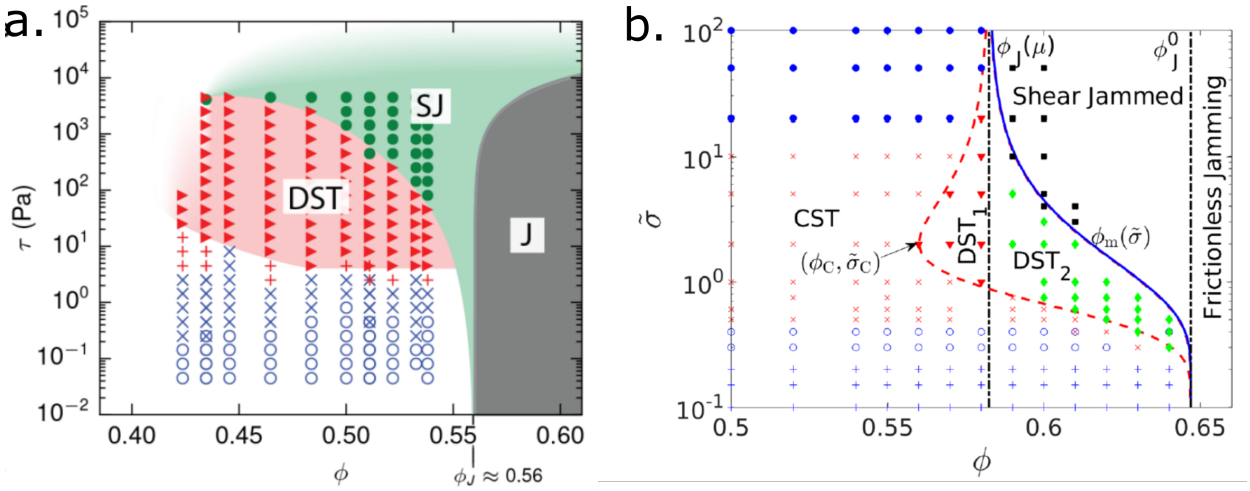

Figure 1.4: Phase diagrams for experimental data from Peters et al. (3) and simulation data taken from Singh et al. (4) (a) Dense suspension phase diagram plotting volume fraction against shear stress for cornstarch particles suspended in a density matched solvent of water and glycerol with cesium chloride dissolved. Phases were determined by a combination of couette cell rheology and particle image velocimetry of the top flows. Red region is where DST was measured, green region is where SJ was measured, data with no color showed CST, and grey region is any volume fraction beyond the jamming point for this system. For more information, including the meaning of the different symbol types, please refer to. (b) Dense suspension phase diagram for simulated data with dimensionless stress on the y-axis and packing fraction on the x-axis. CST flows are all points outside of the DST and SJ region. DST_1 corresponds to DST flows that transition to a liquid at high stresss while DST_2 corresponds to DST flows that transition to SJ solid at high stresses. For more information on the meaning of points and how the solid lines are derived see(4) .

DST, and with some computing power SJ systems as well. An example of a resulting phase diagram from simulations that is then compared with a model phase diagram from the next section is presented in Fig 1.5. Both plots in Fig 1.5 have the same structure which is that there is a region at low stresses and packing fractions that show CST or Newtonian flows, followed by a region that shows DST at higher stresses and packing fractions, and culminating in either shear jammed or jammed states at the highest packing fractions and stresses.

1.2.2 Extracting Phase Boundaries from Wyart-Cates Models

Measuring the phase boundary between DST and SJ either computationally or experimentally, as in the last section, can be incredibly challenging. In simulations the calculations required to evolve the equations of motion near the SJ phase boundary become prohibitively long and measuring the divergence of viscosity and seeing the arrest of the flow experimentally is difficult as ejection from the rheometer and heterogeneous stress profiles leads to pockets of solidified and liquified suspension throughout the sample. This motivates another way of determining the phase boundary, with a popular method being to use theory to extrapolate this boundary from simulations or measurements at lower packing fractions and shear stresses. To do this one needs to first measure the shear thickening response of a suspension system over a range of packing fractions and stresses, as in Fig. 1.1. Then this data is fit to a model, the most common being the Wyart-Cates model (24), and then the fit parameters are used to extract the phase boundaries.

I define a Wyart-Cates' like model as any model of the viscosity of a suspension, η, as a function of volume fraction ϕ and imposed stress τ that has the following form:

$$\eta(\tau, \phi) = \eta_0(1 - \frac{\phi}{\phi_J(\tau)})^{-\alpha}, \tag{1.2}$$

where η_0 is the viscosity of the suspending medium, $\phi_J(\tau)$ is a stress dependent jamming packing fraction, and β is a fit parameter that is usually equal to $\alpha = 2$. In Wyart-Cates' original publication they used $\phi_J(\tau) = (1 - f(\tau))\phi_{SJ} + f(\tau)\phi_0$ where ϕ_0 is the frictionless jamming packing fraction, ϕ_{SJ} is the shear jamming packing fraction, and $f(\tau)$ is the fraction of frictional contacts as a function of stress(24). $f(\tau)$ is usually taken to be a smooth function that satisfies $f(0) = 0$ (no frictional contacts when the stress is zero) and $f(\infty) = 1$ (maximal

frictional contacts at high stress). Often the function

$$f(\tau) = \exp((\frac{\tau^*}{\tau})^\kappa), \tag{1.3}$$

is used, where τ^* is some stress-scale and κ is a fit parameter. Finally, ϕ_0 is the frictionless jamming packing fraction and ϕ_{SJ} is the minimum packing fraction where one can measure SJ.

Measuring $\eta(\tau, \phi)$ for a single suspension system entails measuring the viscosity of multiple suspensions of different ϕ over some range of stress τ, after which one can fit the Wyart-Cates form of $\eta(\tau, \phi)$ using one's favorite fitting method. This will yield as many as five fit parameters β, ϕ_0, ϕ_{SJ}, τ^*, and κ although typically $\alpha = 2$, $\kappa = 1$, and ϕ_0, ϕ_{SJ} can be measured by other mean leaving as little as one fit parameter (τ^*) in $\eta(\tau, \phi)$. Once all the parameters are measured one can extract the phase boundary for both where DST begins and where SJ begins. To do this one imposes the condition $\frac{d\eta}{d\dot{\gamma}} = \infty$ and solves for $\phi(\tau)$ for the DST boundary and imposes $\eta = \infty$ for the SJ boundary. This is done in the appendix A but the result for a general Wyart-Cates model as defined above is given by:

$$\phi_{DST}(\tau) = \frac{\phi_J^2(\tau)}{\phi_J(\tau) - \alpha\tau\phi_J'(\tau)} \tag{1.4}$$

and

$$\phi_{SJ}(\tau) = \phi_J(\tau). \tag{1.5}$$

for the DST and SJ boundaries, respectively. If we use $\phi_0 = 0.85$, $\phi_{SJ} = 0.795$, $\tau^* = 1.5Pa$, $\alpha = 2$, and $\kappa = 1$ we get Fig. 1.5 where $\phi_{SJ}(\tau)$ is the green line and $\phi_{DST}(\tau)$ is the dashed purple line. The purple region is where the model predicts one would measure DST, the green region is where SJ occurs, and the grey region is where isotropic jamming happens as those are where the packing fractions exceed the frictionless jamming packing fraction, $\phi > \phi_0$. These models have been done a reasonable job of fitting experimental data and a

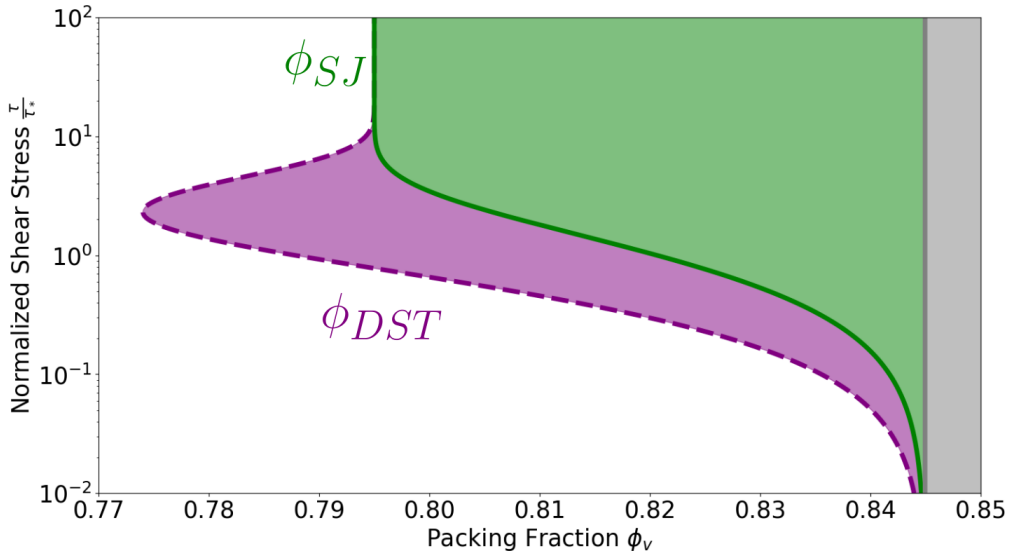

Figure 1.5: Phase diagram from a Wyart-Cates model that uses $\phi_J(\tau) = (1 - f(\tau))\phi_{SJ} + f(\tau)\phi_0$ with $f(\tau) = \exp((\frac{\tau^*}{\tau})^\kappa)$. For model parameters I used $\phi_0 = 0.85$, $\phi_{SJ} = 0.795$, $\tau^* = 1.5Pa$, $\alpha = 2$, and $\kappa = 1$. $\phi_{DST}(\tau)$ is shown in the dashed purple line and $\phi_{SJ}(\tau)$ is the solid green line.

better job of fitting data from simulation.

1.3 Thesis Overview

I have organized this thesis so that it begins with how I performed the experiments that I did during my PhD and then the following chapters are the research that I performed. In the next chapter I describe how to prepare suspensions in detail as well as how to decide which rheometer geometry is the best to use for a particular experiment. Chapter Three is based on the paper I published in my third year in Soft Matter titled "The role of solvent molecular weight in shear thickening and shear jamming". This paper outlines how solvation forces can be used to tune both the shear thickening and shear jamming response of a system of fumed silica suspensions. Chapter 4 is based on a paper that has just been accepted into Nature

Physics, titled "Minimally Rigid Clusters in Dense Suspension Flow", where I use a rigidity metric originally used in dry granular matter to establish a new region of dense suspension phase space. Chapter 5 is the last chapter of research and is unpublished work that pertains to the rheology of suspensions of different starch suspensions. I use rheology and modeling to estimate the phase behavior of potato starch, cornstarch, and wheat starch suspensions. Finally, I conclude and summarize follow by an outlook on the field of suspension science generally. Additionally, the chapters 3, 4, and 5 have corresponding appendices A, B, and C, respectively.

CHAPTER 2

SHEAR RHEOLOGY EXPERIMENTS

2.1 Introduction

This chapter provides information on how to both prepare and measure dense suspensions, as well as common pitfalls to avoid. For this chapter to be most useful I strongly recommend getting trained on a rheometer and doing some simple measurements. Another great resource for getting started when measuring dense suspensions the chapter titled "Experimental challenges of shear rheology: how to avoid bad data" in the book "Complex Fluids in Biological Systems" or watch Randy Ewoldt's Youtube video where he goes over the salient points(25). Additionally, Macosko's book on rheology is an indispensable resource for anyone doing any rheology measurements (26). At the time of this writing there is only one edition but I have heard a rumor that Christopher Macoscko, Gareth McKinley, and Randy Ewoldt are currently writing edition 2.

2.2 Sample Preparation

Before measuring anything in a rheometer it is important to first make sure the sample is worth measuring, This seemingly simple task of mixing solid particles into a suspending solvent can range from an incredibly easy and taking only a couple of minutes to a difficult multi-day endeavor. Suspensions that are not well mixed will show thixotropy (viscosity changes with shear history) as measuring them further disperses the particles, changing the sample viscosity. Some mixtures of particles and solvent will never form suspensions; an instructive example is to imagine "sticky" hydrophobic particles in water. In that system, the particles will always have a greater affinity for each other than the solvent and therefore will aggregate. Provided that the combination of particles and solvent will form a suspension, this section contains strategies for how to fully disperse those particles in the solvent and

determining if the particles are well dispersed. This section is split into the preparation of suspensions with "larger" particles ($\gtrsim 1um$) and the preparation of suspensions with "small" particles ($\lesssim 1um$); this distinction is necessary as preparation of the first is relatively straightforward while the latter is much more difficult.

It is important to have a good scale when preparing dense suspensions as the relative amount of suspending particles to solvent, measured as a mass fraction, ϕ_m, or more commonly as a volume fraction, ϕ_v, is one of the most important quantities determining rheological behavior. More accurate scales allow for greater precision when determining ϕ_m and ϕ_v. This precision becomes most important when working with suspensions near their jamming packing fractions, ϕ_J, as near this volume fraction the viscosity begins to diverge. To determine what precision is required, it is useful to calculate the error in ϕ_v or ϕ_m. For example, ϕ_v is given by:

$$\phi_v = \frac{V_P}{V_P + V_S}, \tag{2.1}$$

where V_P is the volume of particles and V_S is the volume of the solvent. Usually, neither of these quantities are known directly but what is known is the densities of the solvent and suspended particles as well as their relative masses so it is possible to calculate ϕ_v as

$$\phi_v = \frac{V_P}{V_P + V_S} = \frac{\frac{\rho_P}{m_P}}{\frac{\rho_P}{m_P} + \frac{\rho_S}{m_S}}, \tag{2.2}$$

where ρ_P and ρ_S are the densities of the particles and solvents, respectively, and m_P and m_S are the masses of the particles and solvents, respectively. With ϕ_V being function of the densities and masses we can now propagate the error in those measured quantities to get the error for the packing fraction, $\delta\phi_V$, assuming that there are no correlations between any of the measured quantities this will be given by

$$\delta\phi_V = \sqrt{\delta\rho_P^2(\frac{\partial\phi_V}{\partial\rho_P})^2 + \delta\rho_S^2(\frac{\partial\phi_V}{\partial\rho_S})^2 + \delta m_P^2(\frac{\partial\phi_V}{\partial m_P})^2 + \delta m_s^2(\frac{\partial\phi_V}{\partial m_s})^2}, \tag{2.3}$$

where $\delta\rho_P$ and $\delta\rho_S$ are the uncertainties in the densities of the particles and solvents, respectively, and m_P and m_S are the uncertainties in the masses of the particles and solvents, respectively. It is easy to make mistakes when calculating $\delta\phi_V$ by hand so it is recommend to do this calculation in Mathematica. Doing this computationally also allows for easily tuning the values of ρ_P, ρ_S, m_P, m_S, and their respective uncertainties to find the value of $\delta\phi_V$, the precision in ϕ_V, that is required.

There are a couple of useful tools when making suspensions besides the obvious scale and mixing spatula. This section assumes that preparation of approximately milliliters of suspension, for larger samples some of these methods are going to be altered. The first tool is a sonicator, preferably one that can run indefinitely it does not have to be continually turned back on. Keeping samples in a sonicator is a good passive way to mix samples. The second is a centrifuge, which is useful for separating particles and solvent but also for early stages of mixing nanoparticle suspensions which will be explained later. Finally, if working with easily aersolized powders then working is a fume hood is required.

Lastly, I want to caution against two tools that might seem useful in preparing suspensions but are either too effective or ineffective. First and foremost is a tip sonicator, which works by putting a piece of metal into a sample and then driving it at ultrasonic frequencies. These are not for mixing, but instead for destruction. They have been observed to fuse together iron particles that are in suspension and destroy suspended carbon nanotubes. If it can shatter a carbon nanotube, it can likely irreparably damage suspending particles or degrade solvent. The last tool I will caution against are roll mixers or any large amplitude mixer. These work well if mixing large samples of suspension or if the suspending solvent viscosity is very low. But for small samples in viscous suspending solvents I have found that time in a sonicator is much more effective.

2.2.1 Large Particle Suspensions ($\gtrsim 1um$)

Suspensions of large particles such as cornstarch suspended in water or large silica particles ($1um <$) in glycerol are very easy to prepare. It is so easy that oobleck (suspensions of cornstarch and water) is a common physics demo for kids of all ages as the directions for preparing it is to simply mix cornstarch and water until there is no visible dry powder remaining. While these simple directions give qualitatively reproducible results for a physics demos, it can be difficult to get quantitively reproducible rheology from cornstarch suspensions without some care. These difficulties stem from cornstarch particles ageing in almost all solvents as the particles slowly adsorp solvent which slowly inflates the particles and increases the packing fraction. Additionally there is a decent variation in polydispersity and mean particle size from batch to batch of cornstarch particles, even when buying from laboratory suppliers such as Sigma-Aldrich. These two facts mean that to fairly compare rheology between two cornstarch suspensions one should 1. adhere to a strict preparation protocol so that the two suspensions have aged approximately the same amount and 2. use particles come from the same batch of cornstarch.

In addition to particle swelling, which can occur in nanoparticle suspensions as well, a unique difficulty of measuring large particle suspensions is that they sediment over long time scales. We can estimate this timescale given the density of the particle ρ_r, the radius of the particle R_p, the density of the fluid ρ_f, the fluids viscosity η_0 one can calculate the terminal sedimentation velocity of the particle $v_T = \frac{2(\rho_p - \rho_f)gR_p^2}{9\eta_0}$. Assuming our particle attains this speed immediately and that it needs to sediment a length L before reaching the bottom of the container our sedimentation timescale becomes:

$$t_{sediment} = \frac{9\eta_0 L}{2(\rho_r - \rho_f)gR_p^2}. \tag{2.4}$$

Ultimately we need this timescale to be much greater than the timescale of our rheology

experiment and so it is best to try to maximize this timescale.

Looking at the equation for $t_{sediment}$, the most obvious strategy to maximize $t_{sediment}$ is is to density match the particles and fluid $\rho_p \approx \rho_f$. This is possible for suspensions of starch particles in water by dissolving salts, such as cesium chloride, to increase the density of the water. But for silica particles with a density of $\rho \approx 1.8\frac{g}{cc}$ it becomes much more difficult to find liquids that have these densities. For silica particles or other dense particles we can use very viscous solvents so that η_0 is maximal, such as glycerol. Finally, working with smaller particles drastically increases $t_{sediment}$.

2.2.2 Small Particle Suspensions ($\lesssim 1um$)

Nanoparticle suspensions are often substantially harder to disperse than larger particle suspensions. Typically requiring tens of minutes of manual mixing followed by hours and sometimes days of sonication and further manual mixing. For concreteness,in this subsection I will outline how I mix suspensions of fumed silica into polar solvents, such as ethylene glycol (EG) or some polymer of EG, at high concentrations (mass fractions exceeding 50 percent) of fumed silica. This is an instructive system because it is by far the most difficult system to mix that I encountered during my PhD.

I would begin by massing out the desired proportion of fumed silica and EG into a vial that is contained inside of fume hood, as fumed silica is an annihilation hazard. I would then use a small spatula to combine the dry powder and the solvent as best as possible by stirring the vial while holding it under the fume hood. Once all the dry powder has been incorporated, the suspension will be a very stiff gel and will be more solid than liquid. Continue mixing until the opaque gel melts into a clear liquid, this process can take upwards of 20 minutes and like kneading dough to make bread, it can be useful to set a timer. While mixing the gel it will occasionally get coated onto the walls of the vial making mixing difficult, when this happens I would put the vial in a centrifuge for less than a minute to collect the

gel at the bottom of the vial.

Once the gel has been mixed into a viscous liquid I would begin to measure the suspension to determine if it is well mixed. This consists of cycling between measuring the suspensions viscosity then mixing it further and measuring it again to see if the viscosity has changed after further mixing. Once reaching a state where the viscosity measurements do not change with further mixing, I would consider the suspension well mixed. For the fumed silica suspension that I was referring I would typically measure the viscosity of the suspension with a forward and backward stress ramp using a parallel plate geometry followed my manual mixing of the suspension and three or four hours of sonication before measuring again. This is a general strategy to determine if a suspension is well mixed, the viscosity measurement should be reproducible after further mixing. In particular, as the suspension becomes further mixed the viscosity should decrease as the aggregation of particles breaks down the and particles become suspended. As the material is further mixed the onset stress for shear thickening increases as the particle size is decreasing and the onset stress for shear thickening scales as $\tau_0 \sim \frac{F_0}{a^2}$, where F_0 is a repulsive force at particle-particle contact and the a is the radii of the two particles.

If the materials viscosity does not go down after further mixing or does not show shear thickening at all it is possible that the suspension has flocculated and/or that the suspension is thixotropic or antithixotropic. A flocculated suspension is typically one where the particle-particle interaction exceeds that of the particle-solvent to the point that it is impossible to suspend the particles in the solvent as the particles instead aggregate. Thixotropic or antithixotropic suspensions have a viscosity that depends on the shear history of the suspension and therefore one should apply a pre-shear to the suspension before measuring to standardize the shear history between samples.

2.3 Measurement Geometry

The first choice when using any rheometer is what measurement geometry one uses. The most commonly used for measuring dense suspensions are parallel plate, cone and plate, and concentric cylinders, as shown in Fig. 2.1. These geometries all have their pros and cons which I will go over below, but all fundamentally work in the same way by measuring a torque M and an angular rotation rate $\dot{\omega}$ and converting them into a shear stress τ and a shear rate $\dot{\gamma}$. This allows for a measurement of the shear viscosity $\eta = \frac{\tau}{\dot{\gamma}}$. Both the equations themselves and their derivations can be found Macosko's book on rheology (26) and taking a look at the equations before using a particular geometry is generally a good idea. By understanding how to derive these equations one will understand the limitations of the rheometer by seeing the assumptions that are required for calculating the shear rates and shear stresses in each geometry. Before going into detail on the pros and cons of the three most common measurement geometries, I will go over some relevant information for every geometry.

All of the three geometries shown in Fig. 2.1 work by placing a material in a gap between a moving and a fixed surface. Ordering of the suspeded particles near the fixed surface can lead to irreproducible and incorrect results, so best practice is that the gap exceed ten times to the size of the suspending particle. This is especially relevant when measuring larger particle suspensions such as cornstarch where the particle size can be as large as 40um, necessitating a gap of at least 0.4mm. Another potential artifact is wall slip, where the fluid layer touching the moving surface moves at a speed slower than that of the moving surface. In order to eliminate wallslip sandpaper can be bought with adhesive backing that can be attached the the rheoemeter surface. This roughened surface will stop wall slip and the data with the roughened rheometer surface can be compared to the data taken with non-roughend surface and large mismatches can indicate wallslip is present. A final artifact that is endemic to every geometry is either evaporation of the suspending solvent

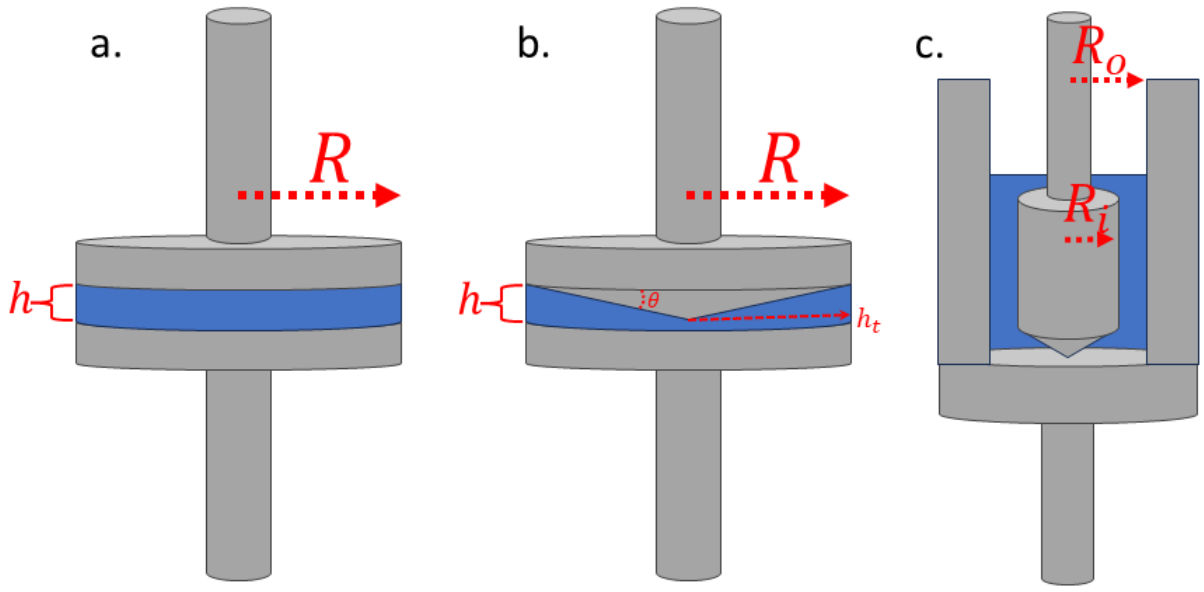

Figure 2.1: Most common rheometer geometries used when measuring dense suspensions where the sample is depicted blue, components of the rheometer in grey, and relevant geometry lengthscales labeled in red. (a) Parallel plate geometry. (b) Cone and plate geometry, both θ and h_t are exaggerated in this picture. Typically θ is between 1° and 2° while h_t is often around $50um$ (c) Concentric cylinders otherwise known as a Couette cell.

or adsorption of water vapor. Both lead to irreproducible results as the packing fraction of the suspension increases with time. To avoid evaporation one can use non-volatile solvents such polyethylene glycol or polyproplyene glycol or use temperature and humidity controls. A common attachment for any geometry is a solvent trap that insulates samples from the environment allowing for minimal evaporation. Avoiding solvent adsorption can be achieved by either doing measurements much faster than the timescale of adsorption or working with non-adsorbing particles such as as silica.

2.3.1 Parallel Plate Geometry

Parallel plate shear rheology, as depicted in Fig. 2.1a, consists of putting a sample between two parallel plates of radius R with gap height h and then shearing the top or bottom plate with shear rate $\dot{\gamma}$ or shear stress τ.

One convenience of the parallel plate geometry is that the experimentalist gets to choose the measurement gap height h and it typically ranges from $.1mm$ to $1mm$. When measuring any fluid in either a parallel plate or cone and plate rheometer one has to be careful to avoid surface instabilities and eventual ejection at the free surface. These instabilities form when the centrifugal force begins to approach the surface tension that confines the suspension. To avoid these instabilities it is best to determine the minimum shear stress at which these instabilities form by visually inspecting the free surface during an increasing ramp of shear stress. The shear stress where the instability begins to form is where the data from the rheometer becomes less reliable, as the boundary conditions assumed to derive our expressions for shear stress and shear rate are no longer true. Empirically I have found that decreasing the measurement gap height increases the stress where the instability occurs, so minimizing the measurement gap height (while not going below 10 particle diameters) is typically best practice when measuring high stresses. Both the parallel plate measurement geometry and the cone and plate measurement geometry in the next section have the benefit of using minimal sample and therefore are best for suspensions where the components are in short supply.

2.3.2 Cone and Plate Geometry

Cone and plate shear rheology, as depicted in Figure Fig. 2.1b, consists of putting a sample between two parallel plates of radius R with gap height h and then shearing the top plate with shear rate $\dot{\gamma}$ or shear stress τ. Unlike the parallel plate rheometer the gap height is fixed to a relatively small height, for the tool in our lab it is mm. Since this gap is small and non-negotiable this geometry is mainly used for nanoparticle suspensions where one can have more than ten particles underneath the lowest level of the gap and thus avoiding the aforementioned ordering near boundaries artifact. This fixed gap height can make measurements difficult as the experimenter needs to guess how much suspension needs to be put on the

bottom plate and if they underestimate they have to reload the sample and if they overestimate they have to trim the excess sample off the boundary. Because of the applicability of this geometry exclusively nanoparticle suspensions and the difficulty of these measurements the cone and plate geometry is mainly used when one is interested in measuring the first normal stress difference $N_1 = \tau_{11} - \tau_{22}$. This quantity is presently only accessible using this measurement geometry and for suspensions it is conjectured that it is a measure of the amount of frictional contacts in the system (27).

2.3.3 Concentric Cylinder Geometry

In the concentric cylinder geometry the sample fills a cup of radius R_{out} and a bob of radius R_{inner} is lowered into the filled cup, as depicted in Figure Fig. 2.1c. This geometry requires a sample volume that is orders of magnitude greater than the previous two geometries and therefore is not often used for suspensions with custom synthesized particles that are usually made in small batches. The main benefit of this geometry is that there is no free boundary for the suspension to eject from and therefore out of the previous two geometries this is the best geometry to measure shear jamming suspensions (9). Furthermore, as the gap between the inner and outer cylinder is often on the order of a 1cm it is possible to measure suspensions large particles without worrying about ordering near the walls. One of the main difficulties in using this geometry is when lowering the inner cylinder into the suspension the normal forces on the inner cylinder can be so large that they can damage the normal force sensor of the tool. To avoid damaging the rheometer one must lower the tool into the suspension very slowly to avoid the extensional shear thickening and/or shear jamming response. This process can be sped up by occasionally turning the rheometer tool which lowers the normal force on the tool. For dense starch suspensions it can take tens of minutes to submerge the tool to the measurement height.

CHAPTER 3

THE ROLE OF SOLVENT MOLECULAR WEIGHT IN SHEAR THICKENING AND SHEAR JAMMING

3.1 Introduction

In this Chapter, we measure the rheology of fumed silica particles suspended in polyethylene glycol (PEG) of various molecular weights (MW) in the olgermic limit. We find that increasing the MW of the PEG induces stronger shear thickening and elicits shear jamming. We propose a mechanism for this observed change in rheology by considering solvation forces and how they inhibit the formation of frictional contacts. This leads to a simple way to predict the rheology of a shear thickening suspension given knowledge of how the solvent molecules and surface of the suspending particles interact chemically. These ideas are not only validated by our rheological results but also supported by measurements found in the literature from rheology, atomic force microscopy, and surface adsorption studies.

Over the past decade, simulations and experiments have shown that discontinuous shear thickening (DST) and shear jamming (SJ) are macroscopic consequences of microscopic stress-activated frictional contacts between particles which constrain their relative motion (28; 4; 29; 21; 6; 11). Initially “lubricated" particle contacts are converted into “frictional" contacts by the mechanical stress applied (14; 30). Increasing the applied stress increases the fraction of frictional contacts and eventually generates “force chains" of particles that underlie dramatic increases in viscosity and jamming behavior (7; 31; 20). Taking cues from dry granular physics, much work has focused on factors that directly modify the frictional

. The research described in this chapter has been published in: van der Naald, M., Zhao, L., Jackson, G. L., and Jaeger, H. M. The role of solvent molecular weight in shear thickening and shear jamming. *Soft Matter* 17, 3144-3152 (2021).

properties of surfaces such as changing the sliding friction (or rolling friction) coefficient and related experimental studies which have investigated the effects of particle roughness, size, aspect ratio, or surface chemistry (32; 1; 33; 34; 35; 36; 37; 38; 12). However, the fundamental difference between dry granular media and a suspension is the presence of a suspending liquid, the solvent, which wets and lubricates each particle. The transition to a "frictional" particle contact thus necessarily involves displacement of the intervening solvent and desolvation of the particle surface. As such, for a given solvent its chemical properties such as molecular weight or pH are important and easily tunable parameters that can affect the nature of frictional contacts between particles.(39)

Though the role of polymeric solvent molecular weight (MW) in strongly shear-thickening (nearly DST) suspensions has been investigated in several prior studies, the outcome has not been clear. Some of these studies found that increasing the MW diminishes shear thickening (40; 41; 42), while others show that it enhances shear thickening instead (43; 44). Specifically, for glass or zirconium dioxide particles in silicone oil, Xu et al. found that increasing the MW of the oil led to a smooth crossover from highly non-Newtonian, essentially DST behavior to completely Newtonian flow (40). Conversely, studies by Raghavan et al., using fumed silica in polypropylene glycol (PPG), showed that increasing the MW led to more pronounced non-Newtonian behavior, from continuous shear thickening (CST) to nearly DST (44). These findings indicate some of the complexity associated with the interactions between particle surfaces and the solvent molecules. To gain further insight, we here extend earlier investigations in two ways. First, we focus on the limit of very small MW so that we can track the evolution of suspension behavior as the solvent molecules are increased in chain length from monomers to oligomers. Second, we extend the upper range of applied shear stress in order to go beyond the DST regime and test how SJ is affected by changing the solvent.

Our experiments use fumed silica particles suspended in polyethylene glycol (PEG). Com-

pared to other materials often used in studies of shear thickening that are available in bulk quantities, such as cornstarch, fumed silica has the advantage that DST can be observed at very low packing fractions, due to the particles' highly non-spherical shape. Fumed silica also is non-porous and has a well-controlled surface chemistry. As solvents we use three different molecules of similar chemical structure, but increasing number n of ethylene oxide repeat units: ethylene glycol (EG, $n = 1$), PEG-200 ($n \approx 4$), and PEG-400 ($n \approx 8$). We characterize the steady-state flow behavior of these fumed silica suspensions using a stress-controlled rheometer in parallel plate geometry. At identical volume fractions, we observe the least shear thickening in EG, followed by PEG-200, and the strongest shear thickening in PEG-400. We use high-speed ultrasound imaging to visualize the transient flow fields under impact. While we observe a localized flow field around the impactor typical of a viscous, fluid-like response for EG suspensions, PEG-200 suspensions yield extended, highly correlated motion indicative of a shear jammed solid. This result constitutes the first direct observation of propagating jamming fronts associated with shear jamming in a fumed silica suspension. We then develop a scenario in which we relate the propensity of forming frictional interparticle contacts to the strength of solvation layers surrounding the particles. We use this to explain both the observed enhancement of non-Newtonian stress response for n up to 8 and its demise for larger n.

3.2 Materials and Methods

3.2.1 Suspension Preparation

The solid particles used in this study are fumed silica (Aerosil® OX50, Evonik) with specific density $\rho = 2.2\text{g cc}^{-1}$. They are aggregates of 40 nm glass spheres that irreversibly fused during the manufacturing process to form irregularly shaped particles approximately 500 nm in size.

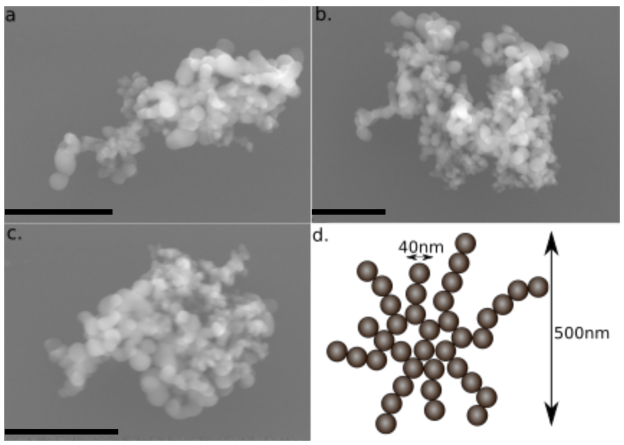

Figure 3.1: (a)-(c) Representative SEM micrographs Aerosil OX50 aggregates. Each scale bar is 500nm. d. Schematic illustration of a fumed silica aggregate composed of smaller primary silica particles (40nm) that fused together. The average aggregate is 500nm with a broad size distribution.

Representative scanning electron microscope (SEM) pictures of these aggregates are shown in Fig. 3.1(a-c) while a schematic of the particles is shown in Fig. 3.1(d). We suspended these particles in ethylene glycol (EG) (Fisher Chemical, MW = $67.07\frac{\text{g}}{\text{mol}}$), PEG-200 (Alpha Aesar, average MW = $200\frac{\text{g}}{\text{mol}}$), and PEG-400 (Sigma-Aldrich, average MW = $400\frac{\text{g}}{\text{mol}}$). These solvents are linear chains containing n ethylene oxide repeat units. We measured the viscosity of each solvent η_0 to calculate the reduced viscosity of our suspensions, $\eta_R = \frac{\eta}{\eta_0}$, and ensure that each solvent is a Newtonian fluid, as shown in figure S2. For EG, $n = 1$, while on average, PEG-200 has $n = 4$ and PEG-400 has $n = 8$. We needed to make large amounts of suspension ($\approx$ 100 mL) for our impact experiments and smaller amounts ($\approx$ 1 mL) for steady-state rheometry. We found that large quantities required much longer mixing times. For this reason we developed two suspension preparation protocols described below. To determine the packing fraction ϕ_v we weighed both the solvent and solid particles using an analytical balance and converted to volumes fractions using their respective densities. Since our particles are porous amorphous aggregates, some of the suspending liquid is inside the particle and the packing fractions reported here should be regarded as effective packing frac-

tions. For small volumes of suspension ($\approx$ 1 mL), the mixture was stirred manually with a spatula until all dry powder had been mixed in. ***Caution:*** *Dry fumed silica powder is easily fluidized and represents an inhalation hazard.* Therefore, all handling of fumed silica powder was conducted in a fume hood. Subsequently, large air bubbles were removed by placing the suspension in a centrifuge at 1000 rpm for 1 minute. The samples were then placed in a water bath sonicator at 40 kHz and 130 W for six hours. These lengthy mixing and sonication times were necessary to ensure that micron-scale agglomerates of particles were broken up and individual particle aggregates (Fig. 3.1) were well-dispersed, a key requirement for reproducible rheometry.

For large amounts of suspension ($\approx$ 100 mL), the particle-fluid mixture was stirred using an overhead mixer in a fume hood at 200 rpm until there was no more visible dry powder, usually taking two hours. Mixing for extended periods of time at such high rotation rates introduced large air bubbles into the suspension. These were especially problematic in impact experiments, as they strongly scatter sound waves and significantly limit ultrasound imaging quality. In order to debubble our suspension, we sealed it and placed it on a 3Hz linear shaker for five hours. This removed all of the large air bubbles but left a number of evenly distributed very small air bubbles, which then served as tracers during ultrasound imaging.

3.2.2 Steady State Rheology

Steady-state shear experiments used a stress-controlled Anton Paar MCR301 rheometer with a parallel plate (25mm in diameter) geometry. All experiments were performed within a temperature range of 22-25 °°C and all runs were conducted less than one hour after sonication. The gap size between the parallel plates was set as needed, but kept between 0.1-0.2 mm, which we found helped in accessing higher stresses without sample ejection. Before measurements we applied a pre-shear at constant shear rate $50\frac{1}{\text{s}}$ for 200 s to a produce homogeneous starting condition for all samples. To check for wall slip, we measured our highest packing

fractions in PEG-200 and PEG-400 in a 25mm parallel plate geometry at two different gap heights, 25mm parallel plate geometry with roughened top and bottom plates at two different gap heights, and a 25mm cone and plate geometry with roughened top and bottom plates shown in Figure. S1. While there was some deviation between the different geometries, this is mainly in the low stress behavior which we found to be dependent on how the plates were roughened, the gap size, and whether we imposed a constant stress or constant rate. This indicates that the low stress behavior in these systems is delicate and requires future study but the enhancement of shear thickening with increasing MW is independent of measurement geometry or boundary roughness. Note that, despite the high shear rates used in our measurement, the high viscosity of the suspending liquid ensures that we are operating well below the regime where secondary flows emerge. Additionally, the highest particle Reynold's number reached was $0.00005 \ll 1$, meaning that particle inertia can safely be neglected. We checked for edge fracture in all of our samples using a high speed video camera (Phantom v12) equipped with a 200 mm lens to observe the sample edge during our rheological measurements. We did not observe edge fracture as observed in polymeric systems (45) but instead observed portions of the suspension-air interface change in reflectivity and surface texture, as also previously observed by video in suspensions in the DST regime just before jamming (46; 47).

3.2.3 Impact Experiments

To study the transient behavior, we used high-speed ultrasound imaging to track the flow field inside the suspension under impact (11; 48; 10; 49). The setup is illustrated in Fig. 3.2. The suspension was placed in a 3D-printed cylindrical container with an inner diameter of 5 cm. An impactor driven at adjustable speed U_p by a linear actuator (SCN5, Dyadic Systems) was mounted above the container. The impactor employed a cylindrical rod with a hemispherical cap of diameter 1 cm. An ultrasound transducer (Philips L7-4) was placed

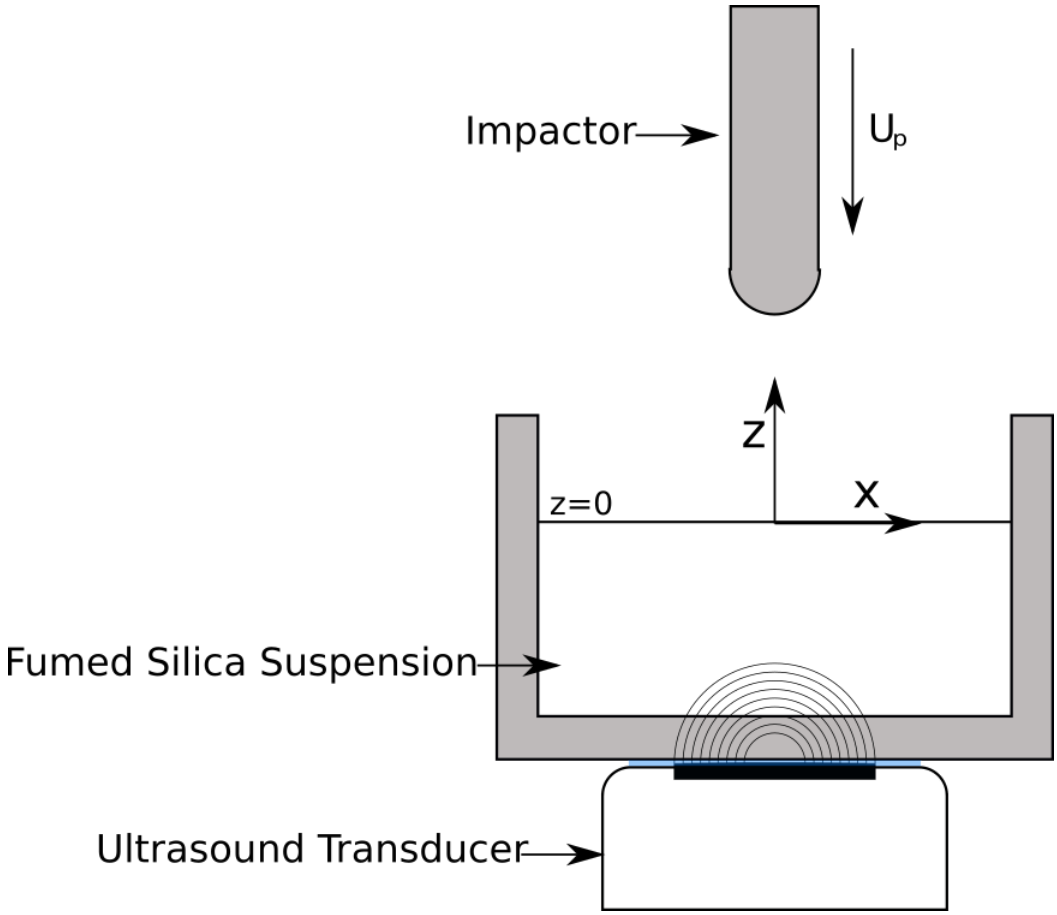

Figure 3.2: Schematic of the impact experiments. The suspension is placed in a cylindrical container of diameter 5.0 cm and impacted with a rod that has a hemispherical cap of diameter 1.0 cm. Once the impactor approaches the suspension surface, ultrasound imaging at 4,000 frames per second is triggered and provides a video of a slice of the flow-field in the x-z plane.

under the bottom of the container, coupled acoustically through a layer of ultrasound gel. This transducer consisted of a linear array of 128 piezoelectric elements and was aligned along the x direction.

In the experiments reported here, the rod moved vertically downward along the central axis of the container at constant speed $U_p = 300\frac{\text{mm}}{\text{s}}$ and impacted the suspension directly above the transducer. Ultrasound imaging was triggered to begin when the rod reached a position 1 mm above the surface of the suspension and collected 500 consecutive frames at a rate of 4000s^{-1}. The impactor pushed vertically 15 mm deep into the suspension, so that it stopped before the ultrasound imaging ended . The images are 2D slices in the x-z plane under the rod, as displayed in Fig. 3.2. Impact experiment were repeated nine to fifteen times for each suspension, and the resulting flow fields, extracted from particle image velocimetry (PIV), were averaged. After each impact, the suspension was fully relaxed by stirring with a spatula as well as by gently shaking and rotating the container.

3.3 Results

3.3.1 Steady State Rheology

In Fig. 3.3a and 3.3b we plot the flow curves for four different packing fractions ϕ_v, reported as shear stress τ, versus reduced viscosity $\eta_R = \frac{\eta}{\eta_0}$ for both PEG-200 and EG. Here η_0 is the viscosity of the suspending solvent. The upper limit in each case was chosen such that we could measure the greatest extent of thickening without sample ejection or free surface deformation during or after each test. All curves in Fig. 3.3 are an average of two forward and backwards ramps; that they all lay approximately on top of each other indicates that we were sampling the steady state viscosity. Error bars are calculated from the standard deviation in the forward and backward ramp and are on the order of the marker size.

All suspensions show shear thinning at low stresses followed by a minimum in the viscosity

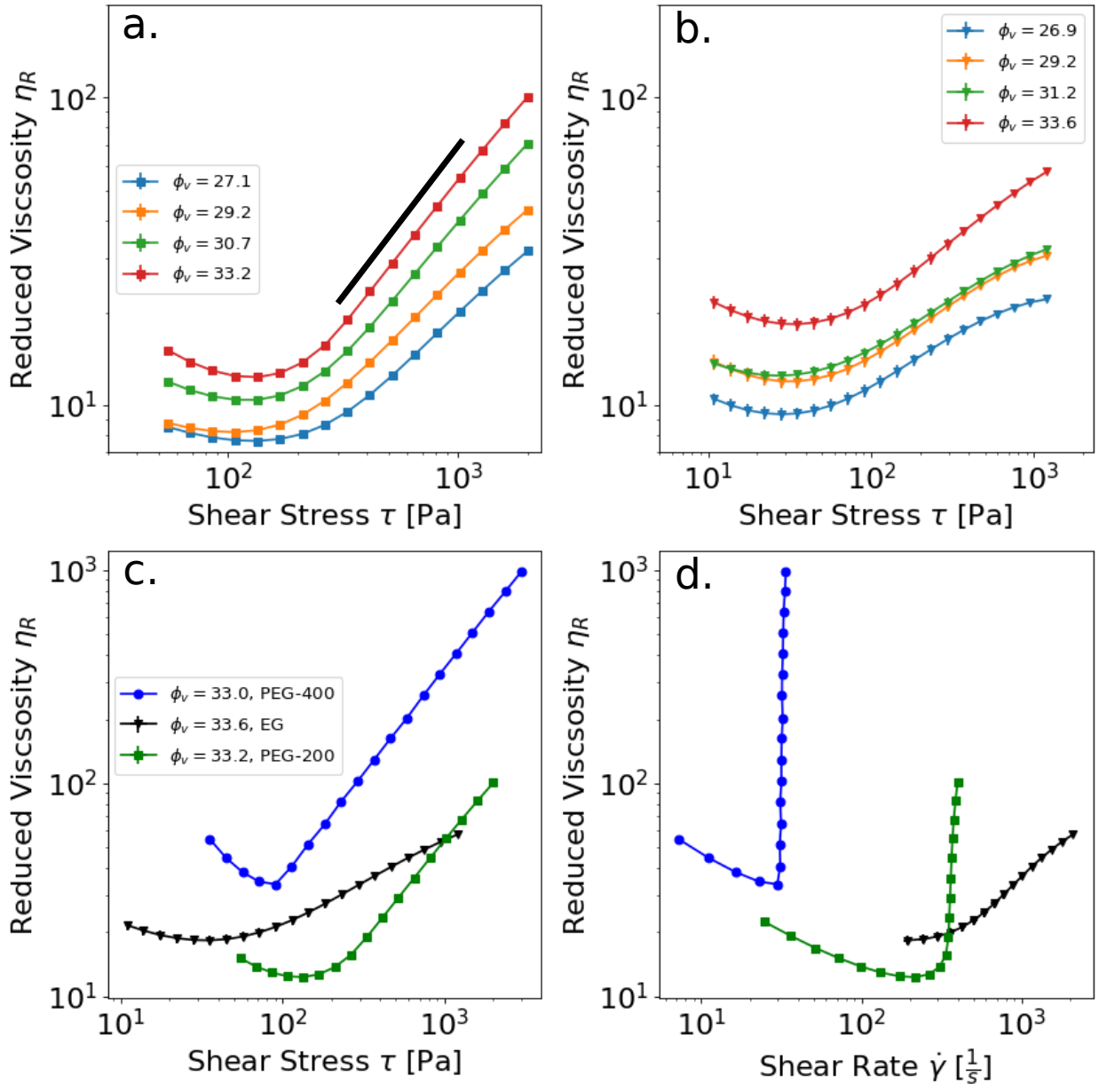

Figure 3.3: Steady state rheometry data from suspensions of Aerosil OX-50 particles. Viscosity is plotted as a function of shear stress in PEG-200 (a) and EG (b). The black line in (a) has a slope of 1 indicating that the flow curve corresponding to a packing fraction $\phi_v = .332$ is undergoing discontinuous shear thickening (DST). Viscosity curves for solvents of different MW but similar packing fraction are plotted as a function of shear stress (c) and shear rate (d).

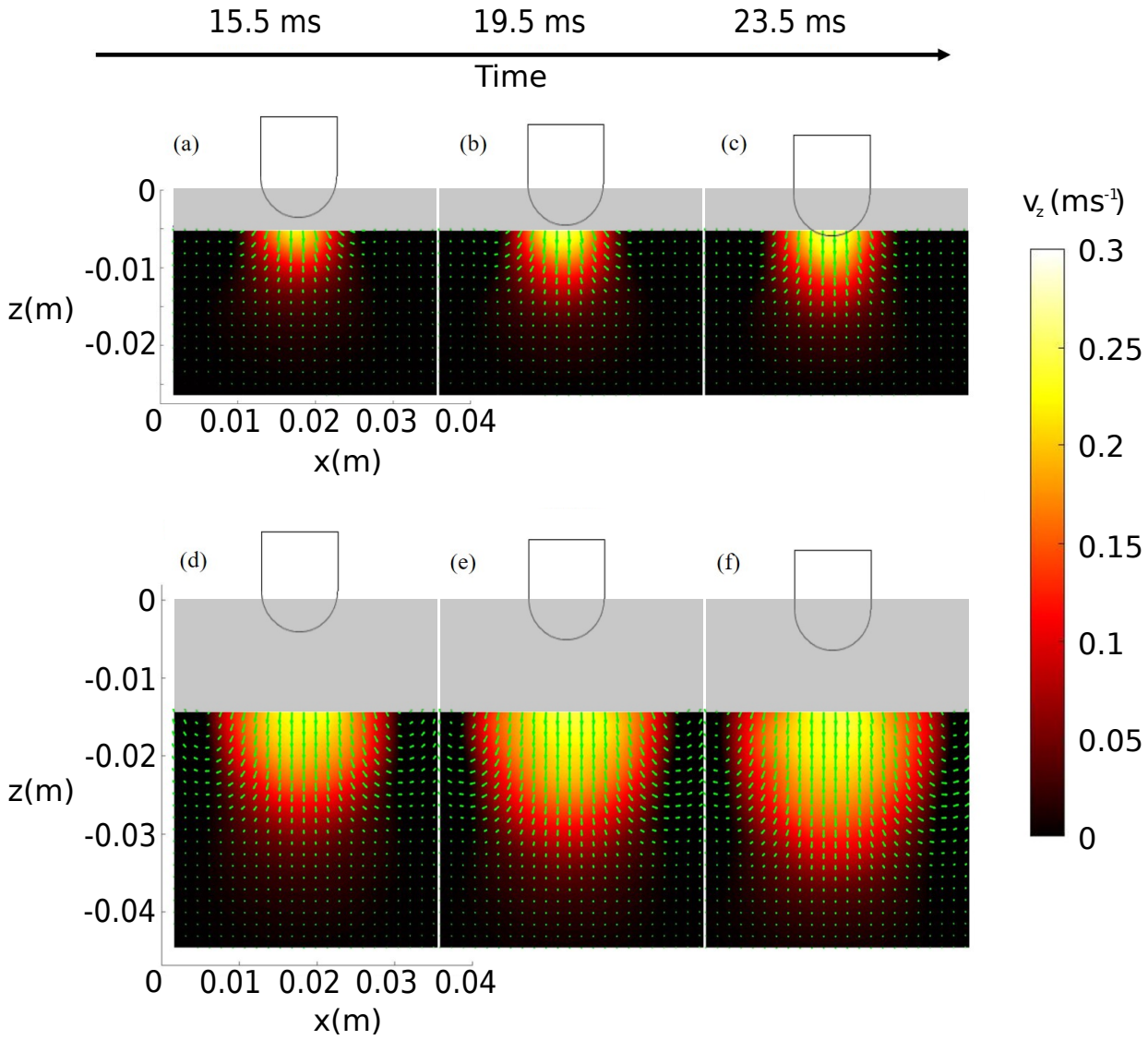

Figure 3.4: Velocity fields and v_z isocontours for impact into Aerosil OX50 suspensions with $\phi_v \approx 0.33$. Shown are snapshots at times $t = 15.5$ ms (a,d), $t = 19.5$ ms (b,e), and $t = 23.5$ ms (c,f) after the impactor reached the suspension surface. Two different solvents are used. The top row (a)-(c) shows results for EG and the bottom row (d)-(f) for PEG-200. Suspension surfaces are at $z = 0$ m and the container bottoms are at $z = -0.03$ m and $z = -0.045$ m for the top and bottom row, respectively. Small green arrows indicate local velocities v_x and v_z. The color mapping tracks v_z, with the upper limit (white) corresponding to the impactor speed (U_p). The actual positions of the impactor in each time frame are outlined. The grey regions indicate the remaining height of the suspension from the field of view of the ultrasound images to the top surface of the suspension.

and subsequent shear-thickening beyond an onset stress (τ_c). From Fig. 3.3a and Fig. 3.3b we see that increasing the packing fraction in PEG-200 enhances both the shear thinning and the degree of thickening, while increasing the packing fraction in EG only enhances the degree of thickening. Comparison between similar packing fractions from Fig. 3.3a and Fig. 3.3b indicates markedly different slopes for the shear thickening as a function of solvent MW. Flow curves that only show mild CST in EG (slope 0.44 on a log-log plot of viscosity as a function of shear stress) now exhibit clear DST in PEG-200 (slope 1). Associated with this change in the thickening behavior in going from EG to PEG-200, we find an increase in the shear thinning, and the minimum in viscosity shifts from a stress of $\tau_c = 11$Pa in EG to a stress of $\tau_c = 100$Pa in PEG-200. To further highlight the role of solvent MW we directly compare suspensions at similar particle concentration $\phi_v \approx 0.33$ but different solvent. This is shown in Fig. 3.3c as a function of stress and in Fig. 3.3d as a function of rate.

3.3.2 Transient Dynamics

To analyze the flow fields of the suspensions under impact, we used a particle imaging velocimetry (PIV) algorithm to extract local velocities $\mathbf{v} = (v_x, v_z)$ from the displacement of tiny air bubbles between successive ultrasound images. Because of the cylindrical symmetry in our system, these two velocity components suffice to reconstruct the entire 3D flow field (10). The impactor hit the suspension surface $z = 0$ mm at $t = 0$ s and continued to move downwards at $U_p = 300\frac{mm}{s}$ into the suspension. Figure. 3.4 shows how the flow fields evolve with time after this impact for suspensions of $\phi_v \approx 0.33$ in PEG-200, one suspended in PEG-200 and the other in EG. The colormap shows the value of v_z, the velocity component in the z direction.

Here we first consider the suspension in EG, shown in the top row of Fig. 3.4. In all three time frames, the flow is highly localized within one centimeter around the impactor tip. This highly dissipative response is what one expects from a viscous liquid. In contrast, we observe

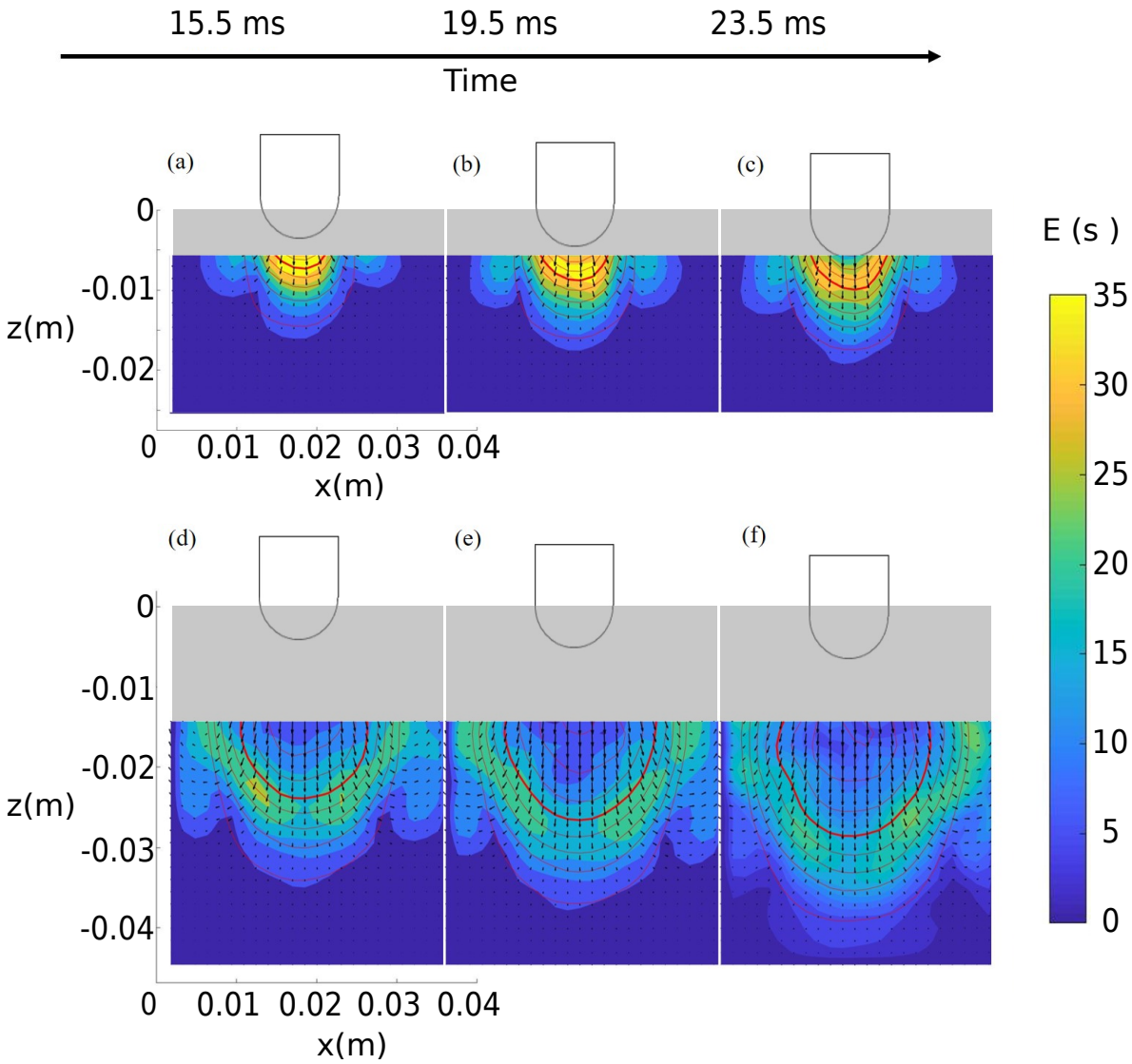

Figure 3.5: Local shear intensity expressed by the strain rate scalar $\dot{E}$ at times $t = 15.5$ms (a, d), $t = 19.5$ms (b, e), and $t = 23.5$ms (c, f) after the impactor reached the surface of the suspension. The suspensions are the same as in Fig. 3.4: Aerosil in EG (top row) and PEG (bottom row). The color map corresponds to the value of $\dot{E}$. Red curves show the isocontours of v_z from $v_z = 0.1U_p$ to $v_z = 0.9U_p$, with increments of $0.1U_p$. The thick curves show $v_z = 0.5U_p$, which we define as the locus of the jamming fronts. The grey region indicates the remaining height of the suspension from the field of view of the ultrasound images to the free top surface.

a dramatically different response in PEG-200, shown in the bottom row of Fig. 3.4. We see a large region, shown as the bright area, which expands into the bulk of the material in both longitudinal and transverse directions. This bright area exhibits a large downward velocity but small internal velocity gradient, as expected for a solid-like state, while the dark region ahead of it is still quiescent. This indicates a large local shear rate at the leading edge of the solid-like region, which is the signature of a shear jamming front, as previously discovered in cornstarch suspensions at much higher packing fraction (10).

To more quantitatively prove that the jamming front forms only in the PEG-200 suspension, we calculate the spatial shear rate distribution. The strain rate tensor in a rotational symmetric system is given by (49)

$$\underline{\underline{\dot{\varepsilon}}} = \begin{bmatrix} \frac{\partial v_r}{\partial r} & 0 & \frac{1}{2}(\frac{\partial v_r}{\partial z} + \frac{\partial v_z}{\partial r}) \\ 0 & \frac{v_r}{r} & 0 \\ \frac{1}{2}(\frac{\partial v_r}{\partial z} + \frac{\partial v_z}{\partial r}) & 0 & \frac{\partial v_z}{\partial z} \end{bmatrix}. \tag{3.1}$$

We can express the effective magnitude of local shear by a strain rate scalar

$$\dot{E} = \sqrt{\left(\lambda_1^2 + \lambda_2^2 + \lambda_3^2\right)/2}, \tag{3.2}$$

where λ_1, λ_2, and λ_3 are the eigenvalues of $\underline{\underline{\dot{\varepsilon}}}$ in Eq. (3.1). $\dot{E}$ for the $\phi_v \approx 0.33$ OX50-EG suspension at three time frames is shown in Fig. 3.5 (a)-(c). We see that the distance between the rod tip and the $v_z = 0.5U_p$ isocontour remains constant during the whole impact process. Also, the region with maximum $\dot{E}$ is concentrated immediately next to the rod. Taken together, this reveals that the OX50-EG suspension under impact does not jam into a solid-like region with a propagating leading edge (jamming front), but remains a viscous fluid.

The bottom row of Fig. 3.5 shows $\dot{E}$ for the same three time frames when the solvent is switched to PEG-200. Behind the shear jamming front, the dark blue region indicates a low

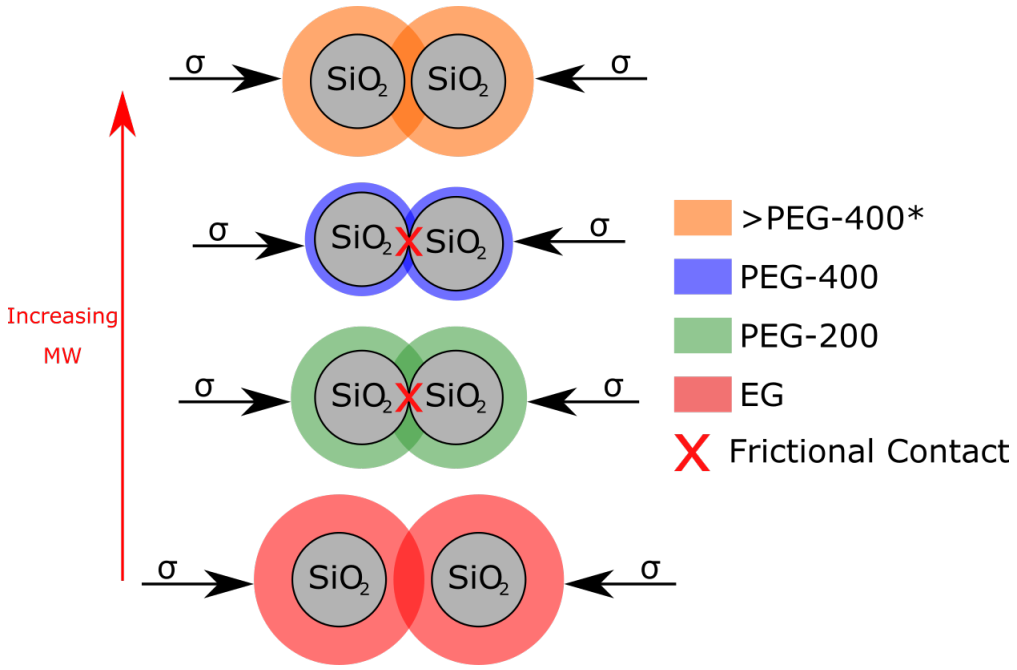

Figure 3.6: Schematic depiction of solvation layers that resist the formation of frictional interparticle contacts and that change as a function of increasing solvent molecular weight. Shaded regions in orange, blue, green, and red surrounding the particles depict the solvation layer of strongly bound solvent molecules. For EG the solvation layer is strong and the applied stress cannot overcome the energetic penalty for desolvation. But in both PEG-200 and PEG-400 the solvation layer is relatively weak, so an applied stress τ can give rise to frictional contacts. *We conjecture that if we could measure fumed silica suspensions in higher MW PEG's (higher MW PEG's are solid at room temperature) that this trend of decreasing solvation layer strength would eventually reverse and the stress required to form frictional contacts would start to increase.

shear rate, which corresponds to a solid-like region continuously propagating and expanding into the suspension. $\dot{E}$ peaks in the shell-like region close to the isocontour $v_z = 0.5U_p$ for all time frames, while it is almost invariant along this shell. This coincides with the rapid decrease in velocity at the boundary between the jamming front and the unjammed, still liquid-like suspension ahead of it.

3.3.3 Discussion

Many studies have demonstrated that the dramatic increases in viscosity associated with DST and the solid-like behavior seen in SJ result from the formation of frictionally-stabilized, percolating contact networks (7; 15; 29; 50; 6; 12; 17). However, these frictional contacts can only form once the applied stress overcomes the repulsive barriers associated with surface solvation (i.e. lubrication breakdown). The data reported here for fumed silica demonstrate that increasing the MW of the suspending solvent elicits DST in PEG-200 at packing fractions that exhibit only CST in EG. Furthermore, in PEG-200 at concentrations far below those required with cornstarch, the suspensions show solid-like, shear jammed behavior under impact, while in EG they behave like viscous fluids. Increasing the MW further by going to PEG-400 only enhances shear thickening. The dramatically different stress responses indicate that even subtle changes in solvent MW affect the ability of the force chain network to resist applied shear.

This effect could be due to either changes in the effective friction coefficient (μ_{eff}) between particle surfaces or changes in the stress-dependent balance of lubricated to frictional contacts. However, as the particle surface chemistry is the same in all suspensions studied here, the friction coefficient between desolvated surfaces is likely identical. This reasoning implies that the solvent MW tunes the repulsive force profile between approaching silica surfaces responsible for resisting frictional interparticle contacts. This scenario, whereby weakening the repulsive barrier between particles leads to more particles interacting frictionally and thus enhanced shear thickening, has recently been suggested to explain similar results in suspensions with polymer additives (51).

The scenario we are proposing, therefore, is that an increase in the solvent MW decreases the strength of the surface solvation layer and enables particles to enter into frictional contact at lower applied stresses (Fig. 6). In other words, the force profile between silica surfaces in PEG-200 is less repulsive than in EG. Thus, a greater applied stress is required to force

particles into frictional contact in EG. Our reasoning is consistent with measurements of the second virial coefficient for dilute samples of 40nm silica dispersed in polyethylene glycol melts (52). Anderson and Zukoski observed a highly repulsive interaction between silica particles in EG, whereas the interparticle potential in PEG-400 and longer PEGs is only slightly more repulsive than their hard-sphere equivalents. While we are unaware of studies in higher MW PEG, atomic force microscopy (AFM) measurements similarly reported a steep and long-ranged repulsive force that extends over 5 nm between silica surfaces in EG (53). These literature precedents coupled with our rheological and impact experiments suggest that the force required to make frictional contacts decreases with increasing MW (Fig. 3.6).

While not the focus of this study, we note that the enhanced shear thinning behavior at low applied stress or shear rate as we move from EG to PEG-400 signals an increase in long-ranged attractive forces between particles (54). As a result of the enhanced shear thinning, also the characteristic stress τ_c associated with the minimum of the viscosity curve $\eta_r(\tau)$ moves to larger values (see Fig. 3c). While this minimum stress is sometimes identified with the onset of shear thickening, i.e., with the critical stress required to push particles into frictional contact, we caution against this interpretation since the true onset stress is likely obscured by the strong shear thinning in all samples, as has been noted in other studies (54; 55).

We now turn our attention to the specific molecular mechanisms that underlie the relative solvent layer strengths. The adhesion energy and resulting conformation of polymer chains at particle surfaces is well known to influence the macroscopic properties of composite materials (56; 57; 58). Polyethylene glycol chains primarily interact with surface silanol (Si-OH) groups through hydrogen bonds with backbone ether (-O-) or terminal hydroxyl (-OH) groups. The hydroxyl end groups have a much larger binding affinity for the silica surface than the ether oxygens (56; 57; 58). As the MW increases, the concentration of hydroxyl end groups decreases and results in a less strongly bound surface solvation layer. Furthermore, increasing

polymer MW results in less dense surface layers by virtue of their less compact conformation at the particle surface (59; 60; 57). The solvation layer in EG is thus denser and also has a larger enthalpic cost for desolvation. Furthermore, solvation of the silica surface by EG facilitates silanol group dissociation (Si-OH $\rightarrow$ Si-O$^-$ + H$^+$) (52). In summary, consistent with arguments by Raghevan, Walls and Khan (44), the increased hydrogen bonding between particle and solvent leads to a stronger, enthalpically stabilized surface solvation layer in EG that stabilizes the dispersed or "lubricated" state. Increasing the MW decreases this barrier and facilitates frictional interparticle interactions at lower applied stresses. To be sure this phenomena is driven mainly by solvation forces we can follow Raghevan, Walls and Khan (44) and estimate the van der Waal's forces between the particles in the three suspending solvents. Using index of refraction values and dielectric constants from the literature (61) we find that the van der Waal's forces for particles in PEG-200 and PEG-400 nearly vanish, while for EG there is a small repulsion that contributes to the particles having the largest barrier to frictional contact in EG.

Our current results and interpretation differ from a number of other studies (41; 40; 42; 43), which concluded that increasing solvent MW suppresses shear thickening due to a more strongly adsorbed surface polymer layer. However, these other studies did not investigate the low MW regime of monomer to oligomer and only investigated polymers with 7 or more repeat units. Surprisingly, even increasing the degree of polymerization of polypropylene glycol (PPG) from n=7 to 17 already shows a (small) decrease in shear thickening (42; 44). In this slightly higher MW regime, a number of studies demonstrated that overall surface coverage increases with MW (57; 62; 63). In other words, the multidentate binding with increasing MW beyond a certain limiting value of n (perhaps around 8-10 in our case) leads to a reduced translational entropy cost for each subsequent binding event and leads to a higher binding coefficient per polymer segment. This entropically bound polymer layer could then lead to a steric barrier that inhibits frictional particle contacts, which could explain the

decreased shear thickening and shift towards higher τ_c with higher MW reported by Shenoy and Wagner (41). Alternatively, as Xu et al. (40) observed no change in τ_c but decreased shear thickening with increasing MW, the bound polymer layer could simply "cap" surface hydroxyl groups and lead to a lower effective interparticle friction coefficient. Thus, beyond a certain characteristic MW the trend can reverse and frictional interactions start to diminish (Fig. 3.6, top row). Where this cross-over takes place is likely to depend on details of the particle surfaces. For example, if the very rough fumed silica agglomerates are replaced by comparatively smooth silica spheres, this cross-over might shift to slightly lower n. Indeed, we find a similar increase in shear thickening strength when switching from EG to PEG-200, but for PEG-400 there is already an indication that the maximum in frictional interaction has been exceeded, as shown in Fig. S3

3.4 Conclusion

The rheological response of shear thickening fluids is a consequence of microscopic interactions. As such, macroscopic changes in the flow profiles are in fact a sensitive reporter of subtle changes in molecular-level interactions. In this study, we investigated the effect of PEG MW on the shear thickening behavior of fumed silica suspensions. By steady-state rheology, we observed that increasing PEG MW led to increased shear thickening. Similarly, by high-speed ultrasound imaging, we observed, for the first time directly, how increasing the MW elicits SJ under impact. We find that the extent of shear thickening and the ability to enter the SJ state are highly dependent on the choice of suspending solvent, which we interpret in light of the stress-dependent balance of lubricated versus frictional contacts. On the basis of prior adsorption and AFM studies we argue that increasing the number of polymer solvent repeat units, n, up to a certain characteristic value weakens the solvation layer surrounding the particles by decreasing the density of more strongly binding -OH end groups. This weakening of the solvation layer lowers the stress required to push particles into

frictional contact which is ultimately responsible for the increase in shear thickening. While PEG solvents with higher MW, i.e., larger n, are solid under our experimental conditions, comparisons with literature precedents of analogous PPG suspensions (44; 42) suggest that even slightly increasing the PEG MW further would actually suppress shear thickening as the system crosses over from a regime where solvation layers are enthalpically-stabilized at low MW ($\leq 400\frac{g}{mole}$ for PEG) to one where they are entropically-bound at higher MW. As a consequence of such crossover, shear thickening may in fact be most pronounced at some intermediate MW. This crossover resolves the apparent contradiction between our current results and previous studies (41; 40; 42) as those studies investigated the higher MW regime where polymers are entropically bound to the particle surface.

Taken together, these findings also open up new opportunities to control both shear thickening and shear jamming in industrial settings, as changing the relative surface affinity of the solvent is much easier than modifying particle properties such as size, shape, or surface chemistry. Our results show that shear jamming during suspension processing can be suppressed (or enhanced) through judicious selection of a solvent that will strongly (or weakly) solvate particle surface chemical functionalities and therefore inhibit (or facilitate) frictional interparticle contacts.

CHAPTER 4

MINIMALLY RIGID CLUSTERS IN DENSE SUSPENSION FLOW

4.1 Introduction

In this Chapter, we explore how transient rigid structures embedded inside of dense suspension flows can contribute to the dissipation of the system. We measure rigidity by importing tools from dry granular materials that were originally used to study jamming in frictional disks to study how the evolution of force chains in dense suspension flows can solidify and yield under imposed stress. Strikingly, we find that system spanning rigid clusters embed themselves into the flow at sufficiently high stresses and packing fractions. Surprisingly, where these rigid clusters begin to span the system do not coincide with bulk rheological signatures, such as DST, although the packing fraction at which rigid clusters span the system and where DST occurs do coincide.

When small particles are suspended in a liquid and the particle packing fraction ϕ is close to, but below, the packing fraction ϕ_J^μ for jamming, the viscosity can increase orders of magnitude with increasing shearing intensity through a process called shear thickening (64; 65). Current models of strong shear thickening in dense suspensions are based on mean-field ideas, whereby stress τ in excess of some characteristic value τ_0 punctures the particle-particle lubrication by the liquid and activates frictional contact with friction coefficient μ (66; 24; 67; 68; 69; 70; 65; 71). Since the viscosity η diverges as a power law with distance $|\phi_J^\mu - \phi|$ from the jamming point ϕ_J^μ and since ϕ_J^μ for finite μ is smaller than for $\mu = 0$, this

. The research described in this chapter has been published in: van der Naald, A., Singh, T., Eid, K., Tang, de Pablo, J., and Jaeger, H. M. Minimally Rigid Clusters in Dense Suspension Flow *Nature Physics*, Accepted

leads to potentially very large viscosity increases at fixed ϕ.

Mean-field modeling expresses the crossover from lubricated to frictional behavior in terms of the fraction of local frictional contacts that have been activated (72; 24; 73; 69; 71). While successful in predicting the steady-state, strain-averaged flow behavior of suspensions as a function of packing fraction and stress (67; 73; 69; 74), this approach is agnostic of the structural consequences of proliferating frictional contacts, such as the emergence of a meso-scale contact network and its properties. In particular, the degree to which this network of frictional contacts is mechanically stable and can resist deformation has so far not been considered in its effect on viscosity. To address this we here use ideas from rigidity theory.

Rigidity theory predicts the mechanical properties of materials by comparing the number of local constraints to the number of global degrees of freedom (75; 76; 77). If the number of local constraints exceeds or is equal to the number of global degrees of freedom, then the system is mechanically rigid (75; 76). This counting argument was originally formulated by Maxwell to assess the rigidity of mechanical trusses (75), and it has since been used to describe rigidity transitions in granular materials, structural glasses, proteins, and models of cells (78; 79; 76; 80; 81; 82; 83; 84; 85; 86; 87; 88).

In these systems, atoms, molecules, or particles form the nodes of a network, while interactions between these entities become bonds that connect the nodes and provide constraints to relative node movement, in analogy to the beams in Maxwell's trusses. For example, constraints in dry granular systems arise from contacts between neighboring particles (89; 90; 78; 79; 91; 92) while constraints in molecular glasses arise from chemical bonds between adjacent molecules (76; 84; 80). Once interparticle interactions have been mapped to interparticle constraints, constraint counting can then be performed using various methods, including the widely-used algorithm called the pebble game (93; 94; 79; 78). This algorithm decomposes the network into rigid and floppy subsections by counting constraints for each local cluster of nodes, with bulk rigidity corresponding to the limit where the rigid clusters

link up and percolate across the whole network.

Here we apply constraint counting in a new context. Rather than testing the mechanical rigidity of a static network, we analyze snapshots from simulations of the continually evolving network of frictional contacts among particles in a dense suspension under shear. Our goal is to extract mesoscale information about the occurrence of transiently rigid clusters within this frictional contact network and correlate this to the degree of global resistance to flow, as measured by the suspension viscosity.

4.2 Results and Discussion

Analyzing the frictional forces with the pebble game we convert them to interparticle constraints, allowing us to extract from the networks the subset of mechanically rigid particle clusters. We are principally concerned with the rigidity of the frictional force network as the frictional forces have been implicated as the primary forces responsible for DST as well as SJ (65; 3; 95). In the appendix C we investigate how our results change when we incorporate also the repulsive and hydrodynamic forces into the pebble game.

Since the pebble game algorithm is generally limited to two-dimensional (2D) networks (an exception is the application to the special case of protein flexibility (96)), we perform our simulations in 2D as well. Prior work has shown that flow curves simulated for dense suspensions in 2D can reproduce 3D results semi-quantitatively if the volume fraction ϕ is translated appropriately (97; 98).

We find the emergence of extended, rigid sub-structures within the network to be a function of stress, from states with no or only small, localized rigid clusters to states with a single system-spanning rigid cluster. Note that when we label clusters here for brevity as “rigid" this should be understood as “minimally rigid." We make this distinction with prior work (79; 78) on dry granular systems to emphasize that our rigidity metric assesses the mechanical stability of only the sub-network of frictional contacts and is ignorant of friction-

less contacts and hydrodynamic contacts, which ultimately destabilize clusters the algorithm identified as mechanically rigid and force them to evolve into different configurations, thus enabling viscous flow. Analyzing the strain evolution of the extended rigid structures in the large stress limit reveals that for low volume fractions they are fleeting, appearing and immediately dissolving into smaller clusters. However, for higher packing fractions we find large stresses to generate a continuous sequence of system-spanning rigid clusters that reconfigure from one imposed strain step to the next, thereby driving the largest viscosity increases.

Our simulations include hydrodynamic lubrication interactions, purely repulsive contact forces, as well as friction. Unless indicated the data shown are for $N = 2000$ particles (see appendix C for more detail and larger system sizes). Forces on the particles obey the overdamped equation of motion $F_C^N + F_C^T + F_H = 0$ where F_C^N is the purely repulsive normal contact force, F_C^T is tangential Coulombic friction contact force, and F_H is the hydrodynamic lubrication force. The repulsive contact force has an associated stress scale τ_0, which controls the stress required to make frictional contact. In the simulations discussed here, the Coulombic friction force constrains only sliding motion and the friction coefficient is set to $\mu = 1$ (see Methods for details and appendix C for data using other friction coefficients). This simulation scheme has been used extensively in recent years as it is a simple method that can recreate the experimentally measured features of shear thickening suspensions (99; 66; 72; 73; 69; 100; 70; 71).

Using stress-controlled conditions, we simulate different packing fractions from $\phi = 0.766$ to 0.79 over a range of stresses $\frac{\tau}{\tau_0} \in [10^{-1}, 10^2]$.

4.2.1 Decomposing Frictional Force Chains Into Rigid Clusters

Figure 4.1a shows a typical force network resulting from the simulations. Line segments that connect neighboring particle centers are color-coded according to the type of force they represent and form bonds in the associated force network, with the magnitude of the force

represented by the width of the line.

We decompose the network of frictional contacts, shown in red in Fig. 4.1a, into subnetworks of rigid clusters. To do this, we apply a particular version of the pebble game, the so-called (3,3) variant, which was originally developed for dry granular systems with friction (79; 78). This algorithm assigns the local constraints on each particle by determining whether the force at a given contact is below or at the Coulomb threshold for sliding, which decides whether that contact constrains two or one degrees of freedom, respectively. The result for the network in Fig. 4.1a is shown in Fig. 4.1b, where orange bonds are below the Coulomb threshold and black bonds are at the threshold. Once the local constraints on each particle have been established, the (3,3) pebble game returns the minimally rigid cluster decomposition shown in Fig. 4.1c.

(Additional information on the simulation method as well as the pebble game algorithm can be found in the Methods section.) As we see from comparing Figs. 4.1a and c, a dense network of frictional forces, even if highly coordinated and system-spanning, does not necessarily imply the presence of extended minimally rigid clusters.

4.2.2 Emergence of System Spanning Clusters

We now sweep through a range of packing fractions ϕ just below $\phi_J^{\mu=1}$ to generate the family of steady-state flow curves shown in Fig. 4.2a, where we plot the effective suspension viscosity $\eta_r = \eta_0^{-1}\tau/\dot{\gamma}$, normalized by the viscosity η_0 of the suspending liquid, as a function of normalized shear rate $\dot{\gamma}/\dot{\gamma}_0$. Here $\dot{\gamma}_0 = \tau_0/\eta_0$. Figure 4.2a shows the typical shear thickening behavior of dense suspensions, where for each packing fraction the viscosity transitions, as a function of shear intensity, between a low and high viscosity plateau. As ϕ increases, this transition steepens from continuous shear thickening, where the maximum slope of $\eta(\dot{\gamma})$ is positive and finite, to discontinuous thickening (DST), where this slope diverges (at $\phi_{DST} \simeq 0.775$). For purely stress-controlled shearing conditions, as here, the flow curves

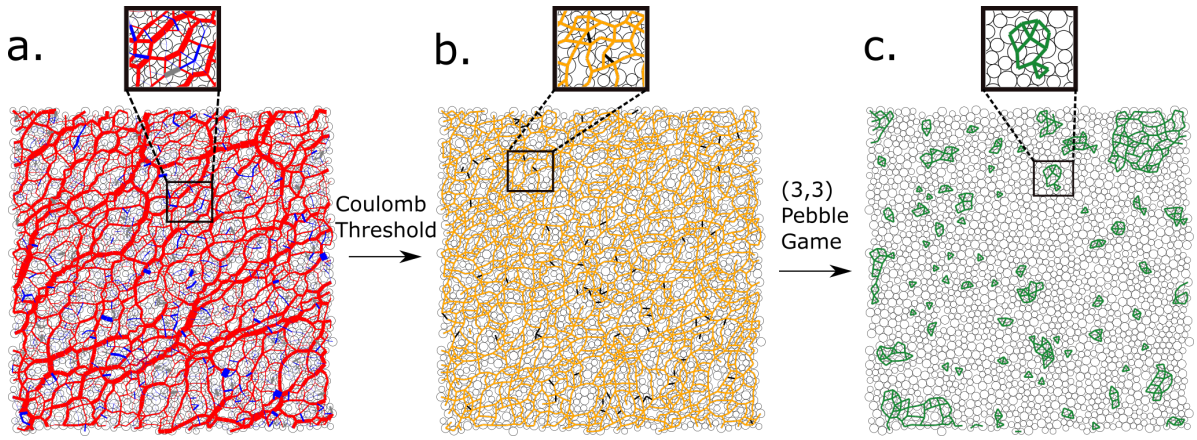

Figure 4.1: **Decomposition of the frictional contact network into rigid clusters.** (a) Simulation snapshot with hydrodynamic forces shown in blue, repulsive forces in grey, and frictional forces in red. Force magnitudes are given by the widths of the line segments, but have been rescaled between different force types so that lines for all types are visible. (b) The contact friction subnetwork, shown by the red lines in panel (a), has been decomposed into contacts that are below the Coulomb threshold (yellow) and contacts at the Coulomb threshold (black). (c) Further decomposition of the network shown in (b) into minimally rigid clusters (green) as a result of applying the (3,3) pebble game algorithm. All simulations use periodic boundary conditions.

develop an S-shape once $\phi > \phi_{DST}$, but in typical experiments, this is an unstable region and the flow curves still jump discontinuously between the low and high viscosity branches.

To visualize at the particle level how the rigid clusters emerge and percolate across the system, we show in Fig. 4.2b-d representative snapshots of the frictional forces (top panel) and their corresponding rigid cluster decomposition (bottom panel) for $\phi = 0.78$, i.e. just above the DST onset. Since frictional interactions are activated by stress, we pick three representative stress levels (in Fig. 4.2a indicated by the red boxes). For the lowest stress $\frac{\tau}{\tau_0} = 1$, frictional contacts only form short, chain-like structures and we find no rigid clusters. At higher stresses, the suspension is being driven sufficiently strongly to form fully percolating frictional contact networks. Nevertheless, the rigid cluster decomposition can show dramatic differences. For $\frac{\tau}{\tau_0} = 10$ the rigid clusters are mostly small and disparate, while at $\frac{\tau}{\tau_0} = 100$ there is a single system-spanning cluster.

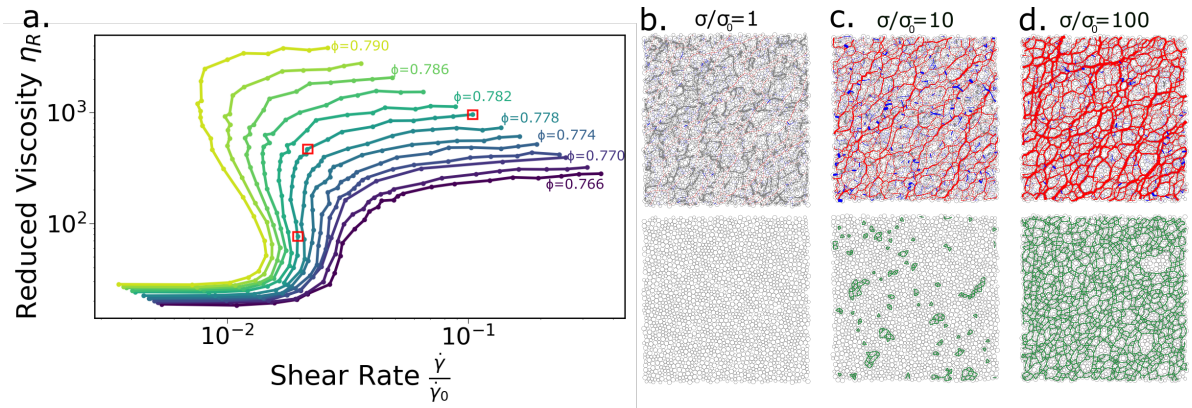

Figure 4.2: **Rheology, frictional contact force networks, and rigidity.** (a) Relative viscosity η_r as a function of shear rate $\dot{\gamma}$ for different packing fractions ϕ. With increasing ϕ the onset of discontinuous shear thickening (DST) corresponds to the first trace that exhibits a vertical jump between the low and high viscosity plateaus. In the 2D suspensions simulated here this occurs at $\phi_{DST} \simeq 0.775$. (b-d) Force networks (top) and associated minimally rigid clusters (bottom) at three stress levels for $\phi = 0.780$: $\frac{\tau}{\tau_0} = 1$ (b), 10 (c), and 100 (d); the corresponding viscosities are indicated by the red boxes in panel (a). The color coding for the different forces is the same as in Fig. 4.1.

4.2.3 Rigid Cluster State Transitions

To track this quantitatively, we define the size S of a given, minimally rigid cluster as the number of participating particles. Taking snapshots as in Figs. 4.3b-d at strain increments $\delta\gamma = 0.1$ over large intervals in the steady-state, we compile rigid cluster size distributions $P(S)$. As we are interested in networks that potentially generate the largest resistance to shear and thus the highest viscosity, we focus in the following on the distribution of the largest rigid clusters, $P(S^{\max})$. Figures 4.3a-c show representative examples of $P(S^{\max})$ for the same three stress values as in Figs. 4.2b-d at packing fractions $\phi = 0.77$, 078, and 0.79. We plot $P(S^{\max})$ for $\phi = 0.776$ and $\phi = 0.774$ (just above and below the onset of DST) in the SI. The associated behavior of $S^{\max}$ as a function of strain γ is shown in the insets.

For all packing fractions $\frac{\tau}{\tau_0} = 5$ produces small clusters and thus small $S^{\max}$ values. At $\phi = 0.77$, we find that clusters involving more than 10 percent of the particles appear only at the largest stress and then only fleetingly (Fig. 4.3a). Increasing the packing fraction to

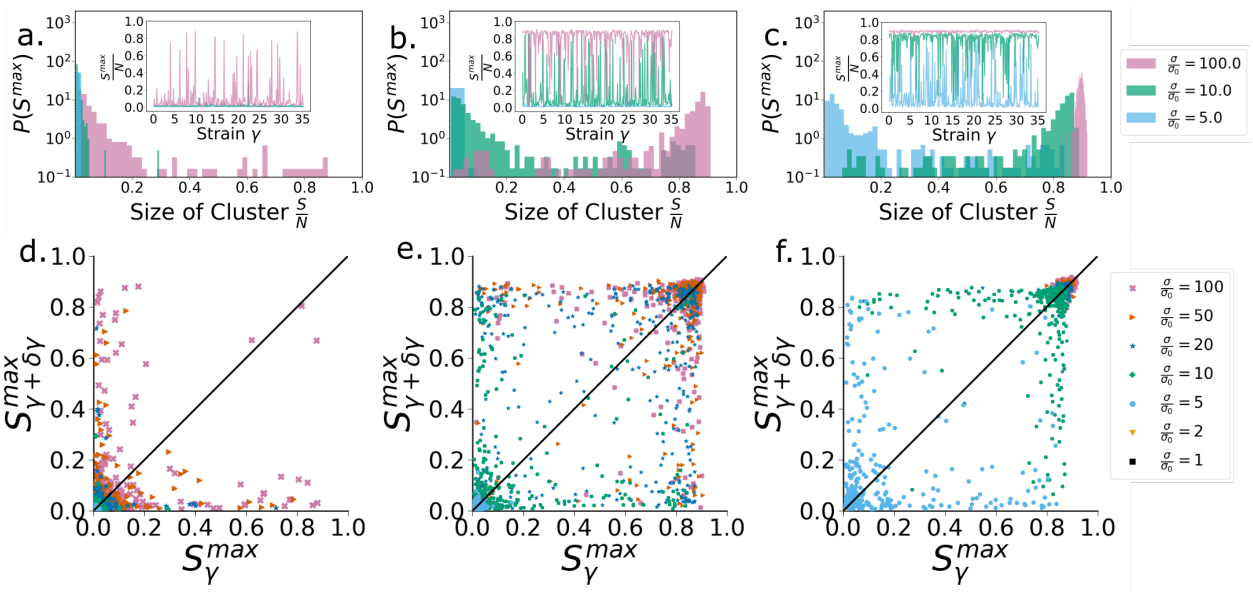

Figure 4.3: **Steady-state dynamics of the largest rigid clusters.** (a-c): Size distributions $P(S^{\max})$ for the largest rigid clusters within the network of frictional contacts. Data shown are for three stresses each at packing fractions $\phi = 0.77$, $\phi = 0.78$, and $\phi = 0.79$. Cluster size S is the number of participating particles. Insets: Evolution of maximum rigid cluster size $S^{\max}$ as a function of strain γ for the same three stresses. (d-f): Return maps at various stresses (see legend to the right of panel (f)) for volume fractions $\phi = 0.77$, $\phi = 0.78$, and $\phi = 0.79$. The maps show how the largest cluster at strain γ, which has size $S^{\max}(\gamma)$, evolves to a new size, $S^{\max}(\gamma + \delta\gamma)$, one strain increment $\delta\gamma$ later. In our simulations $\delta\gamma = 0.1$.

$\phi = 0.78$ bimodal distributions emerge (Fig. 4.3b), where large clusters form often but then collapse (for $\frac{\tau}{\tau_0} = 10$) or where large clusters are the typical state and where they quickly reconstitute after a collapse (for $\frac{\tau}{\tau_0} = 100$). As the packing fraction is increased further to $\phi = 0.79$ (Fig. 4.3c) system-spanning rigid clusters become much more prevalent even at $\frac{\tau}{\tau_0} = 10$, and the suspension evolves from one such cluster to the next, only temporarily jumping to smaller cluster sizes. The intermittent dynamics of these clusters switching between essentially two states is reminiscent of fluctuations seen in boundary stress measurements by Rathee *et al.*, who find intermittent bursts in regions with high stress (23; 101). A movie of the evolution of interparticle forces and rigid clusters with packing fraction and strain for the systems shown in Fig. 4.3 a-c is available in the SI.

A convenient way to analyze the cluster size fluctuations and how this behavior evolves with stress and packing fraction is via return maps of the maximum cluster size, $S^{\max}$. This is done in Fig. 4.3d-f. Each point on these return maps refers to a consecutive pair of simulation snapshots, where the x-coordinate corresponds to the largest rigid cluster at strain step $S^{\max}(\gamma)$ and the y-coordinate to the largest rigid cluster at the next strain step $S^{\max}(\gamma+\delta\gamma)$. For example, points near the lower left corner refer to transitions from a state having small clusters to another state with small clusters, while points in the upper right refer to transitions from one large, system-spanning cluster to the next.

For $\phi = 0.77$ (Fig. 4.3d) almost all points cluster around the bottom left corner, indicating that large clusters rarely form and when they do they fail to persist for more than a single strain step. For $\phi = 0.78$ (Fig. 4.3e) the majority of points reside near the bottom left or top right corners. This reflects the bimodal character of the cluster distribution and the abrupt onset of system-spanning minimally rigid clusters. Occasionally some points populate the top left and bottom right corners corresponding to the formation and destruction of system-spanning minimally rigid clusters, respectively. However, the majority of points with $\frac{\tau}{\tau_0} \geq 20$ populate the area near the top right, indicating long sequences where one system-spanning minimally rigid cluster under strain reconfigures into another cluster of the same type. As the packing fraction reaches $\phi = 0.79$, we see that almost all points reside in the bottom left or top right corner (Fig. 4.3f). Interestingly, there are very few points in the middle of the return maps, indicating that intermediate sized clusters are rare and unstable when they form. We find that the return maps are insensitive to the strain step if we instead plot $S^{max}_{\gamma+2\delta\gamma}$, $S^{max}_{\gamma+3\delta\gamma}$, or $S^{max}_{\gamma+4\delta\gamma}$ on the y-axis, as shown in the SI.

4.2.4 Dense Suspension Phase Diagrams and Rigid Clusters

Given the asymmetric and often bimodal character of the distributions $P(S^{\max})$, we characterize them by their median. Figure 4.4a shows that sizeable median values, corresponding

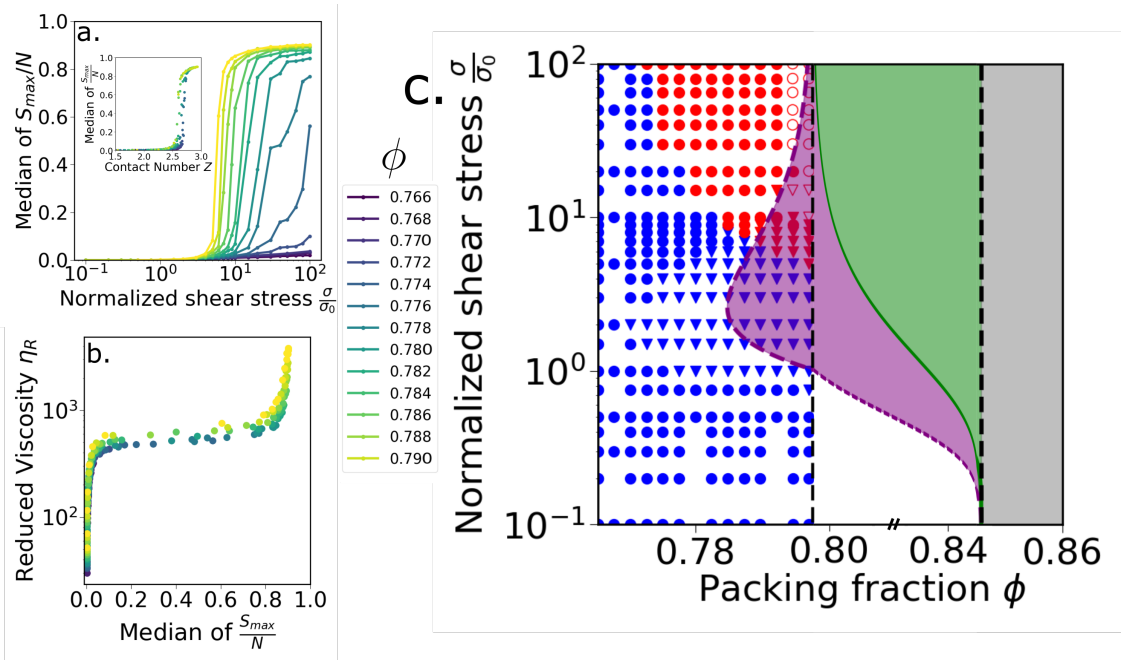

Figure 4.4: **System-spanning rigid cluster statistics define new regime in the suspension state diagram**. (a) Evolution of the rigid cluster statistics, taken here as the median of $S^{\max}/N$ as a function of normalized shear stress τ/τ_0. Data for different packing fractions ϕ are delineated by color. The onset of system-spanning rigid clusters occurs at $\phi_{rig} \simeq 0.775$. Inset: Median of $S^{\max}$ as function of average coordination number Z_{fric} of the frictional contact network.(b) Normalized viscosity as function of the median of $S^{\max}/N$ for different packing fractions ϕ, with color coding given by the legend. The same color coding applies to the data in panel (a). (c) State diagram delineating flow behaviors of dense suspensions as a function of stress and packing fraction. Blue data points: states without a system-spanning rigid cluster in 75% of simulation snapshots. Red data points: states with a system-spanning rigid cluster in 75% of snapshots. Blue or red triangles indicate where discontinuous shear thickening (DST) is observed in the simulations, while circles indicate that DST is not observed. The state diagram also shows the different flow regimes based on mean-field theory: shear jammed (green), DST (purple), and isotropically jammed (gray). The boundaries of the purple and green regions were generated by fitting flow curves, as in Fig. 4.2a, near the onset of DST to the Wyart-Cates (WC) mean-field model (Ref.4). Note that the simulation data (triangles) show the onset of DST at a packing fraction slightly lower (by about 0.01) than predicted by the WC model.

to rigid clusters that involve the majority of all particles, occur only once ϕ approaches ϕ_{DST}. In fact, the transition in the high-stress limit from only small, isolated rigid clusters (median $[P(S^{\max})] < 0.1N$) to high likelihood for observing a fully system-spanning rigid cluster proceeds abruptly in the vicinity of ϕ_{DST}. Associated with this increase is a subtle enhancement of the local connectivity of the nodes in the network of frictional contacts, seen in the average coordination number Z_{fric} (Fig. 4.4a inset): system-spanning rigid cluster require $Z_{fric} > 2.7$. These data also make clear that the frictional contact network becomes (momentarily) rigid well before the suspension jams and the flow arrests completely at $Z = Z_{iso} = 3$. Note that a related observation about onset of rigidity not coinciding with isostaticity has been made in dry granular materials (78).

A second remarkable feature of the data in Fig. 4.4a is the abrupt increase in the size of rigid clusters with stress, especially for the larger ϕ values. To confirm that this behavior is not a finite-size effect, we carried out additional simulations for systems with $N = 5000$ and $N = 10000$ and found the transition to be just as abrupt (see Fig. S1). This abrupt transition is strikingly different from the smooth change of other network measures across the shear thickening transition, for example, measures based on persistence homology or force tile analysis (97; 102; 103; 104). Instead, it is reminiscent of the sharp transitions seen in dry granular systems where system spanning clusters appear as a function of contact number Z (78; 79**?**). In those works the transition corresponds to the jamming transition where the system solidifies and has been measured to occur for $Z_{crit} \approx 2.4$ in experiment(78) and $Z_{crit} \approx 2.9$ in simulation (79). Our finding of $Z_{crit} \approx 2.7$ is within this range, but further investigation characterizing the distribution of clusters is needed to determine if the transition we find lies in the newly discovered frictional universality class for frictional rigidity transitions (**?**), in particular regarding the location and sharpness of the transition as friction is changed. The nature of the transition might be different as all suspensions studied here are continually flowing and not static.

Plotting the viscosity as a function of median $S^{\max}/N$ gives further insight (Fig. 4.4b). We find that the increase of the normalized viscosity during shear thickening proceeds in two steps: over the first decade and a half the dominant contribution is from the local frictional interactions in contact force networks that are not mechanically rigid, until at higher packing fractions and stresses these frictional contacts begin to act cooperatively and form extended, minimally rigid clusters that are responsible for the last decade of viscosity increase. Put another way, for the most highly dissipative states it is not sufficient to have a fully saturated and percolated networks of frictional contacts; additionally these networks need to be mechanically rigid.

Figures 4.4a and b show that a minimum packing fraction is required for system-spanning rigid clusters to emerge. Using as our criterion that system-spanning rigid clusters appear in 75% of all analyzed strain increments, we find that this minimum packing fraction, ϕ_{rig}, appears essentially indistinguishable from the minimum packing fraction required for observing DST, $\phi_{DST} \approx 0.775$ (different criteria do not change ϕ_{rig} by more than 0.005; see the SI).

This finding is particularly interesting if we overlay the probability of finding minimal rigid clusters onto a mean-field state diagram for dense suspensions (24; 3; 69; 65), which delineates the onset of DST (purple region) and shear-jamming (green region) as a function of packing fraction and shear stress. This is done in Fig. 4.4c, where the regime of system-spanning rigid clusters is indicated by the red data points (note that in this work we restrict ourselves to $\phi < \phi_J^{\mu=1}$, i.e., to suspensions that always flow and do not jam at the largest stresses). Red hollow data symbols in Fig. 4.4c correspond to simulations where fewer snapshots to average over were available, given that simulations in the regime very close to shear jamming are computationally expensive. We note a slight discrepancy between the mean-field model prediction for the onset of DST ($\phi \approx 0.784$) and what is obtained from simulation ($\phi \approx 0.775$).

As indicated by the only partial overlap between the red data points and the DST regime

in Fig. 4.4c, frictional network rigidity clearly does not equate with with DST, despite the onsets nearly coinciding in terms of packing fraction, i.e., $\phi_{rig} \simeq \phi_{DST}$. This shows that DST flows cannot be understood as simply a strain- (or time-)average over a sequence of jamming/unjamming events, since the granular backbone attains rigidity only at higher stresses. As we see from Fig. 4.4c, rigidity starts to occur within the DST regime only when ϕ gets close to ϕ_J^μ and then only for stress levels well beyond the stress range over which DST occurs. At lower packing fractions where ϕ gets closer to ϕ_{DST}, extended rigid network structures that could temporarily jam do not even appear within the stress range where DST occurs and only emerge in the upper (Newtonian) viscosity plateau, well above the DST "nose."

4.3 Conclusion

From this analysis a new flow regime emerges within the $\phi - \tau$ state diagram that starts at, or very close to, the packing fraction where DST is first observed, but is distinct from the DST regime in that it marks, as a function of stress, when system-spanning rigid clusters start to drive the dissipation and enable very high viscosities $\eta_r > 500 - 1000$ (Fig. 4.4b). Since this occurs via continual breakup and reconfiguration of extended rigid clusters (Fig. 4.3) we interpret the new regime, rather than DST, as a true precursor of flow arrest through jamming.

Our results demonstrate that analyzing the rigidity of the frictional contact networks in dense suspensions provides new information that goes beyond what can be extracted from measuring the local connectivity or the percolation of frictional forces. An interesting line of future work will be investigating how our rigidity-based analysis compares to recent connectivity-based network measures such as the k-neighbor particle analysis reported by Goyal et al. (105). As such the deconstruction of these networks into mechanically rigid and non-rigid components might enable theoretical advances to go beyond current mean-field

models (24; 72; 73; 69). We envision that this approach can be powerful also when applied to a wide range of other flowing amorphous systems, including emulsions, gels, and foams.

4.4 Methods

4.4.1 Simulation Scheme

In order to simulate dense suspensions near their frictional jamming point ϕ_J^μ we use the well established simulation scheme "Lubricated flow DEM (LF DEM)" (106). The simulation scheme marries lubricated interactions with a discrete element method (DEM) contact model (72) and has been succesful reproducing many experimental features observed in experiments (107; 69; 100; 70; 71). We simulate a two dimensional monolayer of non-Brownian spherical particles immersed in a Newtonian fluid. The simulation scheme presented here is, in principle, similar to Seto et al. (66), where a fixed shear rate was applied to the system. However, since the interest here is to analyze dense suspensions close to their jamming limit ϕ_J^μ, we simulate dense suspensions under constant shear stress, following Mari et al. (107). Our procedure amounts to implementing pairwise hydrodynamic forces between particles within a range of $0.2a$ where a is the radius of the smaller particles. This follows previous studies that considered simple shear using only lubrication interactions while neglecting long-range hydrodynamics for dense suspensions. The gain here is twofold: first, excellent agreement with experimental data sets indicates that considering only lubrication is sufficient to capture the essential particle dynamics in these conditions (107; 71); second, considering only lubrication speeds up the simulations since including long-range hydrodynamics makes the problem extremely difficult computationally in crowded conditions (108; 65). We use Lees-Edwards periodic boundary conditions and impose a shear stress on the system τ (107; 69). In strictly monodisperse 2D simulations of discs it is difficult to avoid crystallisation regardless of interaction potential, packing preparation, or shear protocol (109; 110**? ?**

). To avoid ordering in simulations of disks it is common to use a mixture of particles with a size ratio of 1:1.4 (72; 95; 111; 109; 110**? ?**), and we follow that convention here.

We work in the inertialess limit and consider contact ($\vec{F}_{\mathrm{C}}$) and hydrodynamic ($\vec{F}_{\mathrm{H}}$) forces between particles. Thus, the motion of each particle is obtained by solving the following force balance equations:

$$\vec{0} = \vec{F}_{\mathrm{H}}(\vec{X}, \vec{U}) + \vec{F}_{\mathrm{C}}(\vec{X}) \ , \tag{4.1}$$

where $\vec{X}$ and $\vec{U}$ denote the positions and velocities/angular velocities of all particles, respectively. The equation of motion is coupled with the constraint of the imposed flow at constant shear stress τ. At a given time, the stress in the suspension is given by the summation of hydrodynamic τ_{H} and contact τ_{C} contributions:

$$\tau = \tau_{xy} = \dot{\gamma}\eta_0\left(1 + \frac{5}{2}\phi\right) + \dot{\gamma}\eta_{\mathrm{H}} + \tau_{\mathrm{C}} \ , \tag{4.2}$$

where η_0 is the suspending fluid viscosity, $\eta_{\mathrm{H}} = V^{-1}\left\{(R_{\mathrm{SE}} - R_{\mathrm{SU}} \cdot R_{\mathrm{FU}}^{-1} \cdot R_{\mathrm{FE}}) : \hat{E^{\infty}}\right\}_{xy}$, $\tau_{\mathrm{C}} = V^{-1}\left\{XF_C - R_{\mathrm{SU}} \cdot R_{\mathrm{FU}}^{-1} \cdot F_C\right\}_{xy}$, with R_{SU} and R_{SE} being the resistance matrices to calculate the lubrication stress based on particle velocity and deformation resistance (72; 112), E^{∞} is the the rate-of-strain tensor, : stands for a double dot product, $\{\}_{xy}$ denotes taking the xy entry of the resulting matrix inside the brackets, and V is the volume of simulation box. R_{FU} and R_{FE} are position dependent resistance matrices contain the "squeeze," "shear," and "pump" modes of pairwise lubrication along with one-body Stokes drag. Imposing this shear stress leads to a time-dependent shear rate $\dot{\gamma}(t)$ which we then use to calculate the viscosity. Rheology data presented here are averages of $\eta_r = \tau/\dot{\gamma}/\eta_0$ over a time window equivalent to 30 strain units.

Finally, to introduce the rate dependence we employ a critical load model (CLM) (95; 72; 73). The contact force between particles i and j is purely in the normal direction until the normal force exceeds some critical load F_{CL} and then Coulombic sliding friction is turned

on. Thus the friction law reads:

$$|\vec{F}^{i,j}_{C,tan}| \leq \left\{ \begin{array}{ll} \mu(|\vec{F}^{i,j}_{C,norm}| - F_{CL}) & : |\vec{F}^{i,j}_{C,norm}| \geq F_{CL} \\ 0 & : \text{otherwise} \end{array} \right\} \tag{4.3}$$

where we use a coefficient of sliding friction $\mu = 1$ for most of the work here (for different values of μ see the SI; we do not consider rolling friction separately). The force scale F_{CL} sets a stress scale $\tau_0 = F_{CL}/6\pi a^2$, such that for $\tau \ll \tau_0$ the contacts are frictionless, whereas for $\tau \gg \tau_0$ contact friction dominates. We non-dimensionalize the shear rate $\dot{\gamma}/\dot{\gamma}_0$ using $\dot{\gamma}_0 = F_{CL}/6\pi\eta_0 a^2$ with η_0 being the viscosity of the background solvent. For more information about the CLM, the hydrodynamic forces, contact forces, and the simulation scheme see (95; 72; 69).

4.4.2 Pebble Game Algorithm

To find rigid clusters in our frictional contact networks we use the pebble game algorithm. This algorithm finds rigid clusters by comparing the local constraints in a network to the global degrees of freedom to determine if any portions of the network are fully constrained, and therefore rigid. To apply this algorithm we map particles to nodes in the network and frictional contacts to bonds. In general, there exists a (k,l) pebble game where k is the number of degrees of freedom for each particle and l is the number of total global degrees of freedom for the system (94). In this work we study two dimensional frictional contact networks with three degrees of freedom per particle and three global degrees of freedom, thus we restrict ourselves mainly to the (3,3) pebble game, but find that our results are nearly identical if we instead use the (3,2) pebble game, as shown in the SI. The (3,3) game was originally used in simulations of two-dimensional packings of dry frictional particles by Henkes et al. (79), while the (3,2) game has been used in frictionless packings (113). In order to construct the constraint network for the (3,3) pebble game we consider how

each contact constrains particle motion. We use Coulombic friction so there are two types of constraints between frictional particles, sliding and non-sliding contacts. For contacting particles below the Coulomb threshold ($F_{C,tan} < \mu F_N$) motion is constrained in both the normal and tangential directions, giving two constraints to particle motion. Particles at the Coulomb the threshold ($F_{C,tan} = \mu F_N$) have met the threshold to slide and only constrain the normal direction of motion, giving a single constraint to particle motion. After mapping the contact network to a constraint network we run the (3,3) pebble game algorithm. Results presented in the main text include exclusively frictional forces in the constraint network, as they play a predominant role in stabilizing the force chains leading to rigidity in the system. However, in the SI we include multiple attempts to incorporate hydrodynamic lubrication forces and purely repulsive forces into the (3,3) pebble game to see how those alterations to the pebble game impact the cluster size statistics. For implementation of the (3,3) pebble game see (87; 79). In our simulations we perform the (3,3) pebble game for simulation snapshots separated by a strain increment $\delta\gamma = 0.1$. We chose this strain step such that each simulation snapshot would sample a different ensemble of clusters so that we can adequately correlate cluster size to strain-averaged, steady-state quantities like viscosity. The modeling based on the pebble game algorithm comes with some limitations. As mentioned in the introduction, the currently available algorithm extracts rigid clusters accurately for 2D but not for 3D networks. This limitation in 3D comes from the occurrence of network structures that the pebble game misidentifies as rigid (**?**). These misidentifications also happen in 2D but are rare in disordered networks such as the ones we investigated in this work (93; 78)

CHAPTER 5

RHEOLOGY OF COMMON STARCH SUSPENSIONS

5.1 Introduction

In this chapter we explore the rheology of suspensions of common household starches such as corn, potato, and wheat starch. Cornstarch suspension rheology is commonly measured in dense suspension studies and serves as a prototypical shear thickening and shear jamming suspension both for research but also for physics demonstrations (9; 114; 1). Despite cornstarch suspensions common use in research and outreach, other starch suspensions have not been studied.

Dense suspension flows are ubiquitous across many length scales from geophysical debris flows to colloidial flows relevant in biological processes and 3D printing. One rheological behavior that is commonly measured in these flows is shear thickening, where the viscosity of the suspension increases with applied stress. Even more striking, is when these flows arrest and the suspension solidifies in a process called shear jamming (SJ), a property that is often exploited in physics demonstrations. Both shear thickening and shear jamming have been the subject of intense study over the last decade, and in that time a consensus has emerged that both of these properties arise suspended particles interacting frictionally. This insight has led to designer suspensions where particles and solvents are modified to allow for either a greater number of frictional contacts, stronger frictional contacts, or both which enhances the shear thickening response (115; 1).

As mentioned, the most commonly encountered shear thickening and shear jamming material is a simple suspension of cornstarch and water, sometimes called "Oobleck". This system is often studied in research of dense suspensions as it is available in large quantities and easy to prepare. It is also used regularly in science outreach where it serves as a striking example of non-Newtonian fluid flow. Despite this ubiquity, the rheology of other common

household starches in suspensions has not been studied. Simple questions such as do other starch suspensions shear thicken, how does the viscosity diverge as the packing fraction is increased, and other questions have been left unaswered in the literature.

In this study, we measure the rheology of suspensions of cornstarch, potato starch, and wheat starch to determine if potato starch and wheat starch suspensions show similar rheology to that of the prototypical cornstarch suspension. By comparing similar packing fractions from different starch systems we find that the qualitative behavior of thickening is similar to that of cornstarch suspensions but quantatively there are stark differences. In particular, we find that the viscosity of wheat starch suspensions and potato starch suspensions diverge much differently than that of cornstarch. We quantify these differences by fitting all starch rheology to a Wyart-Cates model that allows us to concretely identify the differences in phase behavior between the three suspensions. These findings constitute the first evidence that other starch systems show qualitatively similar rheology to that of cornstarch suspensions, but with different details about how changes in packing fraction impact their non-Newtonian behavior.

5.2 Measurements

All three starches used in this study, corn, potato, and wheat were sourced from Sigma-Aldrich. Particles were suspended in de-ionized water that is X percent Cesium Chloride by weight in order to density match the particles to the suspending medium to avoid sedimentation during experiments. To prepare suspensions of known volume fractions we massed out mixtures of particles and suspending medium and converted their masses to volumes using their densities. To ensure reproducible results the suspensions were then let to sit for an hour and were measured within 12 hours of preparation.

Rheology of all suspensions was carried using an Anton-Paar MCR-31 stress controlled rheometer using a 25mm parallel plate geometry. We used a solvent trap to mitigate evap-

oration during our measurements. Gap heights for all measurements were kept near 1cm, a length that exceeds ten particle diameters in order to avoid ordering near the walls. To standardize the shear history for all samples we apply a preshear of x Pa of shear stress for y seconds after loading. Following our preshear we measure two successive forward and backward shear stress sweeps and report the average the viscosity over all four runs. The highest stress measured was set by observing when the exposed surface of the suspension began to go unstable and then stopping the experiment and using that stress as the highest stress in the stress sweep.

5.3 Results

5.3.1 Steady State Rheology

Steady state rheology for a variety of packing fractions for each starch system is shown in Fig. 5.1, with Fig. 5.1a showing potato starch rheology, Fig. 5.1b showing cornstarch rheology, and finally Fig. 5.1c showing wheat starch rheology. Each suspension shows shear thickening at higher packing fractions and an approximately Newtonian rheology for the lowest packing fractions. Qualitatively these curves look similar in that they show shear thickening but looking at similar packing fractions across the three different starch systems shown in Fig. 5.2 reveals stark differences.

5.3.2 Fitting Rheology Data to Wyart-Cates Model

Beyond comparing individual flow curves as is done in Fig. 5.2, we can fit the flow curves to a Wyart-Cates model to extract phase diagrams, as is outlined in 1.2.2. In particular, we are going to use the following form of the Wyart-Cates model that assumes the viscosity of

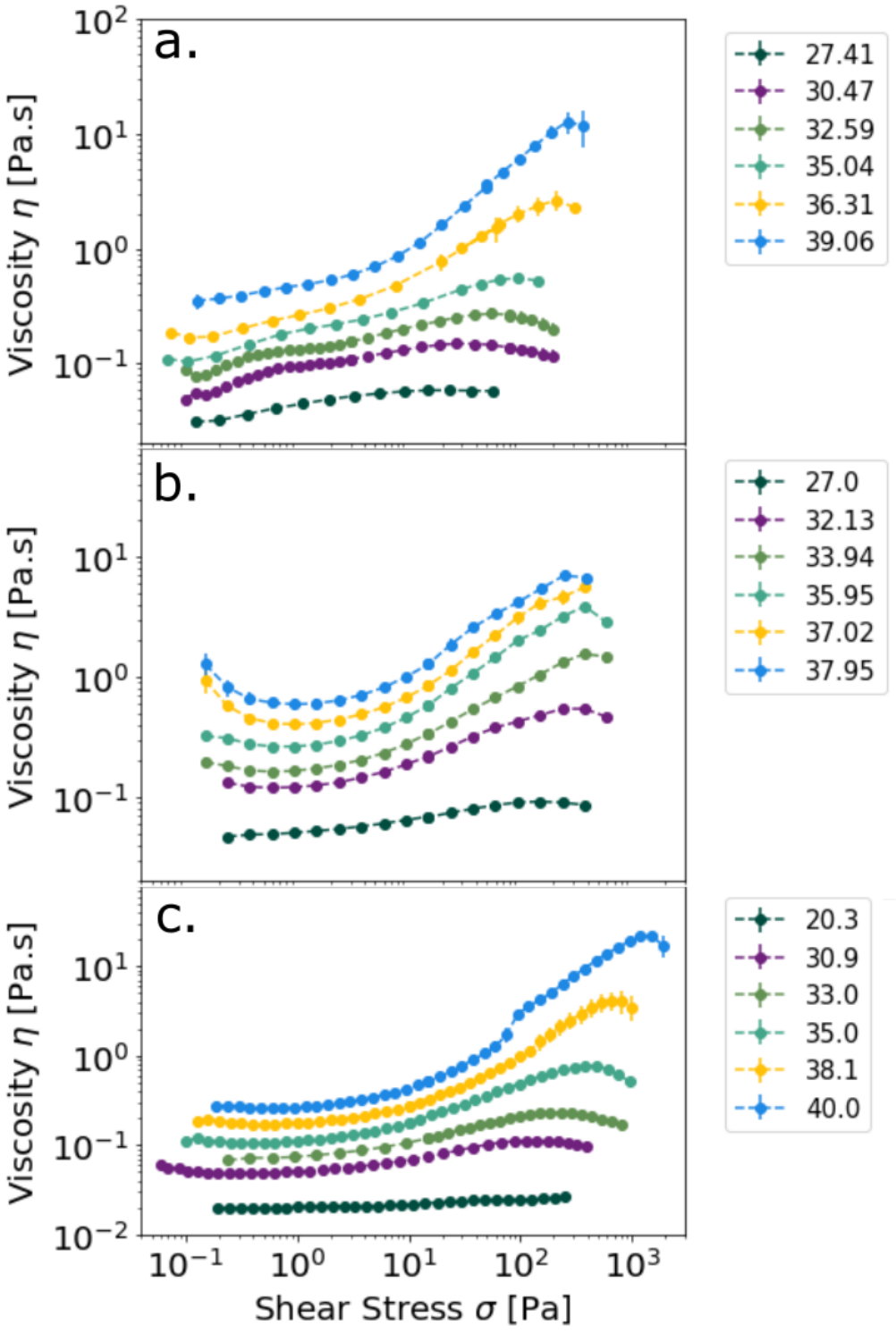

Figure 5.1: Shear rheology for various packing fractions of potato starch suspensions (a), cornstarch suspensions (b), and wheat starch suspensions (c). Colors in the legends denote the packing fractions. Each curve is an average of four measurements that come from two forward and backward stress sweeps that were taken after an initial preshear. Error bars are given by the standard deviation of the four measurements at this scale is often smaller than the point size.

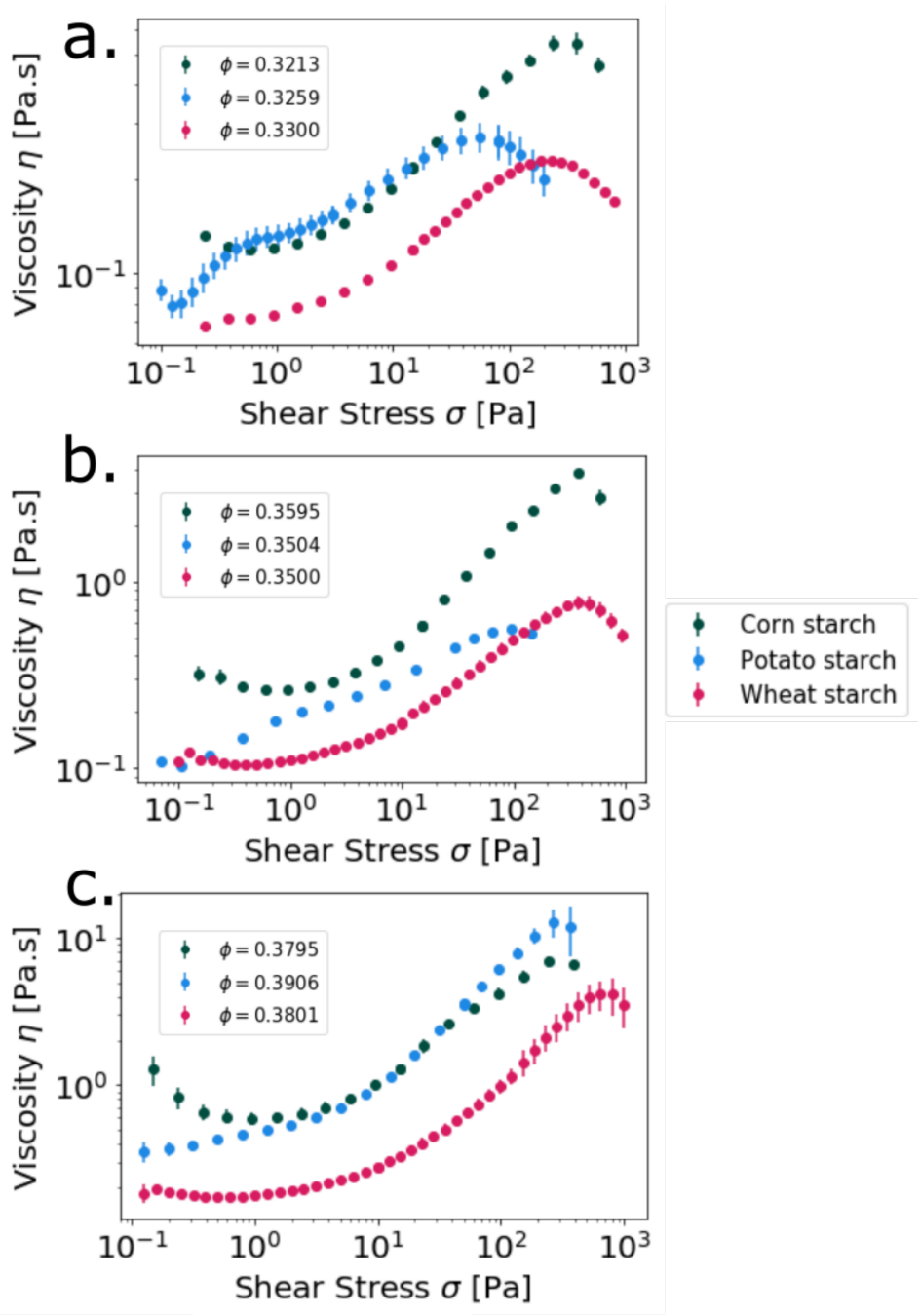

Figure 5.2: Steady state shear rheology with viscosity η plotted as a function of shear stress τ. Data shown for three different approximately equal packing fractions, ≈ 0.32 in (a), ≈ 0.35 in (b), and ≈ 0.38 in (c). from three starch systems, cornstarch in dark blue, potato starch in light blue, and wheat starch in red.

a suspension as a function of stress τ and packing fraction ϕ takes the following form:

$$\eta = \eta_0(1 - \frac{\phi}{\phi_J(\tau)})^{-\alpha}, \tag{5.1}$$

where η_0 is the suspending solvent viscosity, α is a fit parameters, and we take the stress dependent jamming packing fraction to be $\phi_J(\tau) = \phi_m(1 - \exp(\frac{\tau}{\tau^*})) + \phi_0 \exp(\frac{\tau}{\tau^*})$ where ϕ_m is the shear jamming packing fraction, ϕ_0 is the frictionless jamming packing fraction, and τ^* is the characteristic stress scale for shear thickening. With four fit parameters to determine for each starch system, ϕ_0, ϕ_m, τ^*, and α, fitting each data set in Fig. 5.1 is difficult unless we can isolate some of these fit parameters and determine them without knowing the others. To do this we note that Wyart-Cates theory tells us that the low viscosity data should diverge as:

$$\eta_r = (1 - \frac{\phi}{\phi_0})^{-\alpha}, \tag{5.2}$$

and the high viscosity data should diverge as:

$$\eta_r = (1 - \frac{\phi}{\phi_m})^{-\alpha}. \tag{5.3}$$

Therefore we can fit the lowest viscosity data points for each curve in Fig. 5.1 to equation (5.2) and fit the highest viscosity data points for each curve in Fig. 5.1 to (5.3). With the parameters ϕ_m, ϕ_0, and α determined for each starch system we can get an idea of the quality of the fits by plotting $\eta_r^{-\frac{1}{\alpha}}$ vs ϕ as in Fig. 5.3a and $\eta_r^{-\frac{1}{\alpha}}$ vs ϕ as in Fig Fig. 5.3b. The data is shown as colored triangles, with red for potato starch, blue for wheat starch, and green for cornstarch and each colored line is the corresponding fit. With ϕ_m, ϕ_0, and α determined the only remaining parameter to fit to is τ^*. To do this we fit equation (5.1) to the data in Fig. 5.1 for each starch system after inputting their respective values of ϕ_m, ϕ_0, and α.

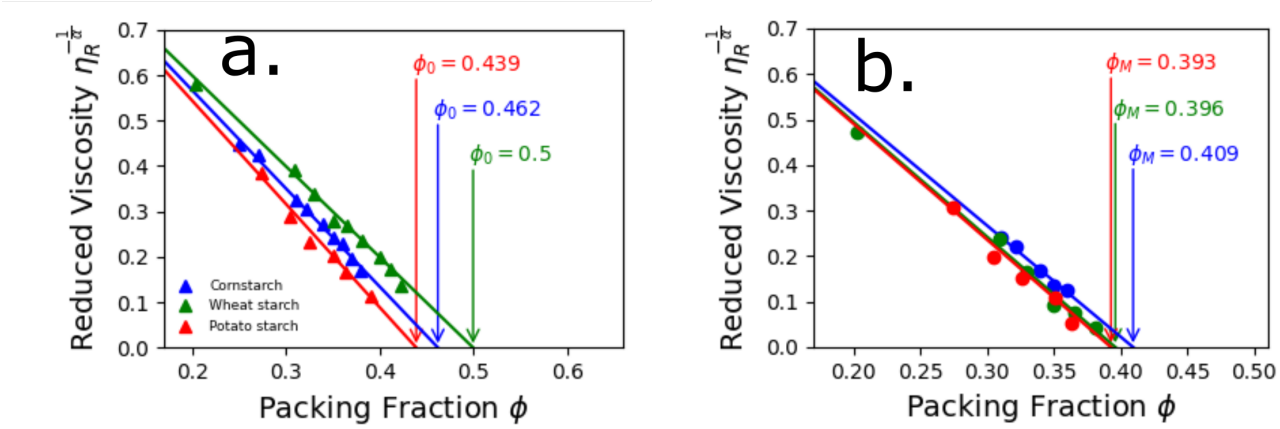

Figure 5.3: Packing fraction ϕ plotted against $\eta_r^{-\frac{1}{\alpha}}$ for low viscosity data in (a) and high viscosity data in (b). Colors correpond to the different starch systems, red for potato starch, green for wheat starch, and blue for cornstarch. The intersection at the x-axis is the relevant jamming packing fraction ϕ_0 for (a) and ϕ_m for (b).

5.3.3 Starch suspensions phase diagrams

These four fit parameters used in the Wyart-Cates model are physically significant but are easiest to interpret if used to calculate each starch suspensions phase diagram, as shown in Fig. 5.4a for wheat starch, Fig. 5.4b for cornstarch, and Fig. 5.4c for potato starch. Generating this phase diagram from fit data is the subject of appendix A. These phase diagrams plot the packing fraction ϕ against the applied shear stress τ and everywhere that is white is where CST or Newtonian like rheology is predicted, the red region is DST is predicted, and the green and grey regions are where solidification is predicted. With the green region being an anisotropic shear jammed solid that requires stress to exist and the grey region being an isotropically jammed solid that is solid at all stresses.

5.4 Discussion

All starch systems shear thicken, which is perhaps unsurprising as all of these starches are used as thickeners in cooking, but the way in which they thicken is very different. This is

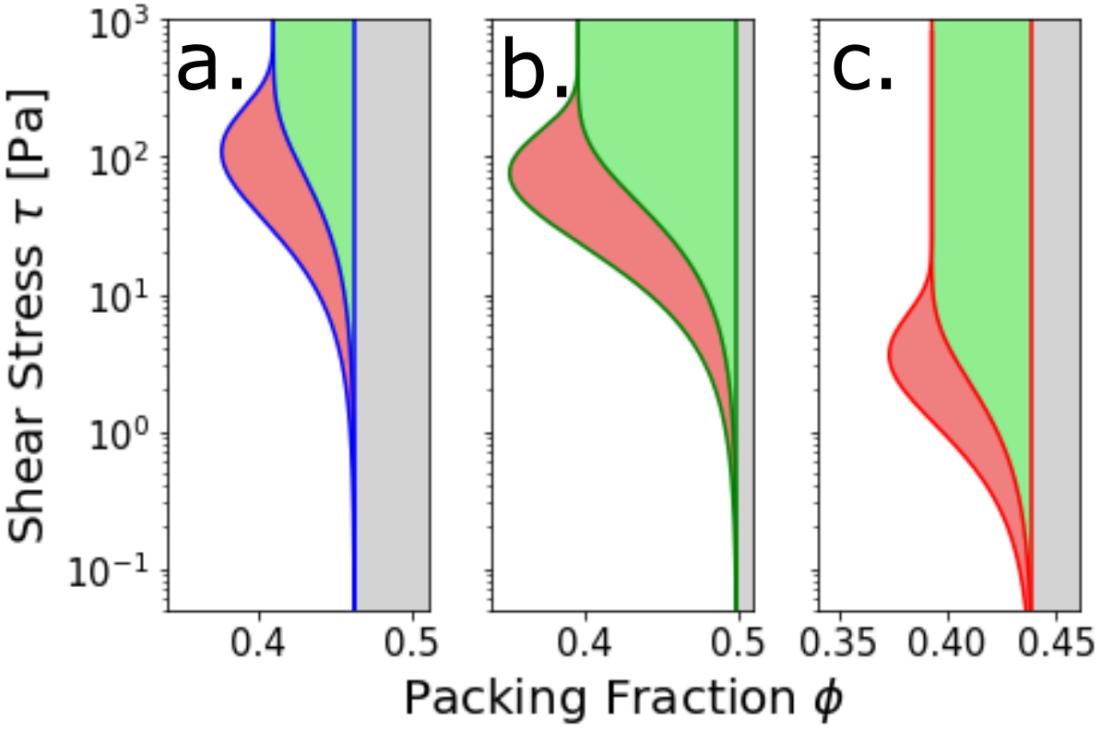

Figure 5.4: Dense suspension phase diagrams of packing fraction ϕ vs shear stress τ for each starch system (a) wheat starch, (b) cornstarch, and (c) potato starch. White region is where each suspension system shows Newtonian and CST flows, red is DST flows, and green and grey regions are jammed states. The green region is where the system is a shear jammed solid, jammed only because of the stress applied. The grey region is where the system is isotropically jammed, and thus is solid at all packing fractions and stresses.

most clear in Fig. 5.2 where similar packing fractions are co-plotted for the three different starch systems. cornstarch and wheat starch suspensions consistently shear thicken at a consistent onset shear stress for all packing fractions while potato starch has seemingly two onset stresses. This could be due to the wide distribution of particle sizes within potato starch samples, as the size of potato starch granules spans a range from 5um-100um while wheat and cornstarches have a more monodisperse distribution spanning 20um–25um and 10um-15um, respectively (116; 117). This is supported by the fact that in monodisperse systems the onset stress for shear thickening scales with the particle size as a^{-2}, and thus two different onset stresses could be multiple different particle diameters competing to thicken the suspension(12). Beyond particle size differences, the shape of these particle is often different with cornstarch being faceted, wheat starch being lenticular, and potato starch being rounded(116; 117).

Another striking difference that can be seen comparing the various figures in Fig. 5.2 is that the stress where the maximum viscosity is achieved for wheat starch and cornstarch systems stays approximately constant while potato starch shifts from $\approx 30Pa$ for $\phi = 0.3259$ and $\phi = 0.3504$ to $\approx 300Pa$ for the highest packing fraction $\phi = 0.39$. This again could be due to potato starch being polydisperse, as monodisperse suspensions typically have a constant onset stress and the stress where the viscosity is maximal is also constant (12; 118; 64).

How flow curves evolve with increasing viscosity is the defining rheological difference between these systems. This is hard to appreciate by looking at the rheology in Fig. 5.1 or Fig. 5.2, but is exactly what the fitting parameters and phase diagrams in Fig. 5.4 capture. We can see that the packing fraction for the onset of DST, SJ, and isotropic jamming are very different between all three systems. In particular, we find that the cornstarch system has the highest shear jamming volume fraction while also having the lowest packing fraction where DST is possible.

What separates these three starch systems is the morphology of the particles as all three

starch systems are made up of two polymers amylose and amylopectin. With cornstarch being 26% amylose and 74% amylopectin, wheat starch composed of 25% amylose and 75% amylopectin, and potato starch composed of 21% amylose and 79% amylopectin (119). This indicates that the large differences in the phase behavior seen in Fig. 5.4 are mainly due to the aforementioned morphological differences in the particle size, and not their chemical composition.

Therefore, this study serves as not only a case study into whether starch suspensions other than cornstarch suspensions shear thicken, but also an example of how polydispersity can drastically impact the phase behavior of these suspensions. An interesting question posed by this research is that while the shear jamming packing fraction, ϕ_m, changes drastically across the three starch systems, it is unclear if the resulting shear jammed solid has similar properties to that seen in shear jammed cornstarch suspensions, where the suspension jams into an incredibly rigid structure that can even show brittle fracture (9; 2). Doing material tests on the jammed structures of wheat and potato starch suspensions could give insight into how the shear jammed solid phase not only changes where it occurs in ϕ-τ space due to polydispersity, but also changes the material properties of the jammed structure.

By measuring the rheology of various starch suspensions we have shown that all starches considered shear thicken similar to cornstarch suspensions. By fitting each set of starch rheology data to the well-established Wyart-Cates in two steps we were able to attain physcally meaninful fit paramters such as the two jamming packing fractions ϕ_0 and ϕ_m, as well as a characteristic stress scale for thickening τ^*. Using these parameters we constructed the phase diagram for each starch system that showed striking differences between the three different starch systems, despite begin chemically similar. As the chemsitry is nearly the same across all three systems, we posit that these large differences in the phase behavior of these suspensions is due to their differences in particle polydispersity, as measured by other studies. Therefore, this work provides a definitive answer to whether or not other starch sys-

tems shear thicken but also elucidates how their thickening scales with changes in packing fraction. Beyond establishing that these suspensions thicken, this data also serves as a case study for how polydispersity can drastically impact the phase behavior of dense suspensions.

CHAPTER 6

CONCLUSIONS

This body of work comprised three distinct, but related, studies of dense suspension flow that ultimately examines how these complex flows can be understood using tools spanning chemistry to computational physics. As demonstrated by the previous chapters, the study of dense suspensions demands an interdisciplinary approach as many of the unexplored questions lie at the intersection of granular matter, tribology, statistical physics, among other disciplines. I will briefly recap the big picture of each chapter before concluding with an outlook on future research in dense suspensions.

After the introduction chapter, I outlined how to prepare and measure dense suspensions in the laboratory. This chapter describes how a simple mixture of particles and liquid can be deceivingly difficult to measure, depending on the constituents. Care needs to given to density matching, adsorption timescales, thorough mixing, and other issues in order to get reproducible results. Beyond sample preparation, measuring the resulting suspension using a rheometer requires a setup with consistent temperature, humidity, and shear history. Furthermore, watching the rheology tests for ejection or surface instabilities requires careful observation during the test and knowledge of how the rheometer is measuring the shear stress, shear rate, and ultimately viscosity. My hope is that this chapter will serve as a guide for new researchers who want to study these fascinating systems.

Chapter 3 showed how solvation forces that depend on the chemical identity of the solvent and suspending particle surface can shape suspension flows. By increasing the polymer molecular weight of the suspending solvent, an easily addressable component of the experimental system, we could elicit a shear jamming response. Before this study, tuning a single suspension to elicit a stronger shear thickening response or even a SJ response was thought to require particle scale modification. This is understandable as frictional interactions are the dominant contribution to the viscosity increase during DST and the solidification seen

during SJ, but ignores that to first establish these frictional contacts one must pierce the film of solvent separating the two particles. By invoking ideas from nanotribology and surface chemistry we argued that when this film becomes comparable to the size of the solvent molecule, the force required to break this film becomes strongly dependent on the chemistry of solvent and suspending particles. In particular, the solvation forces that depend on the affinity for the solvent molecule to the surface of the suspending particle can strongly influence how much force is required it is to make frictional contacts.

Following my experimental investigations, the next chapter was a computational investigation into transient rigid structures inside suspensions flows. This study addressed a long standing question in the dense suspension community, namely is the drastic viscous response seen during DST a product of intermittent jamming events from the frictional force network? To answer this question we simulated 2D dense suspension flows and then used a rigidity metric first introduced for studying jamming in dry granular matter. We found that system spanning rigid clusters can be found in the flow at variety of packing fractions and stresses, but strikingly where system spanning rigidity occurs is distinct from that where DST was measured. This surprising result answers the question posed at the beginning of this paragraph: incipient jamming events are not responsible for DST and instead DST occurs at lower shear stresses than where system spanning rigidity occurs. This narrows the search for physical mechanisms underlying DST, and suggests that any explanation of DST must include not just rigidity and frictional forces but how they conspire with the non-frictional forces to produce this dramatic flow behavior.

My final chapter addresses a common question when dealing with the prototypical shear thickening and shear jamming suspension, cornstarch suspended in water, do other starch suspensions show the same rheological behavior. In particular,namely whether do other common household starches such as wheat starch and potato starch also show shear thickening? Through rheological tests we established that other starch systems do indeed show shear

thickening in a qualitatively similar way to that of cornstarch, but quantitatively very different in terms of how the shear thickening behavior changes with respect to changes in packing fraction. To do this, we fit our data to the Wyart-Cates model to produce a phase diagram of when these three different starch systems show CST, DST, and SJ. We find striking differences in the jamming packing fractions of these three different systems as well different stress ranges where CST, DST, and SJ are observed. We argue that the differences in the phase behavior between these three starch systems is likely due to morphological differences in the starch particles themselves, as the chemical composition between the three is similar. This work provides not only a definitive answer to whether other starch systems show similar rheological behavior to that of cornstarch suspensions, but also provides a compelling case study on how small changes in physical morphology can lead to drastic changes in the rheology of suspension systems.

6.1 Outlook

As mentioned in the previous section, the physics of dense suspensions necessitates insights from many different seemingly disparate fields of science. This necessity made suspension science an incredibly rewarding topic to do my PhD on, as I was in constant conversation with scientists with different backgrounds from my own. These collaborations also shaped my ideas of what I find to be the most interesting or important questions that remain and is the topic of this final section.

In chapter 3 I investigated how solvation forces shape suspension flows and how they can elicit dramatic responses such as DST and SJ. As explained in the chapter, solvation forces are dominant only at nanometer scales, just before frictional contact is made and all solvent is evacuated between the two suspending particles. This and other studies have established that these nanoscale features such as solvation forces, particle asperties, or capacity for the particles to hydrogen bond have massive impacts on the bulk rheology. This suggests a fun-

damental connection between the field of tribology and dense suspension flows. Groups with expertise in atomic force microscopy have already begun to tease out this connection by using measurements of the particle surfaces at the nanoscale to explain the rheological behavior of particle suspensions. This correspondence between the bulk rheology and nanoscale properties suggests an interesting inverse problem, can we use the bulk rheology of suspensions to ascertain nanoscale features of the suspending particles? While this inverse problem may be underconstrained, i.e. multiple types of nanoscale features correspond to the same bulk rheology, even if qualitative features of the nanoscale features can be gleaned from rheological measurements this would be an incredibly powerful correspondence. It would mean that experimentalists interested in nanoscale features could do suspension rheology as a first pass test to determine if they should explore more difficult experiments such as atomic force microscopy.

Chapter 4 computationally explored the rigidity of frictional force networks inside of dense suspension flows and uncovered a new region in the dense suspension phase diagram where rigid structures span the system. When I embarked on this project originally I hoped that system spanning rigidity would not be a new region of the dense suspension phase diagram, but instead overlap exactly with DST and therefore provide a physical mechanism. This leaves a longstanding and interesting question open, is there a microscopic or mesoscopic mechanism for DST? I believe the coincidence between the onset packing fraction for system spanning rigidity and DST is a compelling reason to think that they might be related, but clearly more is required to understand the mechanisms of DST. One proposition to reconcile the two ideas is to figure out a way to meaningfully include non-frictional forces into rigidity metrics such as the (3,3) pebble game. My naive attempts to include non-frictional forces into the (3,3) pebble game were unsuccessful (see appendix C) but I'm hopeful that hydrodynamic forces may one day be included into rigidity metrics.

To conclude, I believe that dense suspension research is entering an exciting new era.

Many questions that were simply out of reach by experimental and computational physicists a decade ago are now within reach due to advances in a variety of technologies. Furthermore, the last decade has been ripe with insights that have pushed the field to a point where many of the fundamentals have been ironed out, but there are still many major open questions.

APPENDIX A

APPENDIX A: DERIVING PHASE BOUNDARIES FROM WYART-CATES MODELS

In the introduction a Wyart-Cates model is defined as any model of viscosity, η, that has the following form:

$$\eta = \eta_0(1 - \frac{\phi}{\phi_J(\tau)})^{-\alpha}, \tag{A.1}$$

where η_0 is the suspending medium viscosity, ϕ is the volume fraction of the suspension, $\phi_J(\tau)$ is a jamming packing fraction that is stress dependent, and α is a fit parameter. In order to we find the phase boundaries for DST and SJ we impose $\frac{d\eta}{d\dot{\gamma}} = \infty$ for DST and $\eta = \infty$ for SJ and solve for $\phi(\tau)$.

A.1 DST Boundary

We will first derive the phase boundary for $\phi_{DST}(\tau)$. Instead of using $\frac{d\eta}{d\dot{\gamma}} = \infty$ we will change variables by noting that $\eta = \frac{\tau}{\dot{\gamma}}$, where $\dot{\gamma}$ is the shear rate. This gives the following condition:

$$\frac{d\eta}{d\dot{\gamma}} = \frac{d\frac{\tau}{\dot{\gamma}}}{d\dot{\gamma}} = \frac{1}{\dot{\gamma}}\frac{d\tau}{d\dot{\gamma}} - \frac{\tau}{\dot{\gamma}^2} = \infty \Rightarrow \frac{1}{\dot{\gamma}}\frac{d\tau}{d\dot{\gamma}} = \infty. \tag{A.2}$$

This new condition for DST can be further simplified by noting $\dot{\gamma} > 0$ and reciprocating to give:

$$\frac{d\dot{\gamma}}{d\tau} = 0. \tag{A.3}$$

To use this new condition we again note that $\eta = \frac{\tau}{\dot{\gamma}}$ so (6.1) can be rearranged to give:

$$\dot{\gamma} = \frac{\tau}{\eta_0}(1 - \frac{\phi}{\phi_J(\tau)})^{\alpha} \tag{A.4}$$

and now using that $\frac{d\dot{\gamma}}{d\tau} = 0$ gives:

$$\frac{d\dot{\gamma}}{d\tau} = \frac{1}{\eta_0}((1 - \frac{\phi}{\phi_J(\tau)})^\alpha + \frac{\alpha\tau\phi\phi'_J(\tau)}{\phi^2_J(\tau)}(1 - \frac{\phi}{\phi_J(\tau)})^{\alpha-1}) = 0. \tag{A.5}$$

To find the solutions we can factor this expression to give:

$$\frac{1}{\eta_0}(1 - \frac{\phi}{\phi_J(\tau)})^\alpha(1 + \frac{\alpha\tau\phi\phi'_J(\tau)}{\phi^2_J(\tau) - \phi_J(\tau)\phi}) = 0, \tag{A.6}$$

which yields two solutions:

$$\phi = \phi_J(\tau) \tag{A.7}$$

and

$$\phi(\tau) = \frac{\phi^2_J(\tau)}{\phi_J(\tau) - \alpha\tau\phi'_J(\tau)}. \tag{A.8}$$

The solution is actually the SJ boundary which we will see in the next section and the second solution describes the DST boundary in a Wyart-Cates model:

$$\phi_{DST}(\tau) = \frac{\phi^2_J(\tau)}{\phi_J(\tau) - \alpha\tau\phi'_J(\tau)}. \tag{A.9}$$

A.2 SJ Boundary

This calculation is substantially more simple and the solution is one that we got as a bonus from the previous calculation. To derive the SJ line one imposes $\eta = \infty$ which gives:

$$\eta = \eta_0(1 - \frac{\phi}{\phi_J(\tau)]})^{-\alpha} = \infty \tag{A.10}$$

which clearly only has solution $\phi = \phi_J(\tau)$ so the SJ boundary is given by:

$$\phi_{SJ} = \phi_J(\tau). \tag{A.11}$$

APPENDIX B

APPENDIX B: SUPPORTING INFORMATION FOR CHAPTER 3

In this appendix we include the three plots that appear in the supporting information for the paper "The Role of Solvation Forces in Dense Suspension Flow", which is the paper chapter 3 is based on. Here, we include rheology data that was taken with various different conditions to reduce wall-slip, exhibit the Newtonian rheology of the suspendind mediums used in that paper, and show that the role of solvation forces is important for more than just fumed silica suspensions.

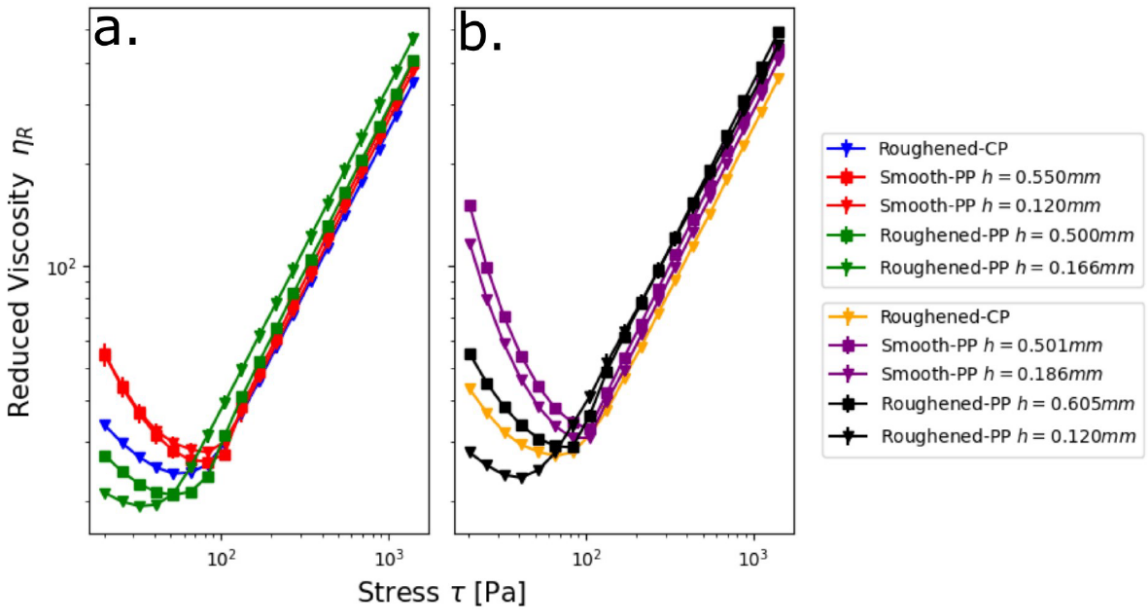

Figure B.1: Steady state rheometry data from suspensions of Aerosil OX-50 particles with $\phi = 0.337$ in PEG-200 and $\phi = 0.339$ in PEG-400. Measured separately with a 25mm parallel plate (PP) geometry with roughened top and bottom plates at two different gap heights, 25mm cone and plate (CP) geometry with $\beta = 1^\circ$ and roughened top and bottom plates, and a smooth 25mm parallel plate geometry with at two different gap heights. Viscosity is plotted as a function of shear stress for suspensions in (a) PEG-200 and (b) PEG-400.

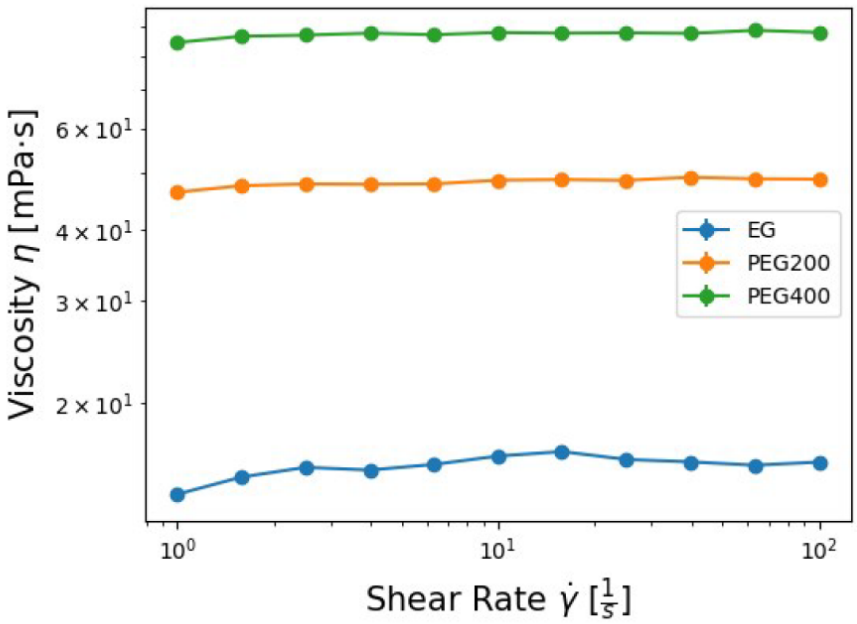

Figure B.2: Steady state rheometry data for the Newtonian suspending liquids used in the study in chapter 3 EG, PEG-200, and PEG-400.

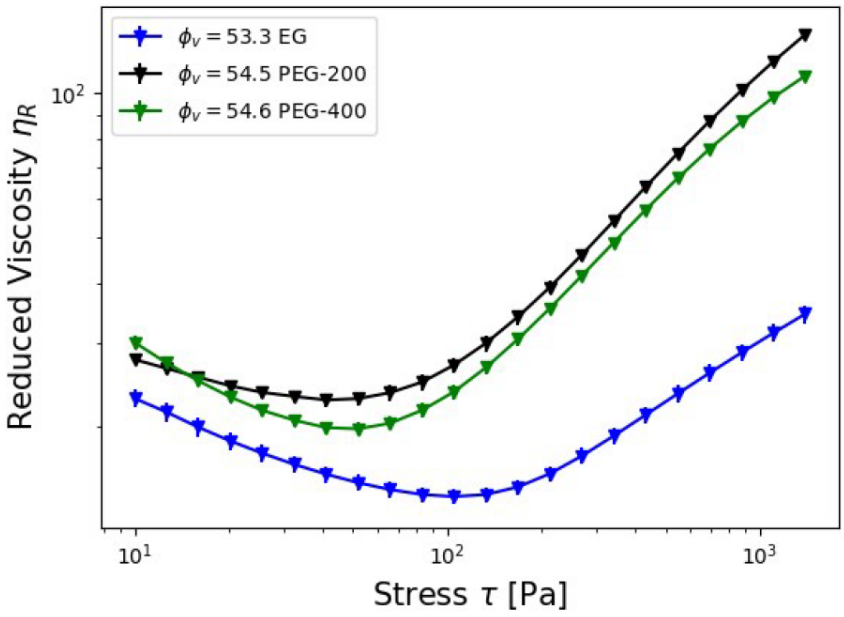

Figure B.3: Steady state rheometry data from suspensions of spherical silica particles with a diameter of 500nm. Reduced viscosity is plotted as a function of shear stress in EG, PEG-200, and PEG-400.

APPENDIX C

APPENDIX C: SUPPORTING INFORMATION FOR CHAPTER 4

This appendix is based off of the supporting information that was published with the paper "Minimally Rigid Clusters in Dense Suspension Flow" which is what chapter four is based off of. Here, we explore what happens to the cluster formation and statistics for various values of interparticle friction, different system sizes, and lastly what happens when one includes non-frictional forces into the (3,3) pebble game.

C.1 Changing sliding friction μ

We investigated as a function of sliding friction μ the minimum packing fraction for which shear jamming and DST occur and for which system-spanning clusters emerge. This is shown in Fig. C.1. The red and blue lines are obtained by fitting flow curves to the Wyart-Cates model (24) to extract ϕ_{DST} and ϕ_{SJ}. The black line indicates the minimum packing fraction where system-spanning clusters appear in at least 75% of the simulation snapshots at the highest stress simulated $\tau/\tau_0 = 100$. For each friction we simulate a range of packing fractions with a step size of $\phi = 0.005$.

We find that, within numerical accuracy of our simulations, ϕ_{rig} and ϕ_{DST} nearly coincide for the range of sliding frictions $\mu \in [0.5, 1]$. This happens to be the relevant μ range for most experiments and also the range for which simulations using only sliding friction provide the best fits to typical experimental data on dense suspensions (71). However, outside this range there are significant differences that grow as μ decreases below 0.5 or increases beyond 1.

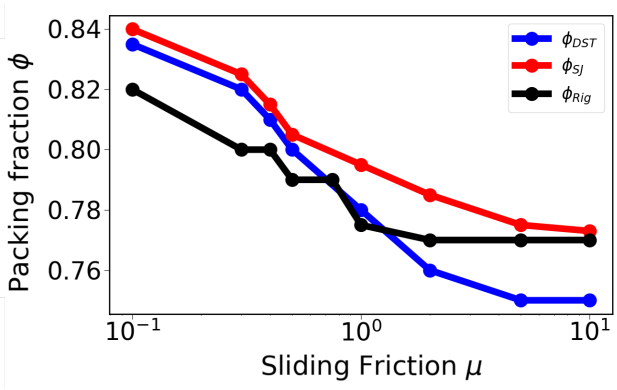

Figure C.1: Dependence of the onset packing fraction for minimally rigid, system-spanning clusters on sliding friction. Black data indicate when minimally rigid clusters first begin to span the system in the high stress state $\tau/\tau_0 = 100$. This is compared with the packing fractions where shear jamming occurs (red data) and where DST is first measured (blue data).

C.2 Identifying ϕ_{rig}

Since the suspensions are sheared and the contact networks are evolving continuously, finding a system-spanning network in one simulation snapshot does not guarantee the occurrence of another system-spanning network in the next snapshot a small strain increment later. Therefore, to identify the onset of system-spanning minimally rigid clusters for phase diagrams as in Fig. 4c of the main text a threshold for the likelihood of finding such clusters is needed. In Fig. 4c the red region corresponds to states where there are system-spanning clusters in at least 75% of the simulation snapshots. In Fig. S3a and Fig. S3b, below, we used two different thresholds, 65% and 85%, respectively. The figures show that the border between the red and blue regions changes only very slightly and that the value of ϕ_{rig} is rather insensitive to changes in thresholding.

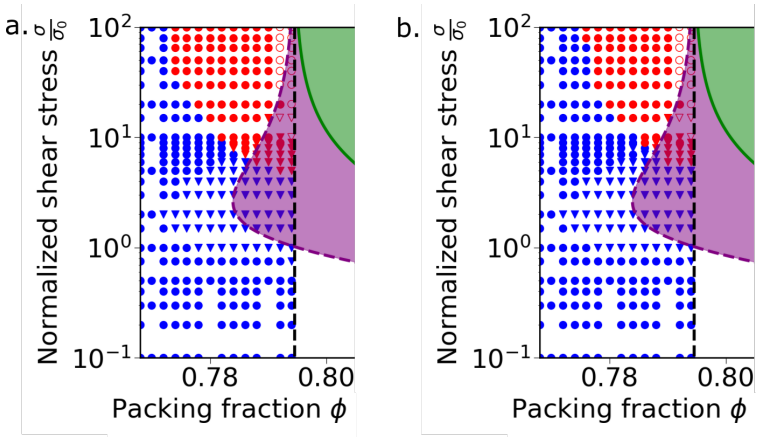

Figure C.2: Figure 4c from the main text but with different rigidity thresholds. Points in (a) are colored red if 65% of snapshots exhibit a system-spanning rigid cluster and points in (b) are colored red if 85% of snapshots exhibit a system-spanning rigid cluster. Red hollow data symbols correspond to simulations where fewer snapshots to average over were available, given that simulations in the regime very close to shear jamming are computationally expensive.

C.3 Incorporating repulsive and hydrodynamic lubrication forces as constraints into the (3,3) pebble game

In the main text the (3,3) pebble game takes into account only the frictional forces as those are the forces that have been shown to be most responsible for strong shear thickening and necessary for shear jamming. In this section we explore four ways to incorporate, in addition to friction, also the compressive and hydrodynamic lubrication forces into the (3,3) pebble to see how it changes the onset of system spanning rigidity. First, we incorporate only the compressive forces as a single constraint and find that it changes the onset of system spanning rigidty only slightly. Next, we explore three different ways to include the hydrodynamic lubrication forces as constraints. The first two ways are to ascribe hydrodynamic lubrication forces either a single or double constraint, regardless of the polarity of the force, while giving the compressive forces a single constraint. Both of these approaches make system spanning clusters appear at much lower stresses for reasons that are discussed below. Finally, we assign

both repulsive hydrodynamic lubrication forces and compressive forces a single constraint while allowing the attractive hydrodynamic lubrication forces to act as anti-constraints and find that this leads to no system spanning clusters at all packing fractions and all stresses.

It is straightforward to include also the purely repulsive forces (grey lines in Figure 1a of main text) into the pebble game analysis by considering each purely repulsive contact as constraining a single degree of freedom. This corresponds to asking how does electrostatic repulsion contribute to the transient rigidity of the system. To show how these repulsive forces change the onset of system-spanning clusters we plot in Fig. C.3 the median of the maximum cluster distribution normalized by system size vs the normalized shear stress for all packing fractions both including the repulsive forces and frictional forces (open circles - dashed lines) and including only frictional forces (circles - solid lines). Adding the repulsive forces as constraints is seen to produce only very small shifts in the size of the clusters and leaves the onset stress for the transition nearly unchanged. Curves with the same color completely agree at low stresses where there are little to no frictional or repulsive contacts yet, and they nearly agree at high stresses where almost all repulsive contacts have been converted into frictional contacts.

We now turn our attention to attempting to incorporate the hydrodynamic lubrication forces as constraints into the pebble game. Compared to including the repulsive forces this is non-trivial as the hydrodynamic lubrication forces (in the lubrication approximation) can be both attractive or repulsive. The two simplest approaches would be to assign each hydrodynamic lubrication force a single or double constraint on particle motion, regardless of the polarity of the force. To determine how this inclusion of hydrodynamic lubrication and compression forces changes the onset of system-spanning clusters we compare in Fig. C.4 the median of the maximum cluster distribution normalized by system size vs the normalized shear stress for all packing fractions for the case including both the hydrodynamic lubrication forces and compression forces as a single constraint (circles - dashed lines), the case where

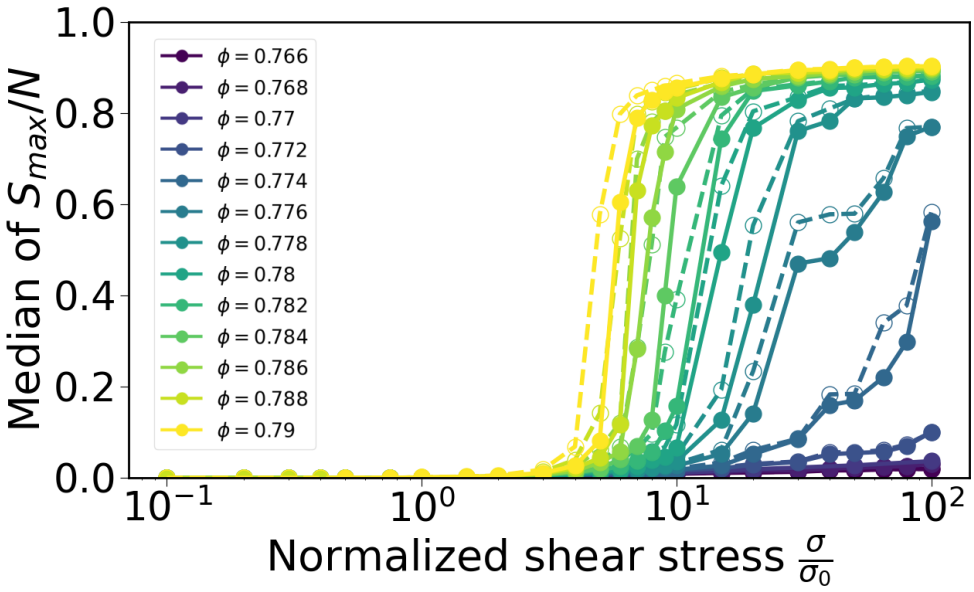

Figure C.3: Figure 4a from the manuscript but now co-plotting the results from the (3,3) pebble game that only incorporates frictional constraints (circles - solid lines) with additional data that includes compression forces (open circles - dashed lines). Median of $S_{\max}/N$ as a function of normalized shear stress τ/τ_0, data for different packing fractions ϕ are delineated by color.

hydrodynamic lubrication forces act as a double constraint and compression forces act as a single constraint (triangles - dashed lines), and the case including only frictional forces (circles - solid lines; same data as in Fig. 4a in the main text).

We first analyze the scenario where we inclusion of all non-frictional forces as single constraints while including the frictional forces in the usual way (data shown in open circles and dashed lines in Fig. C.4). We find that this way of including hydrodynamic lubrication and compressive forces produces a sharp transition to states with system-spanning rigid clusters at the same $\frac{\tau}{\tau_0} \approx 1$ for all volume fractions. This stress is precisely when frictional contacts begin to appear. It indicates that if one considers all hydrodynamic lubrication forces to be single constraints regardless of whether they are attractive or repulsive, then additional constraints from small amounts of frictional contacts are required for the system to form system-spanning rigid clusters. Furthermore, these clusters are quite different from the ones formed by purely frictional contacts as they include every particle in the system: the curves plateau at $\frac{S_{max}}{N} = 1$ instead of $\frac{S_{max}}{N} \approx 0.8$ for the analysis with only frictional constraints.

We can rationalize the onset of these clusters at $\frac{\tau}{\tau_0} \approx 1$ as follows. With only one constraint per interaction one would need six interactions per particle for it to be fully constrained in the (3,3) pebble game. To see this, consider a network of N particles where each particles has six bonds to its nearest neighbors (a triangular lattice, for example) and where each bond provides a single constraint. If we use the (3,3) pebble game to determine the rigidity of this structure we assign three pebbles per particle and distribute a single pebble to each bond. There will be $3N$ pebbles to distribute to $6N$ bonds, but since each bond is shared between two particles there are $3N$ unique bonds to distribute the pebbles to. With the number of pebbles to distribute exactly matching the number of bonds to distribute them to we can conclude that a six-coordinated structure is the minimally coordinated structure that can be rigid if bonds provide only one constraint. In our simulations, the hydrodynamic

lubrication forces extend out to a cut-off distance of $0.2a$ where a is the radius of the smallest particles. This makes the lubrication forces longer ranged than the compressive or frictional forces, and as a consequence they form a well coordinated network even at low stresses $\frac{\tau}{\tau_0} < 1$. Still, we find that the connectivity in this network is not yet large enough to form system-spanning rigid clusters. This changes once frictional interactions become activated at $\frac{\tau}{\tau_0} \approx 1$ because now each of the bonds associated with friction can carry two pebbles instead of just one.

Next, we analyze the scenario where we include compressive forces as single constraints, hydrodynamic lubrication forces as double constraints, and the frictional forces in the usual way (data shown in open triangles and dashed lines in Fig. C.4). In this case there are system spanning clusters at all stresses and all packing fractions as the highly coordinated network of hydrodynamic lubrication forces provides enough constraints to fully constrain all particles in the system, even in the low stress states (as far as the (3,3) pebble game is concerned, letting bonds associated with the lubrication forces carry two pebbles makes them effectively equivalent to frictional bonds). Since dense suspensions are known to exhibit a finite onset stress (or, equivalently, onset shear rate) for strong shear thickening and in particular DST, this assignment double constraints to lubrication forces appears produce unphysical outcomes.

While we only simulate volume fractions in the range of $\phi \in [0.766, 0.79]$ we anticipate that our results for including hydrodynamic lubrication forces as either single or double constraint carry over to lower packing fractions as long as they show strong shear thickening. This is because at any packing fraction that is dense enough for strong shear thickening there will be a highly coordinated network of hydrodynamic lubrication forces, even at low stresses. In the case where the hydrodynamic lubrication forces act as a single constraint the data in Fig. C.4 suggest that already a small amount of additional frictional constraints below the Coulomb threshold is enough to push the system to form system-spanning rigid clusters

(we note that it is important for the frictional forces to be below the Coulomb threshold: that way they provide two constraints to particle motion instead of just the one that the repulsive or hydrodynamic lubrication forces provided before the requisite stress for frictional contacts was reached). When hydrodynamic lubrication forces act as a double constraint one can get system-spanning clusters with as little as three interactions per particle, which happens already at very low packing fractions.

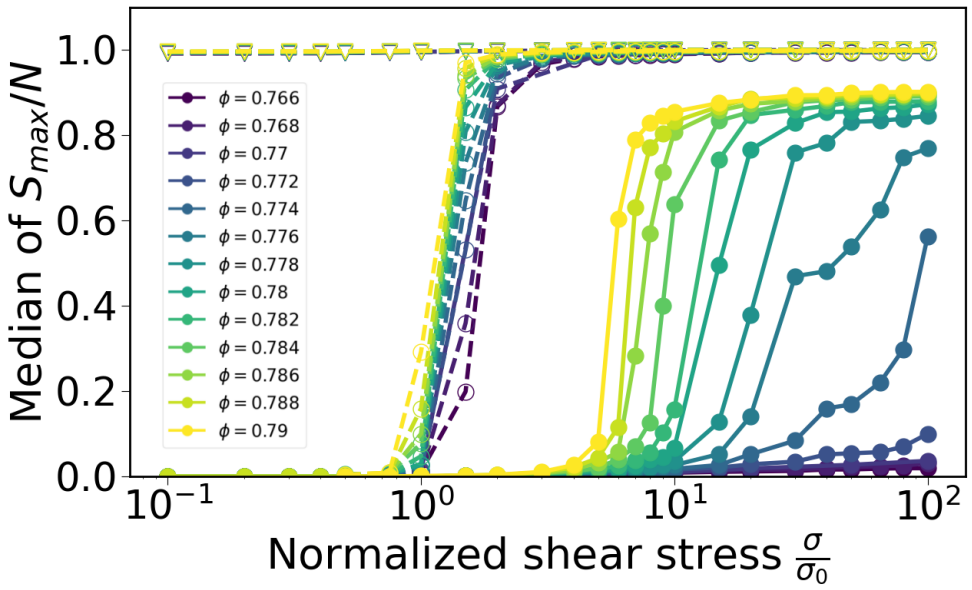

Figure C.4: Figure 4a from the manuscript but now co-plotting the results from the (3,3) pebble game that only incorporates frictional constraints (circles - solid lines) with additional data generated by our first strategy to include hydrodynamic lubrication forces as constraints by assigning all hydrodynamic lubrication forces a single constraint, regardless of the polarity (open circles - dashed lines). Median of $S^{\max}/N$ as a function of normalized shear stress τ/τ_0, data for different packing fractions ϕ are delineated by color.

Our final scenario is motivated by considering the effect hydrodynamic forces can have when a particle under shear approaches an existing cluster or is moving away from it. In the first case the lubrication interaction will be repulsive and in the second case attractive. We therefore include hydrodynamic lubrication forces into the pebble game by adding a single constraint when a repulsive lubrication force emerges, akin to sliding frictional forces

and compressive forces, and by treating an attractive lubrication force, which we view as able to disrupt existing configurations in the cluster, as an anti-constraint that can cancel out constraints from the frictional forces, compressive forces, or repulsive hydrodynamic lubrication forces. This works by assigning every repulsive force a number of constraints (2 for non-sliding frictional contacts, 1 for every other repulsive force) and assigning each attractive hydrodynamic lubrication force the ability to prune a constraint. After pruning all possible constraints we then play the (3,3) pebble game with the remaining constraints. Algorithmically this proceeds as follows:

1. Classify all repulsive forces as constraints with hydrodynamic, compressive, and frictional forces at the Coulomb criterion constraining 1 degree of freedom and the frictional forces below the Coulomb criterion constraining 2 degrees of freedom. Next, classify all attractive hydrodynamic lubrication forces as “disruptors" which are capable of pruning a constraint that constrains 1 degree of freedom.

2. For every hydrodynamic lubrication force $F_{i,j}$ classified as a disruptor attempt to find a corresponding constraint that involves particle i or particle j and delete that constraint. Note that this is not always possible as sometimes there is no corresponding constraint on particle i or j to prune.

3. With this new list of pruned constraints play the (3,3) pebble game.

This procedure captures the constraints from the repulsive hydrodynamic lubrication forces but underestimates the disrupting nature of the attractive hydrodynamic lubrication forces. Thus this procedure should give a lower bound on the ability for hydrodynamic lubrication forces to disrupt clusters. We have performed this modified pebble game and again plot the median of the maximum cluster size normalized by system size again normalized shear stress for all packing fractions both including all the forces in this modified pebble game approach (open circles - dashed lines) and including only frictional forces (circles - solid lines) shown in Fig. C.5. It is apparent that his ad-hoc method of including all forces into the constraint

counting procedure acts to destabilize all clusters for all packing fractions and stresses. There are at least two ways in which incorporating hydrodynamic lubrication forces as constraints in this way is incomplete. The first is that it completely ignores the tangential components of the hydrodynamic lubrication forces, although these are a logarithmic in the separation distance as opposed to a linear dependence that the normal component has. Second, and perhaps more importantly, this algorithm is liable to use minuscule attractive hydrodynamic lubrication forces to disrupt a frictional force constraint that is orders of magnitude larger in force.

In summary, we have analyzed non-frictional forces in the (3,3) pebble game in four distinct ways: (1) we included the compressive forces as a single constraint, (2) we considered hydrodynamic lubrication forces and compressive forces as a single constraint, (3) we included hydrodynamic lubrication forces as a double constraint and compressive forces as a single constraint, and (4) we developed an ad-hoc method where compressive and repulsive forces are included as a single constraint while attractive hydrodynamic lubrication forces are modeled as disruptors to constraints. Including only compressive forces as a single constraint only slightly shifts the onset of system-spanning rigid clusters and has no impact on the results from the main text. Including the hydrodynamic lubrication forces is much less straightforward and, since these forces are ultimately the forces that lubricate particle interactions and keep the system flowing, the interpretation of the clusters is not as clear. Despite this, if we include hydrodynamic lubrication forces by ascribing a single constraint to each compressive and hydrodynamic lubrication force, regardless of the polarity of the force, we find that all packing fractions show system-spanning rigid clusters near $\frac{\tau}{\tau_0} \approx 1$. If we ascribe a double constraint to each hydrodynamic lubrication force along with a single constraint for each compressive force, this leads to system-spanning rigid clusters at all packing fractions and all stresses. Finally, if we ascribe a single constraint to repulsive hydrodynamic lubrication forces and a single anti-constraint to attractive hydrodynamic lubrication forces, this

leads to the absence of system-spanning rigid clusters at all packing fractions and stresses.

The upshot is that those interactions dominate the behavior for which double constraints have been assigned. The (3,3) pebble game for dry granular systems and as well as suspensions assigns double constraints to frictional contacts below the Coulomb threshold (but note that in suspensions, motivated by the underlying physics, there is not only a Coulomb threshold but also a minimum stress scale τ_0 for thin lubrication layers to rupture and contact friction to set in). Whenever these double constraint interactions are present, and only once they become activated, system-spanning rigid clusters can form. But the clusters that consist of hydrodynamic lubrication constraints are fundamentally different from those that consist of purely repulsive or frictional constraints and it is unclear if they constrain the particles in a way that meaningfully corresponds to rigidity. This implies that none of the above scenarios for including hydrodynamic lubrication forces into the pebble game quite captures the correct physics of dense suspensions. Extending the pebble game algorithm in a way that can properly deal with both hydrodynamic and frictional forces is not straightforward and care will be needed because the physics behind these two types of forces is very different. This remains an interesting direction for future exploration.

C.4 (3,3) vs (3,2) Pebble Game

For systems in two dimensions with periodic boundary conditions, as studied here, global rotations are not allowed due to symmetry arguments. Therefore, there are only two degrees of freedom per particle coming from the two translational degrees of freedom suggesting that we should instead play the (3,2) pebble game instead of the (3,3) pebble game. In practice, we find that our results are largely insensitive to this detail. This is indicated by Fig. C.6 here we co-plot the median of $S_{\max}/N$ as a function of normalized shear stress τ/τ_0 for results from the (3,3) pebble game (circles - solid lines) together with the results from the (3,2) pebble game (open circles - dashed lines). While some points move around slightly, the position

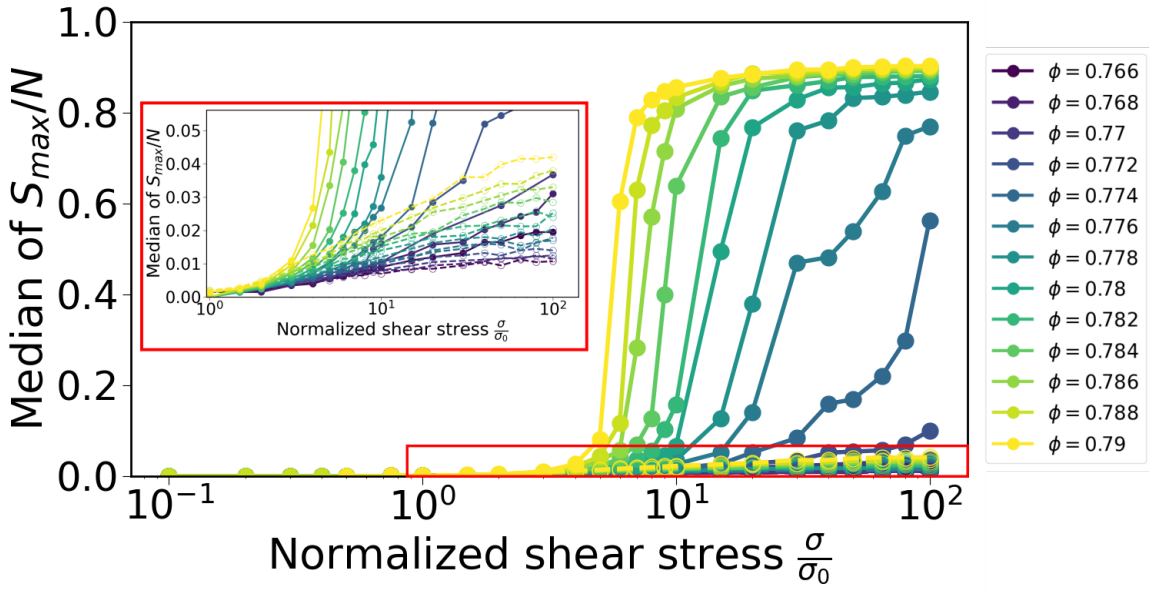

Figure C.5: Figure 4a from the manuscript but now co-plotting the results from the (3,3) pebble game that only incorporates frictional constraints (circles - solid lines) with additional data generated by our second strategy to include hydrodynamic lubrication forces as both constraints and disruptors to constraints (open circles - dashed lines). Median of $S_{\max}/N$ as a function of normalized shear stress τ/τ_0, data for different packing fractions ϕ are delineated by color. The red-boxed inset plot corresponds to a zoomed in version of the data contained in the red box in the lower right-hand corner of the plot that contains all the results from the second strategy to include hydrodynamic lubrication forces into the pebble game.

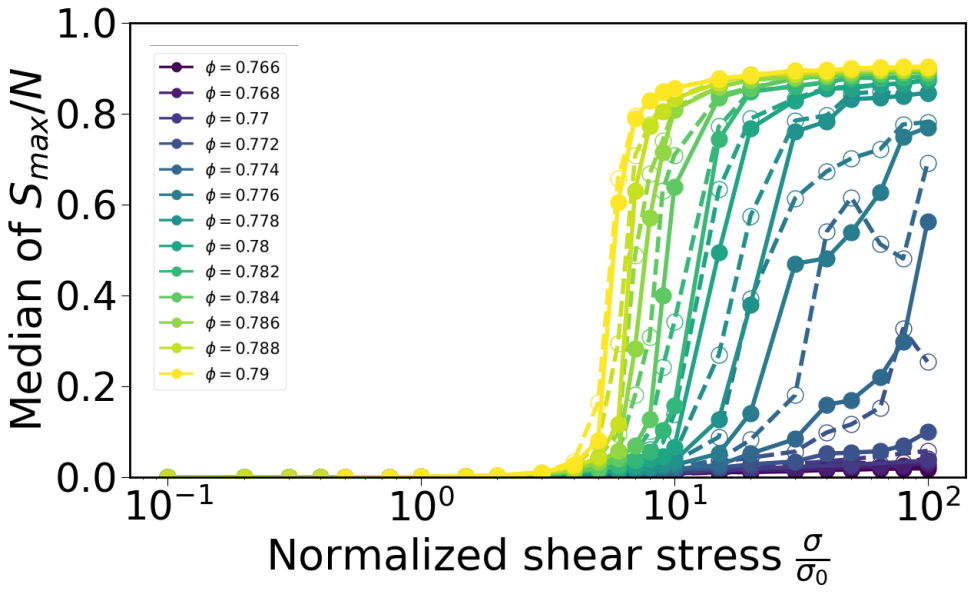

Figure C.6: Figure 4a from the manuscript but now co-plotting the results from the (3,3) pebble game (circles - solid lines) with the results from the (3,2) pebble game (open circles - dashed lines). Median of $S_{\max}/N$ as a function of normalized shear stress τ/τ_0, data for different packing fractions ϕ are delineated by color.

of the transition to system spanning clusters remains unchanged, similar to what has been found in 2D frictional granular packing's (79). One reason for the close agreement between the (3,3) and (3,2) pebble game results is that many of the clusters we measure are system spanning clusters, where fixed wall boundary conditions and periodic boundary conditions provide similar constraints. This also explains why the maximum disparity between the (3,3) and (3,2) pebble games is for packing fractions where we do not yet find system spanning clusters.

C.5 Larger Strain Return Maps

We have re-plotted the return maps from Figure 3(d-f) of the main text but instead of plotting the largest cluster from the subsequent snapshot $S^{max}_{\gamma+\delta\gamma}$ on the y-axis we plot $S^{max}_{\gamma+2\delta\gamma}$ in Fig. C.5(a-c), $S^{max}_{\gamma+3\delta\gamma}$ in Fig. C.5(d-f), and $S^{max}_{\gamma+4\delta\gamma}$ in Fig. C.5(g-i). Where the first column

of plots corresponds to $\phi = 0.77$, the second column of plots corresponds to $\phi = 0.78$, and finally the third column shows $\phi = 0.79$. Looking down each column we see that while individual points move around in their positions, the overall clustering at specific stresses does not change qualitatively. Furthermore, at each packing fraction the return maps are qualitatively similar to those for $S^{max}_{\gamma+\delta\gamma}$, as in the main text. We would expect to see a qualitative difference between Fig. C.5 and Figure 3(d-f) from the main text if we chose a $\delta\gamma$ that is comparable with the lifetime of an individual cluster. With no qualitative difference between Fig. C.5 and Figure 3(d-f) from the main text we conclude that our strain step of $\delta\gamma = 0.1$ is sufficiently large to sample a new population of clusters at each step. This is further corroborated by the movie included in this SI.

C.6 Maximum Cluster Distributions for Systems Above and Below DST

Here, we investigate further maximum cluster distributions above and below the DST transition. In Fig. C.8a-b we plot the maximum cluster distributions for just below the DST transition at $\phi = 0.774$ for stresses $\frac{\tau}{\tau_0} = 5$, $\frac{\tau}{\tau_0} = 50$ in plot a and $\frac{\tau}{\tau_0} = 10$, $\frac{\tau}{\tau_0} = 30$, and $\frac{\tau}{\tau_0} = 80$ in plot b. In Fig. C.8c-d we plot the maximum cluster distributions for just above DST at $\phi = 0.776$ for stresses $\frac{\tau}{\tau_0} = 5$, $\frac{\tau}{\tau_0} = 50$ in plot a and $\frac{\tau}{\tau_0} = 10$, $\frac{\tau}{\tau_0} = 30$, and $\frac{\tau}{\tau_0} = 80$. We see that Fig. C.8a and Fig. C.8d look very similar just as Fig. C.8b and Fig. C.8c look very similar. The main changes between the distributions of these two packing fractions is that there are slightly larger populations of large clusters for the higher packing fraction, something that is also reflected in Figure 4a from the main text.

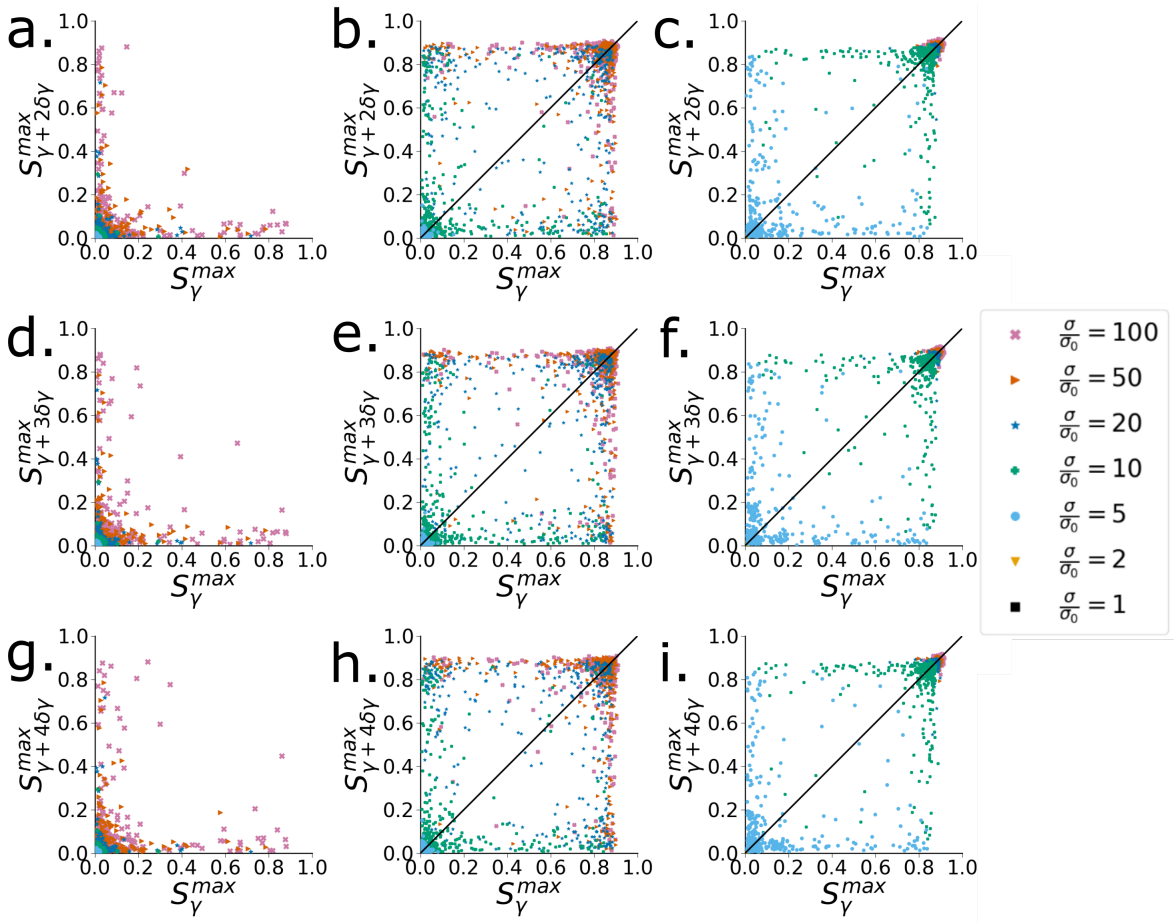

Figure C.7: Return maps from Figure 3 in the main text but now with the y-axis we plot $S^{max}_{gamma+2\delta\gamma}$(a-c), $S^{max}_{gamma+3\delta\gamma}$(d-f), and $S^{max}_{gamma+4\delta\gamma}$(g-i). The first column shows the return maps for $\phi = 0.77$, second column is for$\phi = 0.78$, and the final column corresponds to $\phi = 0.79$. Inset shows zoom of data including all forces.

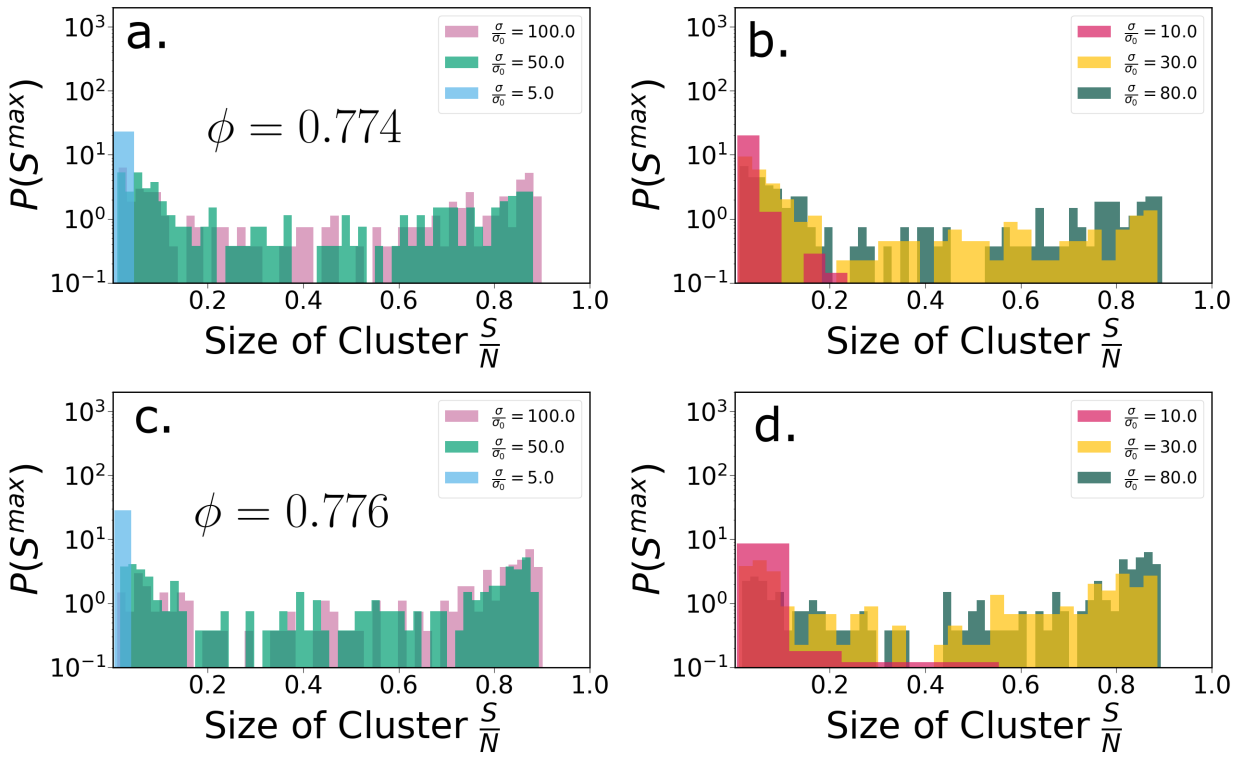

Figure C.8: Size distributions $P(S^{\max})$ for the largest rigid clusters within the network of frictional contacts. Plots (a-b) correspond to $\phi = 0.774$ for three different stresses in each plot and plots (c-d) correspond to $\phi = 0.776$ for three different stresses in each plot.

REFERENCES

[1] James, N. M., Han, E., de la Cruz, R. A. L., Jureller, J. & Jaeger, H. M. Interparticle hydrogen bonding can elicit shear jamming in dense suspensions. *Nat. Mater.* **17**, 965–970 (2018).

[2] Roché, M., Myftiu, E., Johnston, M. C., Kim, P. & Stone, H. A. Dynamic fracture of nonglassy suspensions. *Phys. Rev. Lett.* **110**, 148304 (2013).

[3] Peters, I. R., Majumdar, S. & Jaeger, H. M. Direct observation of dynamic shear jamming in dense suspensions. *Nature* **532**, 214–217 (2016).

[4] Singh, A., Mari, R., Denn, M. M. & Morris, J. F. A constitutive model for simple shear of dense frictional suspensions. *J. Rheol.* **62**, 457–468 (2018).

[5] Brown, E. & Jaeger, H. M. Shear thickening in concentrated suspensions: phenomenology, mechanisms and relations to jamming. *Reports on Progress in Physics* **77**, 046602 (2014).

[6] Royer, J. R., Blair, D. L. & Hudson, S. D. Rheological signature of frictional interactions in shear thickening suspensions. *Phys. Rev. Lett.* **116**, 188301 (2016).

[7] Mari, R., Seto, R., Morris, J. F. & Denn, M. M. Shear thickening, frictionless and frictional rheologies in non-Brownian suspensions. *J. Rheol.* **58**, 1693–1724 (2014).

[8] James, N. M., Han, E., de la Cruz, R. A. L., Jureller, J. & Jaeger, H. M. Interparticle hydrogen bonding can elicit shear jamming in dense suspensions. *Nat. Mater.* **17**, 965 (2018).

[9] Peters, I. R., Majumdar, S. & Jaeger, H. M. Direct observation of dynamic shear jamming in dense suspensions. *Nature* **532**, 214–217 (2016).

[10] Han, E., Peters, I. R. & Jaeger, H. M. High-speed ultrasound imaging in dense suspensions reveals impact-activated solidification due to dynamic shear jamming. *Nat. Commun.* **7**, 12243 (2016).

[11] Majumdar, S., Peters, I. R., Han, E. & Jaeger, H. M. Dynamic shear jamming under extension in dense granular suspensions. *Phys. Rev. E* **95**, 012603 (2017).

[12] Guy, B. M., Hermes, M. & Poon, W. C. K. Towards a unified description of the rheology of hard-particle suspensions. *Phys. Rev. Lett.* **115**, 088304 (2015).

[13] Cheng, X., McCoy, J. H., Israelachvili, J. N. & Cohen, I. Imaging the microscopic structure of shear thinning and thickening colloidal suspensions. *Science* **333**, 1276–1279 (2011).

[14] Lin, N. Y. C. *et al.* Hydrodynamic and contact contributions to continuous shear thickening in colloidal suspensions. *Phys. Rev. Lett.* **115**, 228304 (2015).

[15] Seto, R., Mari, R., Morris, J. F. & Denn, M. M. Discontinuous shear thickening of frictional hard-sphere suspensions. *Phys. Rev. Lett.* **111**, 218301 (2013).

[16] Mari, R., Seto, R., Morris, J. F. & Denn, M. M. Nonmonotonic flow curves of shear thickening suspensions. *Phys. Rev. E* **91**, 052302 (2015).

[17] Ness, C. & Sun, J. Shear thickening regimes of dense non-Brownian suspensions. *Soft Matter* **12**, 914–924 (2016).

[18] Raghavan, S. R., Walls, H. J. & Khan, S. A. Rheology of silica dispersions in organic liquids: new evidence for solvation forces dictated by hydrogen bonding. *Langmuir* **16**, 7920–7930 (2000).

[19] Jackson, G. L. *et al.* Designing stress-adaptive dens esuspensions using dynamic covalent chemistry. *55* 6453–6461 (2022).

[20] Mari, R. & Seto, R. Force transmission and the order parameter of shear thickening. *Soft Matter* **15**, 6650–6659 (2019).

[21] Mari, R., Seto, R., Morris, J. F. & Denn, M. M. Discontinuous shear thickening in brownian suspensions by dynamic simulation. *Proc. Natl. Acad. Sci. U.S.A* **112**, 15326–15330 (2015).

[22] Hsu, C.-P., Ramakrishna, S. N., Zanini, M., Spencer, N. D. & Isa, L. Roughness-dependent tribology effects on discontinuous shear thickening. *Proc. Nat. Acad. Sci.* (2018).

[23] Rathee, V., Blair, D. L. & Urbach, J. S. Localized stress fluctuations drive shear thickening in dense suspensions. *Proceedings of the National Academy of Sciences* **114**, 8740–8745 (2017).

[24] Wyart, M. & Cates, M. E. Discontinuous shear thickening without inertia in dense non-Brownian suspensions. *Phys. Rev. Lett.* **112**, 098302 (2014).

[25] Ewoldt, M. T. J., R. H. & Caretta, L. M. Experimental challenges of shear rheology: how to avoid bad data,. In Spagnolie, S. (ed.) *Complex Fluids in Biological Systems*, 207–241 (Springer, 2015).

[26] Macosko, C. W. *Rheology: Principles, Measurements, and Applications* (Wiley, 1996).

[27] Royer, J. R., Blair, D. L. & Hudson, S. D. Rheological signature of frictional interactions in shear thickening suspensions. *Phys. Rev. Lett.* **116**, 188301 (2016).

[28] Hermes, M. *et al.* Unsteady flow and particle migration in dense, non-Brownian suspensions. *J. Rheol.* **60**, 905–916 (2016).

[29] Fernandez, N. *et al.* Microscopic mechanism for shear thickening of non-Brownian suspensions. *Phys. Rev. Lett.* **111**, 108301 (2013).

[30] Morris, J. F. Lubricated-to-frictional shear thickening scenario in dense suspensions. *Phys. Rev. Fluids* **3**, 110508 (2018).

[31] Radhakrishnan, R., Royer, J. R., Poon, W. C. K. & Sun, J. Force chains and networks: wet suspensions through dry granular eyes. *Gran. Matt.* **22**, 29 (2020).

[32] Singh, A., Ness, C., Seto, R., de Pablo, J. J. & Jaeger, H. M. Shear thickening and jamming of dense suspensions: The "roll" of friction. *Phys. Rev. Lett.* **124**, 248005 (2020).

[33] James, N. M., Hsu, C.-P., Spencer, N. D., Jaeger, H. M. & Isa, L. Tuning interparticle hydrogen bonding in shear-jamming suspensions: Kinetic effects and consequences for tribology and rheology. *J. Phys. Chem. Lett.* **10**, 1663–1668 (2019).

[34] Buttinoni, I. *et al.* Direct observation of impact propagation and absorption in dense colloidal monolayers. *Proc. Natl. Acad. Sci. U.S.A* **114**, 12150–12155 (2017).

[35] James, N. M., Xue, H., Goyal, M. & Jaeger, H. M. Controlling shear jamming in dense suspensions via the particle aspect ratio. *Soft Matter* **15**, 3649–3654 (2019). URL `http://dx.doi.org/10.1039/C9SM00335E`.

[36] Yang, W., Yang, W., Pei, X., Zhou, F. & Xue, Q. Contribution of surface chemistry to the shear thickening of silica nanoparticle suspensions. *Langmuir* **33**, 1037–1042 (2017).

[37] Bourrianne, P., Niggel, V., Polly, G., Divoux, T. & McKinley, G. H. Unifying disparate experimental views on shear-thickening suspensions. *arXiv preprint arXiv:2001.02290* (2020).

[38] Nakamura, H., Makino, S. & Ishii, M. Shear-thickening behavior of concentrated monodispersed colloidal suspensions. *The Society of Rheology, Japan* **47**, 9–15 (2019).

[39] Laun, H. M. Rheological properties of aqueous polymer dispersions. *Angew. Makromol. Chem.* **123**, 335–359 (1984).

[40] Xu, Q., Singh, A. & Jaeger, H. M. Stress fluctuations and shear thickening in dense granular suspensions. *J. Rheol.* **64**, 321–328 (2020).

[41] Shenoy, S. S. & Wagner, N. J. Influence of medium viscosity and adsorbed polymer on the reversible shear thickening transition in concentrated colloidal dispersions. *Rheologica Acta* **44**, 360–371 (2005).

[42] Zhang, Q., Wu, C., Song, Y. & Zheng, Q. Rheology of fumed silica / polypropylene glycol dispersions. *Polymer* **148**, 400–406 (2018).

[43] Jiang, T. & Zukoski, C. F. Role of particle size and polymer length in rheology of colloid–polymer composites. *Macromolecules* **45**, 9791–9803 (2012).

[44] Raghavan, S. R., Walls, H. J. & Khan, S. A. Rheology of silica dispersions in organic liquids: New evidence for solvation forces dictated by hydrogen bonding. *Langmuir* **16**, 7920–7930 (2000).

[45] Keentok, M. & Xue, S.-C. Edge fracture in cone-plate and parallel plate flows. *Rheological Acta* **38**, 321–348 (1999).

[46] Maharjan, R., O'Reilly, E., Postigilione, T., Klimenko, N. & Brown, E. Intermittent dilation and its coupling to stress in discontinuous shear thickening suspensions. *arXiv preprint arXiv:1606.07650* (2020).

[47] Brown, E. & Jaeger, H. M. The role of dilation and confining stresses in shear thickening of dense suspensions. *Journal of Rheology* **56**, 875 (2012).

[48] Han, E., Wyart, M., Peters, I. R. & Jaeger, H. M. Constitutive relations for shear fronts in shear-thickening suspensions. *Phys. Rev. Fluids* **3**, 073301 (2018).

[49] Han, E. *et al.* Dynamic jamming of dense suspensions under tilted impact. *Phys. Rev. Fluids* **4**, 063304 (2019). URL `https://link.aps.org/doi/10.1103/PhysRevFluids.4.063304`.

[50] Wyart, M. & Cates, M. E. Discontinuous shear thickening without inertia in dense non-Brownian suspensions. *Phys. Rev. Lett.* **112**, 098302 (2014).

[51] Park, N., Rathee, V., Blair, D. L. & Conrad, D. Contact networks enhance shear thickening in attractive colloid-polymer mixtures. *Phys. Rev. Lett.* **122**, 228003 (2019).

[52] Anderson, B. J. & Zukoski, C. F. Nanoparticle stability in polymer melts as determined by particle second virial measurement. *Macromolecules* **40**, 5133–5140 (2007).

[53] Atkins, D. T. & Ninham, B. W. Surface and structural forces measured between silica surfaces in 1,2-ethanediol. *Colloids and Surfaces A* **129-130**, 23–32 (1997).

[54] Singh, A., Pednekar, S., Chun, J., Denn, M. M. & Morris, J. F. From yielding to shear jamming in a cohesive frictional suspension. *Phys. Rev. Lett.* **122**, 098004 (2019).

[55] Brown, E. *et al.* Generality of shear thickening in dense suspensions. *Nat. Mater.* **9**, 220–224 (2010).

[56] Pattanayek, S. K. & Juvekar, V. A. Prediction of Adsorption of Nonionic Polymers from Aqueous Solutions to Solid Surfaces. *Macromolecules* **35**, 9574–9585 (2002).

[57] Trens, P. & Denoyel, R. Conformation of Poly(ethylene glycol) Polymers at the Silica/Water Interface: A Microcalorimetric Study. *Langmuir* **9**, 519–522 (1993).

[58] Barbier, D., Brown, D., Grillet, A.-C. & Neyertz, S. Interface between End-Functionalized PEO Oligomers and a Silica Nanoparticle Studied by Molecular Dynamics Simulations. *Macromolecules* **37**, 4695–4710 (2004).

[59] Cheng, S. *et al.* Unexpected Molecular Weight Effect in Polymer Nanocomposites. *Phys. Rev. Lett.* **116**, 038302 (2016).

[60] Voylov, D. N. *et al.* Unraveling the Molecular Weight Dependence of Interfacial Interactions in Poly(2-vinylpyridine)/Silica Nanocomposites. *ACS Macro Lett.* **6**, 68–72 (2017).

[61] Sengwa, R., Kaur, K. & Chaudhary, R. Dielectric properties of low molecular weight poly(ethylene glycol)s. *Polmer International* **49**, 599–608 (2000).

[62] Fu, Z. & Santore, M. M. Kinetics of Competitive Adsorption of PEO Chains with Different Molecular Weights. *Macromolecules* **31**, 7014–7022 (1998).

[63] Scheutijens, J. M. H. M. & Fleer, G. J. Statistical theory of the adsorption of interacting chain molecules. 1. Partition function, segment density distribution, and adsorption isotherms. *J. Phys. Chem.* **83**, 1619–1635 (1979).

[64] Brown, E. & Jaeger, H. M. Shear thickening in concentrated suspensions: phenomenology, mechanisms and relations to jamming. *Rep. Prog. Phys.* **77**, 046602 (2014).

[65] Morris, J. F. Shear thickening of concentrated suspensions: Recent developments and relation to other phenomena. *Annual Review of Fluid Mechanics* **52**, 121–144 (2020).

[66] Seto, R., Botet, R., Meireles, M., Auernhammer, G. K. & Cabane, B. Compressive consolidation of strongly aggregated particle gels. *J. Rheol.* **57**, 1347–1366 (2013).

[67] Guy, B. M., Hermes, M. & Poon, W. C. K. Towards a unified description of the rheology of hard-particle suspensions. *Phys. Rev. Lett.* **115**, 088304 (2015).

[68] Lin, N. Y. C. *et al.* Hydrodynamic and contact contributions to continuous shear thickening in colloidal suspensions. *Phys. Rev. Lett.* **115**, 228304 (2015).

[69] Singh, A., Mari, R., Denn, M. M. & Morris, J. F. A constitutive model for simple shear of dense frictional suspensions. *J. Rheol.* **62**, 457–468 (2018).

[70] Singh, A., Ness, C., Seto, R., de Pablo, J. J. & Jaeger, H. M. Shear thickening and jamming of dense suspensions: The "roll" of friction. *Phys. Rev. Lett.* **124**, 248005 (2020).

[71] Singh, A., Jackson, G. L., van der Naald, M., de Pablo, J. J. & Jaeger, H. M. Stress-activated constraints in dense suspension rheology. *Phys Rev Fluids* **7**, 054302 (2022).

[72] Mari, R., Seto, R., Morris, J. F. & Denn, M. M. Shear thickening, frictionless and frictional rheologies in non-Brownian suspensions. *J. Rheol.* **58**, 1693–1724 (2014).

[73] Ness, C. & Sun, J. Shear thickening regimes of dense non-Brownian suspensions. *Soft Matter* **12**, 914–924 (2016).

[74] Han, E., James, N. M. & Jaeger, H. M. Stress controlled rheology of dense suspensions using transient flows. *Phys. Rev. Lett.* **123**, 248002 (2019).

[75] Maxwell, J. C. On the calculation of the equilibrium and stiffness of frames. *Philos. Mag.* **27**, 294–299 (1864).

[76] Phillips, J. & Thorpe, M. Constraint theory, vector percolation and glass formation. *Solid State Communications* **53**, 699–702 (1985).

[77] He, H. & Thorpe, M. F. Elastic properties of glasses. *Phys. Rev. Lett.* **54**, 2107–2110 (1985).

[78] Liu, K., Kollmer, J. E., Daniels, K. E., Schwarz, J. & Henkes, S. Spongelike rigid structures in frictional granular packings. *Physical Review Letters* **126**, 088002 (2021).

[79] Henkes, S., Quint, D. A., Fily, Y. & Schwarz, J. M. Rigid cluster decomposition reveals criticality in frictional jamming. *Physical Review Letters* **116**, 028301 (2016).

[80] Phillips, J. Topology of covalent non-crystalline solids i: Short-range order in chalcogenide alloys. *Journal of Non-Crystalline Solids* **34**, 153–181 (1979).

[81] Noll, N., Mani, M., Heemskerk, I., Streichan, S. J. & Shraiman, B. I. Active tension network model suggests an exotic mechanical state realized in epithelial tissues. *Nature Physics* **13**, 1221–1226 (2017).

[82] Atia, L. *et al.* Geometric constraints during epithelial jamming. *Nature Physics* **14**, 613–620 (2018).

[83] Yan, L. & Bi, D. Multicellular rosettes drive fluid-solid transition in epithelial tissues. *Phys. Rev. X* **9**, 153–181 (2019).

[84] Smedskjaer, M. M., Mauro, J. C., & Yue, Y. Prediction of glass hardness using temperature-dependent constraint theory. *Phys. Rev. Lett.* **105**, 115503 (2010).

[85] Hespenheide, B. M., Jacobs, D. J. & Thorpe, M. F. Structural rigidity in the capsid assembly of cowpea chlorotic mottle virus. *Journal of Physics: Condensed Matter* **16**, S5055–S5064 (2004).

[86] Heroy, S., Taylor, D., Shi, F. B., Forest, M. G. & Mucha, P. J. Rigid graph compression: Motif-based rigidity analysis fore disordered fiber networks. *Multiscale Modeling Simul.* **16**, 1283–1304 (2018).

[87] Berthier, E. *et al.* Rigidity percolation control of the brittle-ductile transition in disordered networks. *Phys. Rev. Materials* **3**, 075602 (2019).

[88] Zhang, S. *et al.* Correlated rigidity percolation and colloidal gels. *Physical review letters* **123**, 058001 (2019).

[89] Majmudar, T. S. & Behringer, R. P. Contact force measurements and stress-induced anisotropy in granular materials. *Nature* **435**, 1079–1082 (2005).

[90] Corwin, E. I., Jaeger, H. M. & Nagel, S. R. Structural signature of jamming in granular media. *Nature* **435**, 1075–1078 (2005).

[91] Vinutha, H. & Sastry, S. Disentangling the role of structure and friction in shear jamming. *Nature Physics* **12**, 578–583 (2016).

[92] Vinutha, H. & Sastry, S. Force networks and jamming in shear-deformed sphere packings. *Physical Review E* **99**, 012123 (2019).

[93] Lester, D. & Li, R. The frictional pebble game: An algorithm for rigidity percolation in saturated frictional assemblies. *Journal of Computational Physics* **369**, 225–236 (2018).

[94] Jacobs, D. J. & Hendrickson, B. An algorithm for two-dimensional rigidity percolation: the pebble game. *Journal of Computational Physics* **137**, 346–365 (1997).

[95] Seto, R., Mari, R., Morris, J. F. & Denn, M. M. Discontinuous shear thickening of frictional hard-sphere suspensions. *Phys. Rev. Lett.* **111**, 218301 (2013).

[96] Jacobs, D. J., Rader, A. J., Kuhn, L. A. & Thorpe, M. F. Protein flexibility predictions using graph theory. *Proteins: Structure, Function, and Bioinformatics* **44**, 150–165 (2001).

[97] Gameiro, M., Singh, A., Kondic, L., Mischaikow, K. & Morris, J. F. Interaction network analysis in shear thickening suspensions. *Phys. Rev. Fluids* **5**, 034307 (2020).

[98] Nabizadeh, M., Singh, A. & Jamali, S. Structure and dynamics of force clusters and networks in shear thickening suspensions. *Physical Review Letters* **129**, 068001 (2022).

[99] Mari, R. & Seto, R. Force transmission and the order parameter of shear thickening. *Soft Matter* **15**, 6650–6659 (2019).

[100] Singh, A., Pednekar, S., Chun, J., Denn, M. M. & Morris, J. F. From yielding to shear jamming in a cohesive frictional suspension. *Phys. Rev. Lett.* **122**, 098004 (2019).

[101] Rathee, V., Miller, J. M., Blair, D. L. & Urbach, J. S. Structure of propagating high stress fronts in a shear thickening suspension. *Proceedings of the National Academy of Sciences* **119**, e2203795119 (2022).

[102] Thomas, J. E. *et al.* Microscopic origin of frictional rheology in dense suspensions: correlations in force space. *Phys. Rev. Lett.* **121**, 128002 (2018).

[103] E. Thomas, J. *et al.* Investigating the nature of discontinuous shear thickening: Beyond a mean-field description. *Journal of Rheology* **64**, 329–341 (2020).

[104] Edens, L. E. *et al.* Shear stress dependence of force networks in 3d dense suspensions. *Soft Matter* **17**, 7476–7486 (2021).

[105] Goyal, A., Martys, N. S. & Del Gado, E. Flow induced rigidity percolation in shear thickening suspensions. *arXiv:2210.0033 [cond-mat.soft]* (2022).

[106] Morris, J. F. Lubricated-to-frictional shear thickening scenario in dense suspensions. *Physical Review Fluids* **3**, 110508 (2018).

[107] Mari, R., Seto, R., Morris, J. F. & Denn, M. M. Nonmonotonic flow curves of shear thickening suspensions. *Phys. Rev. E* **91**, 052302 (2015).

[108] Melrose, J. R. & Ball, R. C. The pathological behaviour of sheared hard spheres with hydrodynamic interactions. *Europhys. Lett.* **32**, 535–540 (1995).

[109] Kulkarni, S. D. & Morris, J. F. Ordering transition and structural evolution under shear in Brownian suspensions. *J. Rheol.* **53**, 417–439 (2009).

[110] O'Hern, C. S., Silbert, L. E., Liu, A. J. & Nagel, S. R. Jamming at zero temperature and zero applied stress: The epitome of disorder. *Phys. Rev. E* **68**, 011306 (2003).

[111] Denn, M. M. & Morris, J. F. Rheology of non-Brownian suspensions. *Annu. Rev. Chem. Biomol. Eng.* **5** (2014).

[112] Jeffrey, D. J. The calculation of the low Reynolds number resistance functions for two unequal spheres. *Phys. Fluids A* **4**, 16–29 (1992).

[113] Goodrich, C. P., Ellenbroek, W. G. & Liu, A. J. Stability of jammed packings i: the rigidity length scale. *Soft Matter* **9**, 095704 (2013).

[114] Han, E., James, N. M. & Jaeger, H. M. Stress controlled rheology of dense suspensions using transient flows. *Phys. Rev. Lett.* **123**, 248002 (2019).

[115] Hsu, C. P., Ramakrishna, S. N., Zanini, M., Spencer, N. D. & Isa, L. Roughness-dependent tribology effects on discontinuous shear thickening. *Proc. Natl. Acad. Sci. U.S.A* **115**, 5117–5122 (2018).

[116] Zhou, K., Slavin, M., Lutterodt, H., When, M. & Yu, N. A. M. E. L. *Biochemsitry of Foods* (2012).

[117] Singh, J., Colussi, R., McCarthy, O. J. & Kaur, L. *Advances in Potato Chemistry and Technology* (2016).

[118] Mari, R., Seto, R., Morris, J. F. & Denn, M. M. Discontinuous shear thickening in Brownian suspensions by dynamic simulation. *Proc. Natl. Acad. Sci. U.S.A.* **112**, 15326–15330 (2015).

[119] Zobel, H. *Food Polysaccharides and their Applications* (2006).